EFFECTS OF THE DEVELOPMENTAL TERATOGENS ETHANOL AND NICOTINE ON LONG NONCODING RNA EXPRESSION IN MOUSE FETAL NEURAL STEM CELLS OF THE CORTEX

A Thesis

by

ELIZABETH S. RAYMOND

Submitted to the Office of Graduate and Professional Studies of
Texas A&M University
in partial fulfillment of the requirements for the degree of

MASTER OF SCIENCE

Chair of Committee,	Rajesh Miranda
Committee Members,	Farida Sohrabji
	C. Jane Welsh
Interdisciplinary Faculty Chair,	C. Jane Welsh

August 2016

Major Subject: Neuroscience

ABSTRACT

Research on long noncoding RNAs (lncRNAs) has increased significantly over the past few decades. However, investigation of lncRNA continues to lag behind that of other noncoding RNAs species like microRNA (miRNA). One subject receiving limited consideration to date is how teratogens impact the expression patterns and functions of lncRNAs as well as their interactions with other noncoding RNAs. To that end, research was undertaken to determine how six lncRNAs present in the developing nervous system are affected by ethanol and nicotine exposure.

After identifying Malat1, Cyrano, Sox2ot, TUNA, Emx2os, and MIAT as neurodevelopmentally-regulated transcripts, initial experiments probed the expression patterns of each lncRNA in mouse fetal cortical neurosphere cultures treated with ethanol, nicotine, and ethanol and nicotine in combination. While expression of the transcripts of interest was not significantly impacted by ethanol exposure, nicotine treatment reduced expression of TUNA, MIAT, Cyrano, and Malat1. Treatment with both ethanol and nicotine also yielded reduced expression of Cyrano, TUNA, and MIAT. Experimentation progressed to investigations of the potential for interactions between miRNAs, TUNA, MIAT, and Emx2os. These studies focused on whether such associations were mediated by the Argonaute 2 (Ago2) protein, if they were disrupted by ethanol and nicotine treatment, and where these interactions localized within cells. Although bioinformatics tools predicted multiple binding sites between ethanol- and nicotine-sensitive miRNAs and the six lncRNAs of interest, there was no evidence of

Ago2-mediated interactions in either treated or untreated mouse fetal neurosphere cultures. As such, there was also no evidence of disrupted localization of these complexes. However, RNA immunoprecipitation (RIP) experiments with Ago2 did provide insight into the miRNAs actively associated with the RNA-induced silencing complex (RISC) and the compartmentalization patterns of these miRNAs within cells of the developing cortex. Ultimately, this work expands knowledge on the expression patterns of several lncRNAs in the developing brain and serves as the first report detailing the impacts of ethanol and nicotine on lncRNAs in this developmental context.

ACKNOWLEDGEMENTS

I would like to acknowledge several sources of funding associated with this thesis. Though not directly related to this project, some of the monies from NIAAA Grants R01-AA0-13440 and R21-AA0-24055 went toward the purchase of reagents, kits, and other general use supplies in the laboratory that were used in my research. In addition, Grant R01-AA0-13440 directly supported prior experiments in the lab that generated total RNA samples used in this work. With regard to personal funding sources, I was the recipient of the Heep Fellowship in Neuroscience from Fall 2012 through Spring 2014 and I was supported by the Texas A&M Institute for Neuroscience during Summer 2014.

I would like to thank my committee chair and advisor, Dr. Miranda, for his guidance and insight throughout the course of this research. Additional thanks to all of my committee members, Dr. Miranda, Dr. Sohrabji, and Dr. Welsh, for their support throughout my time at Texas A&M University as well as during the time spent writing this thesis and preparing for my defense.

A special thank you to Dr. Sridevi Balaraman, Dr. Rhonda, Holgate, Dr. Pai-Chi Tsai, and Nihal Salem. Each contributed in some way to the success of this research be it through mentorship, training, or direct assistance with experimentation. Your time and expertise was deeply appreciated.

Finally, I would like to extend my love and thanks to my husband, Jeffery Raymond; my parents, Michael and Susan Thom; and my brothers, Scott and Alex

Thom. Your support and encouragement during my graduate school experience—and while writing this thesis—were invaluable.

TABLE OF CONTENTS

Page

Page

LIST OF FIGURES

Page

LIST OF TABLES

Page

CHAPTER I

INTRODUCTION AND LITERATURE REVIEW

I.1 Long Noncoding RNA

For several decades the scientific community puzzled over the fact that over 80% of the human genome produces non-protein coding RNA molecules (Ender and Meister, 2010, Guennewig and Cooper, 2014). These molecules were collectively deemed "junk RNA" and mostly ignored. Despite the fact that ribosomal RNA and transfer RNA were discovered in the 1950s, it took nearly 40 years for researchers to revisit these "junk" transcripts, ultimately concluding that much of the non-protein coding RNA was indeed functional (Palazzo and Lee, 2015, Gomes et al., 2013). Study of the newly termed noncoding RNAs (ncRNAs) provided evidence for the existence of several classes of small ncRNAs including miRNAs, piwi-interacting RNAs (piRNAs), and small nucleolar RNAs (snoRNAs); all distinguished by their relative lengths and molecular functions (Lee et al., 1993, Ender and Meister, 2010, Guennewig and Cooper, 2014). While investigations of these small ncRNAs exploded from the early 1990s through the 2000s, research slowly accumulated on another class of ncRNA initially identified in the mid-1980s and called long noncoding RNA (Lee et al., 1993, Gomes et al., 2013, Palazzo and Lee, 2015). Pioneering studies of lncRNAs characterized H19 (Pachnis et al., 1984, Pachnis et al., 1988, Brannan et al., 1990) and Xist (Brockdorff et al., 1991, Borsani et al., 1991, Brockdorff et al., 1992, Brown et al., 1992), revealing their roles in

genomic imprinting and X chromosome inactivation, respectively. It was not until the past decade and a half that research on lncRNAs truly began in earnest, however. In particular, the discovery of roles for some lncRNAs in cancer development and metastasis has been a major driver in the recent surge of investigation (Gupta et al., 2010, Gutschner and Diederichs, 2012, Tano and Akimitsu, 2012).

As the name suggests, the major characteristic that distinguishes lncRNAs from their smaller noncoding counterparts is their size. In general, any ncRNA sequence longer than 200 base pairs is classified as an lncRNA (Mercer et al., 2009, Geisler and Coller, 2013, Fatica and Bozzoni, 2014). Members of this category can additionally be divided into four groups according to their location within the genome relative to protein coding genes. These groups include sense, antisense, intronic, and intergenic noncoding RNAs (Mercer et al., 2009, Ponting et al., 2009, Ma et al., 2013). Sense lncRNAs are transcribed from genomic regions on the same strand as exons of protein-coding genes and may overlap or entirely encompass these exons (Ponting et al., 2009, Ma et al., 2013). Conversely, antisense lncRNAs are transcribed from genomic regions on the strand opposite coding exons (Mercer et al., 2009, Ma et al., 2013). Intronic lncRNAs are transcribed from regions within the introns of protein-coding genes while intergenic lncRNAs are transcribed from genomic regions between coding genes (Mercer et al., 2009, Ponting et al., 2009, Ma et al., 2013).

While lncRNA sequence length and genomic locations are varied, they do share some things in common with mRNA. For instance, they are transcribed by RNA polymerase II and the majority of lncRNAs are 5' capped, undergo splicing, and exhibit

3’ polyadenylation (Krishnan and Mishra, 2014). However, unlike mRNA, sequence conservation tends to be limited between species, except for a few highly conserved regions (Mercer et al., 2009, Ponting et al., 2009, Diederichs, 2014, Johnsson et al., 2014). While this lack of sequence conservation led many to hypothesize that these sequences had limited functionality compared with the other ncRNA classes, others have more recently suggested that conservation in lncRNAs is most predominant in a transcript’s secondary structure; thus, the specific interactions between lncRNAs and their targets should also be conserved (Diederichs, 2014, Fatica and Bozzoni, 2014, Johnsson et al., 2014, Krishnan and Mishra, 2014). With regard to secondary structure, lncRNAs are a rather diverse noncoding RNA class, which seems to explain the variety of functional roles attributed to them. These include regulation of chromatin structure (Malecova and Morris, 2010, Tsai et al., 2010, Saxena and Carninci, 2011), formation and maintenance of nuclear bodies and molecular scaffolding complexes (Clemson et al., 2009, Wang and Chang, 2011), gene regulation mediated by lncRNA transcription (Kornienko et al., 2013), splicing of target molecules (Hutchinson et al., 2007, Anko and Neugebauer, 2010, Tsuiji et al., 2011), and regulation of protein and transcription factor activity (Wilusz et al., 2009, Geisler and Coller, 2013, Bergmann and Spector, 2014), among others.

Since lncRNAs have not been the focus of intense research for as long as the various small noncoding RNAs, there are many basic research questions that remain to be answered about this category of ncRNA. One such subject requiring additional investigation is how lncRNAs and the other ncRNA classes may interact and what

purpose these interactions serve. Evidence from the primary literature suggests lncRNAs and other noncoding RNAs make up complex regulatory networks (Cesana et al., 2011, Hansen et al., 2013, Wang et al., 2013). Many of these interactions appear to follow the pattern of miRNA-mediated RNA-induced silencing often observed between miRNAs and their targets (Leucci et al., 2013, Wang et al., 2015). More recently, however, some researchers have described lncRNAs that appear to function as miRNA regulators and sequestration molecules (Cesana et al., 2011, Wang et al., 2013, Zhou et al., 2014, Liu et al., 2014). Such transcripts have been termed competing endogenous RNAs (ceRNAs) or miRNA sponges (Cesana and Daley, 2013, Hansen et al., 2013, Tay et al., 2014). For example, two separate studies have identified the lncRNA linc-RNA-RoR as an effective miRNA sponge for miR-145. Wang et al. (2013) observed that by binding miR-145-activated RISC complexes, linc-RNA-RoR served to limit the miRNA-mediated degradation of Oct4, Sox2, and Nanog in human embryonic stem cells; thereby, positively impacting stem cell maintenance. Zhou et al. (2014) further characterized this interaction between miR-145 and linc-RNA-RoR in cancer stem cells. Yet, with only a few hundred of the thousands of known and predicted long noncoding RNA transcripts having undergone much study, there remain a multitude of potential undiscovered lncRNA/small ncRNA interactions to be described.

I.2 Noncoding RNAs and Neural Development: Effects of Teratogens

I.2.1 Alcohol and Development

Alcohol is one of the most commonly abused substances in the world and has been used by humans for thousands of years (Global Status Report On Alcohol And Health 2014, Weiss and Porrino, 2002, Alfonso-Loeches and Guerri, 2011). In 2014, an estimated 139.7 million Americans aged 12 years and older were current alcohol users (Center for Behavioral Health Statistics and Quality, 2014). Worldwide 3.3 million deaths are attributable to the consumption and misuse of alcohol annually (Global Status Report On Alcohol And Health 2014). Aside from fatalities, alcohol use has short-term risks such as alcohol poisoning and bodily injury as well as long-term risks like the development of chronic diseases and alcoholism (Global Status Report On Alcohol And Health 2014, CDC - Fact Sheets-Alcohol Use and Health - Alcohol). However, research has indicated that some of the starkest effects of alcohol use stem from its impacts on the central nervous system. Chronic alcohol use is associated with a variety of structural, cellular, and molecular changes in the (Harper, 1998, Bleich et al., 2003, Yadav et al., 2011, Kryger et al., 2012, Most et al., 2014, Wu et al., 2014, de la Monte and Kril, 2014, Pleil et al., 2015). Such effects result in brain damage and reduced brain mass, which in turn lead to cognitive and motor deficits, dysfunction of the cholinergic system, and dementia (Arendt, 1994, Harper and Matsumoto, 2005, Yadav et al., 2011, de la Monte and Kril, 2014). Although mediated by other factors like nutritional state and genetics,

the severity of alcohol's neurotoxic effects is dose and frequency dependent; heavy drinkers run the greatest risk of developing adverse outcomes (Vengeliene et al., 2008, de la Monte and Kril, 2014).

While the effects of alcohol use during adulthood are severe, exposure during prenatal development is especially damaging. Despite widespread campaigns to curb alcohol consumption during pregnancy, such behavior persists. According to results of the 2013 National Survey on Drug Use and Health, an annual average of 9.4% of pregnant American women aged 15-44 years reported current use of alcohol within one month of taking the survey (Center for Behavioral Health Statistics and Quality, 2014). Drinking during pregnancy can result in negative outcomes including miscarriage, stillbirth, and a suite of disabilities collectively referred to as fetal alcohol spectrum disorders (FASDs) (CDC - Fact Sheets-Alcohol Use and Health – Alcohol, Haycock, 2009, Laufer et al., 2013). FASD-associated disabilities commonly include facial dysmorphologies, microcephaly, growth retardation, poor coordination, hyperactivity and attention issues, poor memory, learning disabilities, cognitive disabilities, vision or hearing issues, and cardiac and skeletal abnormalities (CDC - Fact Sheets-Alcohol Use and Health – Alcohol, Haycock, 2009, Ramsay, 2010, Alfonoso-Loeches and Guerri, 2011).

Echoing results observed in adults, research has determined that the risk of alcohol-related effects and the nature of such effects depend greatly on the timing, frequency, and dose encountered (Alfonso-Loeches and Guerri, 2011, de la Monte and Kril, 2014). Additionally, neurotoxicity caused by developmental alcohol exposure is

associated with structural, cellular, and molecular changes; the same types of changes linked to alcohol-related neurotoxicity in adults (Haycock, 2009, Soares et al., 2012, Carnahan et al., 2013, Tingling et al., 2013, Ungerer et al., 2013, Qi et al., 2014). For example, Camarillo et al. (2008) observed that alcohol exposure disrupted normal cellular migration patterns in the developing cortex, dysregulated the expression of migration-related mRNAs, and reduced neurite branching in differentiating neurons. Similarly, abnormal cellular migration, changes in cytoskeletal structures, and increased apoptotic cell death have been reported in neural crest cells of alcohol-exposed chick embryos (Rovasio and Battiato, 2002). Such mechanisms have ultimately been shown to give rise to agenesis of and abnormalities in various regions of the CNS including the cerebellum, brainstem, corpus callosum, optic nerve, pituitary, neural tube, cortex, hippocampus, olfactory bulb, basal ganglia, and diencephalon (Roebuck et al., 1998, Guerri, 2010, Alfonso-Loeches and Guerri, 2011).

I.2.2 Nicotine and Development

Tobacco products are used widely throughout the world. According to the 2013 NSDUH, 25.5% of the U.S. population aged 12 years and older were current users of tobacco products with 21.3% smoking cigarettes or cigars (Center for Behavioral Health Statistics and Quality, 2015). Smoking tobacco allows for quick and efficient delivery of nicotine directly to the brain (Research Report Series: Tobacco/Nicotine, WHO Report On The Global Tobacco Epidemic, 2008: The MPOWER Package). Each puff of a

cigarette delivers one to two milligrams of nicotine (Research Report Series: Tobacco/Nicotine). With the average smoker taking ten puffs per cigarette, each one provides approximately 10 milligrams of this highly addictive substance (Research Report Series: Tobacco/Nicotine). As with alcohol, smoking—and, therefore, indirectly nicotine—leads to a multitude of adverse health consequences; the most serious being death. It is the leading cause of preventable deaths in the U.S. and results in 6 million fatalities worldwide (WHO Report On The Global Tobacco Epidemic, 2011: Warning About the Dangers of Tobacco, Research Report Series: Tobacco/Nicotine). Other negative outcomes associated with smoking include higher risk of developing cancer, heart disease, chronic obstructive pulmonary diseases, and emphysema as well as higher risk of suffering a stroke or heart attack (Research Report Series: Tobacco/Nicotine). Other impacts on the brain and nervous system are observed at the cellular and molecular levels and have been shown to mediate nicotine addiction and withdrawal (Benowitz, 2009, Lingford-Hughes et al., 2010, Yu et al., 2012, Ng et al., 2013, Bavarva et al., 2013).

In part due to nicotine's highly addictive nature, some women continue smoking during pregnancy despite warnings about the dangers it poses to the unborn child. In 2013, 15.4% of gestating American women aged 15-44 years self-reported as current smokers (Center for Behavioral Health Statistics and Quality, 2014). Of these women, 19.9% smoked during the first trimester, 13.4% continued into the second trimester, and 12.8% smoked through to the third trimester (Center for Behavioral Health Statistics and Quality, 2014). Due to the nature of nicotine metabolism and transfer through the

placenta, concentrations experienced by the fetus can be up to 15% higher than levels observed in the mother (Maccani and Knopik, 2012, Duncan et al., 2015). *In utero* exposure to nicotine and tobacco smoke is associated with growth retardation, dose-dependent low birth weight, disrupted blood flow to and oxygenation of the fetus, and tissue damage to the developing lungs and brain (Slotkin, 1998, Atluri et al., 2001, Mick et al., 2002, Roza et al., 2007, Cents et al., 2012). Smoking during pregnancy also increases the risk of spontaneous abortion, pre-term birth, stillbirth, and Sudden Infant Death Syndrome (SIDS) as well as the likelihood that a child will suffer from respiratory problems, behavioral issues, and nicotine addiction later on (Slotkin, 1998, Atluri et al., 2001, Mick et al., 2002, Takarada et al., 2012, Lee et al., 2014).

Investigation into the impacts of developmental nicotine exposure on the central nervous system has revealed that it exerts its neurotoxic effects through the disruption of structural, cellular, and molecular processes. In general, such disruptions are attributed to nicotine's role as a nicotinic acetylcholine receptor (nAChR) agonist (Benowitz, 2009, Fagerstrom, 2014). Acetylcholine is the endogenous agonist of nAChRs and its regulation in the developing brain is critical for proper cholinergic control of neurogenesis (Slotkin, 1998, Slotkin, 2004, Dwyer et al., 2008). Therefore, *in utero* nicotine exposure causes overstimulation and inappropriately timed stimulation of the cholinergic system resulting in molecular, cellular, and structural abnormalities (Slotkin, 2004, Dwyer et al., 2008). The most common of these effects are impaired synaptogenesis and axonogenesis, reduced cell proliferation, and increased cell death (Slotkin, 1998, Slotkin, 2004, Slikker et al., 2005, Slotkin et al., 2007, Lee et al., 2014,

Aoyama et al., 2016). For example, Roy et al. (1998) observed significant cell death in neural tubes of mouse embryos exposed to one, 10, and 100 μM nicotine. A study by Takarada et al. (2012) revealed that exposure to nicotine inhibited the proliferation of neural progenitors and lead to altered expression of MAP2 and GFAP in neurons differentiated from these neural progenitors. In addition to these outcomes, research also indicates that *in utero* nicotine exposure may impact the expression of nAChRs based on subunit type and alter DNA methylation in offspring (Markunas et al., 2014, Duncan et al., 2015).

I.2.3 Ethanol, Nicotine, and ncRNAs in Neural Development

Recently investigations into the molecular mechanisms of alcohol- and nicotine-related developmental defects have begun to focus on noncoding RNAs. Multiple research teams have reported the existence of miRNAs which are dysregulated following alcohol and/or nicotine exposure (Sathyan et al., 2007, Wang et al., 2008, Huang and Li, 2009, Yadav et al., 2011, Guo et al., 2012, Maccani and Knopik, 2012, Soares et al., 2012, Takahashi et al., 2013, Yokoi and Nakajima, 2013). In a paper by Taki et al. (2014), researchers observed dose-dependent changes in the expression profiles of 40 miRNAs in *C. elegans* individuals exposed to 20 μM or 20 mM nicotine. Another report by Tal et al. (2012) described altered expression of 35 miRNAs in *D. rerio* embryos exposed to ethanol from four to 24 hpf.

Interestingly, although toxicology and teratology are major research foci in developmental biology, few studies on long noncoding RNA have considered the effects of developmental exposure to environmental compounds on these transcripts. Of the publications detailing such effects, several explored the impacts of toxic compounds like dioxin and azacytidine on methylation patterns at the H19 imprint control region and expression of H19 in embryos (Wu et al., 2004, Haycock and Ramsay, 2009, Zhao et al., 2012). One group of researchers reported that expression of Xist was significantly reduced in the cerebrums of female mouse pups following bisphenol-A exposure *in utero* (Kumamoto and Oshio, 2013). However, to date, no studies have considered how ethanol or nicotine might affect lncRNAs in the developing nervous system. In fact, a recent search of the primary literature turned up no papers concerning the role of long noncoding RNAs in the etiology of FASDs. As such, this constitutes a major knowledge gap in the developmental toxicology literature.

I.3 Argonaute Proteins and Noncoding RNA

Argonaute (Ago) proteins are a family of highly conserved RNA binding proteins that can be divided into two subfamilies, Ago proteins and Piwi proteins (Patel et al., 2006, Ender and Meister, 2010, Derrien and Genschik, 2014). Piwi protein expression is mainly restricted to the germ line, while Ago subgroup members are expressed in a variety of tissues (Hammell, 2008, Ender and Meister, 2010). Due to this expression pattern, Ago proteins are of greater interest when studying the brain. In mammals, the

Ago subfamily is comprised of four different proteins: Ago1, Ago2, Ago3, and Ago4 (Hutvagner and Simard, 2008, Ender and Meister, 2010). In general, these proteins have a molecular weight of approximately 100 kDa and contain a Piwi-Argonaute-Zwille (PAZ) domain that allows for binding of small RNAs (Patel et al., 2006, Gagnon and Corey, 2012, Gurtan and Sharp, 2013).

Functionally, Ago proteins are key components of the RISC, which facilitates the regulation of RNA, DNA, and protein targets of small noncoding RNAs in cells (Hutvagner and Simard, 2008, Gagnon and Corey, 2012, Ohrt et al., 2012). This is accomplished when a small ncRNA molecule binds to an Ago protein and proceeds to direct the associated RISC to targets with sequences complementary to itself (Hammell, 2008, Gurtan and Sharp, 2013, Meister, 2013). For miRNAs, variable complementarity between an eight base pair seed region and sequences in a target dictates RISC binding as well as the mechanism of RNA induced silencing (Ender and Meister, 2010, Ohrt et al., 2012). Some common mechanisms include cleavage of the target, altered stability of the target, and altered translation of the target. While any of the four types of Ago proteins can be recruited to RISC for interaction with small ncRNAs, only Ago2 is capable of carrying out direct cleavage of small ncRNA target molecules on its own (Morita et al., 2007, Hutvagner and Simard, 2008, Ender and Meister, 2010). This independent splicing functionality and evidence that it is required for successful early embryonic development have made Ago2 popular for study, especially in developmental contexts (Morita et al., 2007, Lykke-Andersen et al., 2008).

Initial research indicated that Ago proteins and RISC complexes were localized in the cytoplasm (Ohrt et al., 2012, Gomes et al., 2013). This was in large part due to the discovery of cytoplasmic sub-compartments, such as cytoplasmic processing bodies and stress granules, where miRNA-bound Ago proteins and miRNA target molecules aggregate (Hammell, 2008, Hutvagner and Simard, 2008). However, evidence from a growing number of studies has described the localization of Ago proteins/RISC complexes and associated RNA to the nucleus in a variety of organisms (Morita et al., 2007, Hammell, 2008, Gagnon and Corey, 2012, Meister, 2013). Indeed, it appears that active RISC complexes are shuttled between the cytoplasm and nucleus following RISC complex loading in the cytoplasm (Ohrt et al., 2012, Gomes et al., 2013).

As was briefly mentioned above, evidence indicates that lncRNAs and miRNAs interact and regulate one another's transcription, cellular functions, etc. (Cesana et al., 2011, Hansen et al., 2013, Wang et al., 2013). As such, it is likely that Ago proteins are involved in such interactions. Indeed, evidence of lncRNAs interacting with Ago/miRNA complexes has been reported (Ulitsky et al., 2011, Jalali et al., 2013, Juan et al., 2013). Most of these studies have found such interactions via *in silico* analysis of sequencing datasets generated from Argonaute pull downs. However, only one such publication has assessed Ago-mediated miRNA interactions in the developing brain. While Chi et al. (2009) did probe such associations in the post-natal mouse cortex, the investigators did not consider interactions between miRNAs and other ncRNAs, only between miRNAs and mRNA targets found in Ago pull downs. Therefore, there is little to no information available regarding potential miRNA/lncRNA interactions in the brain.

Furthermore, at this time there appears to be nothing in the primary literature that investigates how environmental contaminants or drugs of abuse may change the Ago/ncRNA interactions observed in cells.

I.4 lncRNAs of Interest and Specific Aims

I.1.2 lncRNAs of Interest

Toward the aim of expanding the body of research on lncRNAs, seven transcripts will be considered in this thesis including Malat1, Cyrano, Sox2ot, Megamind, Emx2os, MIAT, and GM7854. The first six of these seven lncRNAs were selected by searching the lncRNA Database (Amaral et al., 2011) for sequences with evidence supporting expression in the nervous system, developmental regulation, conservation from at least mouse to human, and association with the adoption of neural cell fate or maintenance of stem cell character. The final lncRNA of interest, GM7854, was selected because a colleague's work indicated potential regulation of this transcript via miRNA dysregulation. Further, a primary literature search confirmed that none of these lncRNAs have been assessed for effects of ethanol and/or nicotine exposure in a neurodevelopmental context.

A brief summary of what is currently known about each transcript with a focus on why it was selected for this thesis is presented below. Additional information can be found in Table 1.

Table 1. Long Noncoding RNAs of Interest

lncRNA Name	Additional Names	NCBI Accession Number(s)	NCBI PubMed Publication Number	Reasons for Consideration	Selected Publications
Malat1	Neat2	NR_002847.2	166	Highly expressed in the brain especially NSCs and early differentiated neurons and glia; regulated in various cancers; roles in cell migration, mitosis, and cell death	Mercer et al., 2010; Tano et al., 2010; Tripathi et al., 2010
Cyrano	linc-oip5 linc-1510 linc-NUSAP1-1 OIP5-AS1	NR_027832.1 NR_015473.1	1	Expressed in the brain and eye of *D. rerio* embryos; brain and eye defects with knockdown; knockdown inhibited neural differentiation and neural cell fate maintenance	Ulitsky et al., 2011
Sox2ot	Sox2dot	NR_015580.2 NR_015580.1	12	Expressed in embryonic stem cells and cultured neurospheres; suggested role in ocular defects; possible interaction with Sox2	Mercer et al., 2008; Amaral et al., 2009
TUNA	TUNA BX093813 linc-birc6 linc-hhipll	NR_045047.1	2	Expressed in the brain and eye of *D. rerio* embryos; brain and eye defects with knockdown; knockdown inhibited mESC pluripotency and neural differentiation	Ulitsky et al., 2011; Lin et al., 2014
Emx2os	N/A	NR_002863.2	2	Expressed in cells of the developing periventricular proliferative layers and cortical plate of the telencephalon; knockdown downregulated Emx2	Noonan et al., 2003; Spigoni et al., 2010
MIAT	gomafu RNCR2	NR_033657.1 NR_003718.2	14	Expressed in the developing retina and in differentiating NSCs; possible Oct4 target; may regulate splicing factor 1 splicing efficiency	Dinger et al., 2008; Mercer et al., 2010; Rapicavoli et al., 2010; Sheik Mohamed et al., 2010
GM7854	N/A	NR_028417.1	0	Expression induced in fetal NSCs overexpressing miR-153	N/A

I.1.2.1 Malat1

Metastasis associated lung adenocarcinoma transcript 1 (Malat1) is a 6983 base pair (bp) lncRNA located on chromosome 19 in mice (Amaral et al., 2011, Kersey et al., 2012). It consists of a single exon and contains a 61 bp region near the 3' end that is conserved from zebrafish (*Danio rerio*) to therian mammals (Amaral et al., 2011, Kersey et al., 2012, Zhang et al., 2013). Malat1 was first described by Ji et al. (2003) in cells of primary lung tumors from patients with early stage non-small cell lung cancer. Since its discovery Malat1 has been the focus of intense study, the majority of which has focused on its expression in a variety of cancers (Lin et al., 2007, Guffanti et al., 2009, Lai et al., 2012, Han et al., 2013, Ozgur et al., 2013, Ren et al., 2013, Fan et al., 2014, Kuo et al., 2013, Mohamadkhani, 2014, Wang et al., 2014). Malat1 is also highly expressed in cells of the adult and developing nervous system. Researchers have reported the presence of the lncRNA in adult mouse cortex and hippocampus, adult human cerebellum and hippocampus, neural stem cells, and early differentiated neurons and glia (Mercer et al., 2010, Tano et al., 2010, Tripathi et al., 2010, Kryger et al., 2012, Nakagawa et al., 2012, Zhang et al., 2012). In both cancerous and neural cell types, Malat1 is most commonly found localized to the nucleus where it is enriched in nuclear speckle structures (Clemson et al., 2009, Bernard et al., 2010, Mercer et al., 2010, Nakagawa et al., 2012). Functionally, it has been determined that upregulation of Malat1 in cancerous tissue is associated with cancer promotion, increased metastatic nature of tumors, and lower survival rates among patients (Ji et al., 2003, Yamada et al., 2006, Schmidt et al., 2011,

Lai et al., 2012, Gutschner et al., 2013, Liu et al., 2013, Fan et al., 2014). Similarly, Malat1 is believed to play a role in cell migration, mitosis, and cell death in other tissues (Mercer et al., 2010, Tano et al., 2010, Tripathi et al., 2010, Amaral et al., 2011). Several researchers have also determined that this transcript modulates splicing factor levels and distribution; thereby, controlling alternative splicing (Tripathi et al., 2010, Wang et al., 2014).

I.1.2.3 Cyrano, TUNA, and GM7854

Unlike Malat1, the majority of lncRNAs have been the subject of limited study. Of the lncRNAs considered in the scope of this thesis, the least is known about GM7854. Indeed, ENSEMBL and the lncRNA Database either do not contain a record of it at all or simply indicate that it is a predicted lncRNA (Amaral et al., 2011, Kersey et al., 2012). At this time, no publications have investigated this transcript. However, in personal communication with Dr. Pai Chi Tsai it was revealed that during the course of his research GM7854 expression was induced in neural stem cells (NSCs) overexpressing miR-153.

Although more is understood about Cyrano than GM7854, this transcript has still received limited attention. Located on chromosome 2 in *M. musculus*, this lncRNA consists of three exons and has two transcript variants (RefSeq Accession NR_027832.1) (Amaral et al., 2011, Kersey et al., 2012). Within each sequence there is a 67 bp region that is conserved between zebrafish, mice, and humans and may contain a binding site

for miR-7 (RefSeq Accession NR_027832.1) (Ulitsky et al., 2011). At this time, only a single paper has investigated Cyrano expression and functions. This research was performed in zebrafish embryos and found evidence for the transcript's expression in the developing brain and notochord (Amaral et al., 2011, Ulitsky et al., 2011) Knockdown of the transcript led to a variety of nervous system abnormalities including fetuses with small heads and eyes, short curly tails, defects in neural tube opening, loss of Neuro-D positive neurons in the retina and tectum, and enlarged nasal placodes (Ulitsky et al., 2011). When zebrafish, mouse, and human Cyrano transcripts were reintroduced into knockdown embryos, the abnormal phenotypes were rescued (Ulitsky et al., 2011). Cyrano is sometimes referred to as linc-oip5 or OIP-AS1 because it is antisense to the coding region for the OIP5 gene (Amaral et al., 2011). This is potentially significant since OIP5 is associated with chromatin organization and cell cycle control (Naetar et al., 2007).

The lncRNA referred to as TUNA (Tcl1 upstream nuclear associated transcript), or Megamind, is approximately 3303 bps in length and composed of three exons (RefSeq Accession NR_045047.1) (Amaral et al., 2011, Kersey et al., 2012). Although there are multiple orthologs in humans and zebrafish, only one transcript exists in mice. The TUNA gene is located on chromosome 12 in mice with the major region of sequence conservation between humans, zebrafish, and mice consisting of a stretch of 93 bp (RefSeq Accession NR_045047.1) (Amaral et al., 2011, Kersey et al., 2012). Research in *D. rerio* shows that, like Cyrano, this lncRNA is expressed in the developing brain and eye. Some evidence also exists suggesting that orthologs are found in the

brains of humans and mice (Amaral et al., 2011, Ulitsky et al., 2011). Functionally, TUNA is required for normal development of the brain and eye in zebrafish. Following knockout in zebrafish embryos, resultant fetuses had smaller heads and eyes, enlarged brain ventricles, and loss of Neuro-D positive cells in the retina and tectum (Ulitsky et al., 2011). More recently, Lin et al. (2014) reported the expression of TUNA in mouse embryonic stem cells. The researchers suggest a role for TUNA in the maintenance of pluripotency and control of neural cell fate commitment in these cells. Evidence is also provided for localization of TUNA to both the nucleus and cytoplasm, regulation of the transcript in the brains of Huntington's patients, and a possible regulatory connection between TUNA and Sox2 (Lin et al., 2014).

I.1.2.4 Sox2ot

Sox2ot, or Sox2 overlapping transcript, is an lncRNA located on mouse chromosome 3 and partially overlapping the region from which Sox2 is transcribed (Amaral et al., 2011, Kersey et al., 2012). It has seven highly conserved regions in its sequence that are associated with promoters. Sox2ot consists of five exons and has multiple isoforms in mice, humans, amphibians, fish, and other organisms (Amaral et al., 2011). In total, there are sixteen Sox2ot isoforms in *M. musculus*, some of which contain a sequence corresponding to mir-1897 (Kersey et al., 2012). Total length of the Sox2ot sequence considered in these experiments is roughly 2971 bp (RefSeq Accession NR_015580.1) (Amaral et al., 2011).

This lncRNA is expressed in a variety of tissues and cell types including mouse embryonic stem cells, cultured neurospheres, the developing and adult CNS, developing zebrafish and chicken neural tissues, and in the human CNS (Mercer et al., 2008, Amaral et al., 2009, Mandalos et al., 2012, Boraska et al., 2014, Hou et al., 2014). At this time the function of Sox2ot is not fully understood. However, most research on this ncRNA species points toward a role in ocular development and defects. In particular, it appears to be associated with myopia (Amaral et al., 2009). It is also believed that Sox2ot interacts with Sox2. In part this is predicted because of the overlapping nature of the coding regions for each transcript. However, there is some experimental evidence of such an interaction as well (Amaral et al., 2009, Amaral et al., 2011). This is potentially meaningful since Sox2 is critical for early embryogenesis and stem cell pluripotency, especially in the CNS (Amaral et al., 2009). At this time, little is known about the localization of Sox2ot as the author was unable to find publications that explored this. Like the four transcripts of interest already described, the effects of nicotine and ethanol on Sox2ot expression has also not been investigated in any cell or tissue type.

I.1.2.5 Emx2os

Similar to Sox2ot, the coding region for Emx2 opposite strand transcript (Emx2os) is situated nearby that of Emx2 on chromosome 19 in mice (Amaral et al., 2011, Kersey et al., 2012). As the name suggests, these coding regions are on the strand of DNA opposite that of Emx2. The 5023 bp transcript is made up of four exons (RefSeq

Accession NR_002863.2) (Amaral et al., 2011). Unlike the other lncRNAs with multiple exons that are considered in this experiment, only one transcript variant is known (RefSeq Accession NR_002863.2) (Kersey et al., 2012). Also, unlike the other lncRNAs, orthologs of Emx2os in mice and humans maintain conservation of function and genomic location but do not maintain any sequence conservation (Amaral et al., 2011). There is evidence for Emx2os expression in the developing telencephalon (specifically, the periventricular proliferative layers/cortical plate) as well as in periventricular precursor cells in which Emx2 is also expressed (Spigoni et al., 2010). Functionally, knockdown of this ncRNA has been shown to post-transcriptionally down-regulate Emx2 in these cells; ultimately, this suggests a regulatory loop with this transcription factor since a similar effect on Emx2os is observed with Emx2 knockdown (Spigoni et al., 2010). As with Sox2ot and Sox2, it appears that proximity of genomic coding regions yields transcripts that interact closely with one another (Noonan et al., 2003). This proposed relationship is important because the homeobox transcription factor Emx2 is critical for neural development and is believed to contribute to the patterning of the neocortex (Boncinelli et al., 1995, Bishop et al., 2000).

I.1.2.6 MIAT

MIAT, or myocardial infarction associated transcript, is conserved in mice, humans, chickens, and amphibians. In mice the transcript is roughly 8760 bp long and consists of seven exons (RefSeq Accession NR_033657.1; RefSeq Accession

NR_003718.2) (Amaral et al., 2011, Kersey et al., 2012). The coding region for this transcript is located on chromosome 5 in mice (RefSeq Accession NR_033657.1; RefSeq Accession NR_003718.2) (Amaral et al., 2011). Like Emx2os, there only appears to be evidence for a single transcript variant despite MIAT having such a long sequence and multiple exons (Kersey et al., 2012). MIAT was first described by Ishii et al. (2006) when they discovered that dysregulation of this transcript correlated strongly with risk of myocardial infarction. However, it is mostly expressed in the nervous system with strong evidence for its regulation during retinal development, neural stem cell differentiation leading to oligodendrocyte development, and during mouse embryonic stem cell differentiation (Blackshaw et al., 2004, Sone et al., 2007, Rapicavoli et al., 2010, Aprea et al., 2013, Barry et al., 2013). Within these cells, MIAT has been shown to localize to the nucleus (Blackshaw et al., 2004, Mercer et al., 2010, Tsuiji et al., 2011, Ishizuka et al., 2014). Functionally, two major pathways have been described for MIAT. The first involves its interaction with splicing factor 1 (SF1). SF1 can bind with UACUAAC repeat sequences found in the transcript; thus, allowing MIAT to regulate slicing efficiency by inhibiting spliceosomal complex formation (Aprea et al., 2013, Barry et al., 2013, Ishizuka et al., 2014, Shahryari et al., 2014). The second suggests that MIAT is involved in a feedback loop with Oct4 in mouse embryonic stem cells. Its expression may maintain Oct4 expression and ultimately pluripotency (Sheik Mohamed et al., 2010, Shahryari et al., 2014).

I.1.2 Specific Aims

In this thesis work, attempts were made to answer the following questions: 1) What are the expression levels of the lncRNAs of interest in developing NSCs? 2) How is their expression impacted by treatment with ethanol and/or nicotine? 3) Do these lncRNAs interact with Ago2 and, by proxy, miRNAs? 4) Do these interactions change as a result of exposure to ethanol and/or nicotine? 5) Is the location of lncRNAs and/or lncRNA/Ago2 complexes within the nuclear or cytoplasmic compartments of NSCs affected by treatment with ethanol and/or nicotine?

CHAPTER II

MATERIALS AND METHODS

II.1 General Methods

II.1.1 Mouse Fetal Cortical Neural Stem Cell Line

Non-adherent neurosphere cultures derived from neural stem cells/neural precursor cells (NSCs/NPCs) of the dorsal telencephalic vesicle epithelium of gestational day (GD) 12.5 CB57BL/6 mouse fetuses were employed as the model system. All cultures were maintained in serum-free Type II C medium consisting of the following: DMEM/F12 (1:1; Invitrogen/Life Technologies, Carlsbad, CA), EGF (20 ng/ml; PeproTech, Rocky Hill, NJ), bFGF (20 ng/ml; Corning Life Sciences, Tewksbury, MA), ITS-X (1X; Invitrogen/Life Technologies), heparin (5 μg/ml; Sigma-Aldrich, St. Louis, MO), LIF (0.15 ng/ml; Alomone, Jerusalem, Israel), progesterone (0.02 μM; Sigma-Aldrich), and pen-strep (1%; Invitrogen/Life Technologies). This model system was previously published (Santillano et al., 2005, Miranda et al., 2008) and closely approximates the conditions encountered by NSCs/NPCs *in vivo* at this stage of development. All neurosphere cultures used in this work were generated from a cryo-preserved cerebral cortical NSC/NPC line previously established in the laboratory.

II.1.2 Neurosphere Culture Generation and Treatment

NSCs were cultured as suspended neurospheres in T-75 plastic tissue culture flasks (Corning Life Sciences) in 15-20 ml serum-free Type II C medium following previously published procedures (Santillano et al., 2005, Miranda et al., 2008). Cultures were passaged no more than 12 times prior to use and were allowed to reach 80-90% confluency within a flask before they were passaged or used in an experiment. Treatments followed a five day static renewal model wherein 15-20 ml fresh Type II C medium doped with the appropriate concentration of the experimental compound of interest was added to each flask on the first and third days of the treatment period. Incubation occurred at 37˚C and 5% CO_2.

II.1.3 Primer Design and Selection

Primers were designed for each lncRNA by obtaining their cDNA sequences from NCBI Nucleotide (Benson et al., 2013) and using NCBI PrimerBLAST (Ye et al., 2012) to generate primer pairs conforming to the following parameters: high target specificity; melting temperatures between 67 and 71˚C, but within 3˚C of one another for each primer pair; GC content between 40 and 65%; minimal homo- and hetero-dimer formation; minimal hairpin formation; amplicon length between 150 and 350 base pairs and primer lengths less than 26 base pairs. Primers were also designed to include the most highly conserved regions of the lncRNA sequences of interest in the resulting

amplicon. These regions were determined by alignment of mouse, human and zebrafish cDNA sequences from NCBI Nucleotide via NCBI BLAST (McGinnis and Madden, 2004). Finally, PrimerBLAST was set to eliminate any primer pairs showing specificity to mouse RefSeq sequences other than the sequence of interest.

Table 2. Primer Pairs

Target	Forward Primer	Reverse Primer
Malat1	GGTGGGAATGTAGGAAGTCGGATGAA	AGTGCCAGCCACCAGCGTCTTT
Cyrano	TGTGCCTCCTCCCTTCTCCATGTAA	TTTCTCCTATCCGCAGGGAGACTATCA
Sox2ot	TCGACAACTCTGCCCTCTCCCTGA	TCAGCAAATGCTGTCGTCTCTGGCTA
TUNA	GCAACCAAGATGGTAATCACGAGTGG	ACCCTTGTCTCGTGGCCATCCT
Emx2os	TTGAAGCCGTTTCCATCCACCAGT	CTAGGCAGATGAAGGCAATAGCATGT
MIAT	GGAGCTCCAAGACCCACAGCCTAGAA	TAGGACATGCTCGGGCCAGGTTAGT
GM7854	CCTGCCCTTGTGGGGTTGGAGGT	AGTCACCTCTTTGGGCTGCCAGCTA
GAPDH	AGTATGTCGTGGAGTCTACTG	TGGCAGCACCAGTGGATGCAG
HPRT1	AAGACTTGCTCGAGATGTCATGAA	ATCCAGCAGGTCAGCAAAGAA
PPIA	CGCGTCTCCTTCGAGCTGTTTG	TGTAAAGTCACCACCCTGGCACAT

Once primers had been tailored in PrimerBLAST, the candidate primer pairs were also evaluated via Primer3 (Untergasser et al., 2012), IDT Oligo Analyzer (Integrated DNA Technologies, Coralville, IA) and OligoPerfect Designer (Life Technologies). Primer pairs most closely corresponding to the above criteria were

ordered for qPCR. Primers for normalization standards were GAPDH (Kedmi and Orr-Urtreger, 2007), HPRT1 (Caldwell et al., 2008) and PPIA (Mamo et al., 2007, Carnahan et al., 2013). A full list of primers generated for the lncRNAs of interest as well as those used as normalization standards can be found in Table 2.

II.1.4 RNA Extraction and Quantification

After the completion of the 5 day treatment period, the contents of each flask were pelleted and the medium removed. Following two washes with 1X DPBS (Life Technologies), a mirVana miRNA Isolation Kit (Life Technologies) was used to lyse cells and extract total RNA according to the manufacturer's instructions. Briefly, the provided lysis buffer was added to pellets and the solutions vortexed to further disrupt cell membranes. For organic extraction, a provided miRNA homogenate additive was added followed by vortexing and incubation. Then, acid-phenol:chloroform was added in a volume equal to that of the sample. The resultant solution was vortexed and centrifuged to separate the aqueous and organic phases. The aqueous phase was transferred to a new tube and eluted in nuclease free H_2O via spin column following two washes with provided wash buffers. Total RNA extracts were then assessed for RNA content and purity using the $A_{260/280}$ functionality of a Nanodrop 2000 spectrophotometer (Thermo Scientific, Waltham, MA).

II.1.5 cDNA Synthesis

qScript cDNA Synthesis kits (Quanta Biosciences, Gaithersburg, MD) were used to synthesize cDNA for all qPCR reactions according the manufacturer's instructions. Starting total RNA template concentrations for each cDNA synthesis reaction was 250 ng/µl. The appropriate volume needed to reach this RNA concentration for each sample was combined with 4 µl qScript reaction mix, 1 µl qScript reverse transcriptase and enough nuclease free H_2O to bring the total solution volume to 20 µl. Cycling was performed in a thermal cycler with parameters as follows: 25˚C for 5 min., 42˚C for 30 min., 85˚C for 5 min. and a hold at 4˚C. The cDNA underwent a 1:16 dilution with nuclease free water prior to use in qPCR reactions. Both diluted and undiluted cDNA was stored at -20˚C.

II.1.6 qPCR

All qPCR reactions were run using PerfeCTa SYBR Green Fastmix kits with ROX (Quanta Biosciences). Reaction volumes were 10 µl (5 µl SYBR Green reaction mix, 2 µl nuclease free water, 0.5 µl forward primer, 0.5 µl reverse primer and 2 µl cDNA template) and each sample was run in triplicate on a 384-well microplate. Primer solutions used for qPCR reactions were working solutions consisting of 1:10 dilutions of stock solutions prepared from lyophilized oligo nucleotides (100 µM; IDT and Life Technologies). All qPCR was performed on an ABI 7900 HT Real-Time PCR System

(Life Technologies) set for 'Standard Curve (ΔA)' analysis. Cycling parameters were as follows: 50˚C for 2 minutes; 95˚C for 10 minutes; 40 cycles of 95˚C for 15 s, 57˚C for 30 s, 65˚C for 30 s; a melting/dissociation curve step.

II.1.7 New Primer Validation

To ensure amplification of the intended targets, the products of qPCR reactions with whole cell, untreated control templates for each lncRNA primer pair were analyzed via Southern Blot and DNA sequencing. For Southern Blotting, 7 µl inputs (6 µl qPCR reaction product, 1 µl Laemmeli buffer) were run on 1.5% agarose gels (1.5 g agarose (Bio-Rad, Hercules, CA) in 100 mL 1X TBE buffer (Life Technologies)) with ethidium bromide (2 µl of 10mg/mL ethidium bromide per 100 mL agarose gel) and 5 µl DNA ladder (Invitrogen). The gels were run in 1X TBE running buffer at 90 V for 2 hours before visualization under UV light. Bands were excised and purified using a Gel/PCR DNA Fragments Extraction kit (IBI Scientific, Peosta, IA). Sequencing was performed by the Gene Technologies Laboratory of the Texas A&M University Institute of Developmental and Molecular Biology. All purified qPCR reaction products underwent sequencing with 8 pmol of primer (lncRNA specific primers as described above; 4 pmol forward, 4 pmol reverse) and ABI Big Dye Reaction Mix (PerkinElmer) on an ABI PRISM® 3100 Genetic Analyzer (Life Technologies). Product identity was assessed via NCBI BLAST (McGinnis and Madden, 2004).

II.1.8 Data Analysis

All qPCR data was reported as a Ct value corresponding to each well on a 384-well microplate. The three Cts produced for each sample (run in triplicate) were used to generate a single averaged Ct value for a sample in combination with a given primer pair. For the potential normalization standard primer pairs considered, these averaged Ct values were input in to the EST Database of Cotton Reference Gene Expression Tool and assessed via BestKeeper (Pfaffl et al., 2004), NormFinder (Andersen et al., 2004), Genorm (Vandesompele et al., 2002), and the comparative delta-Ct method (Silver et al., 2006). The two 'best' reference genes indicated by Genorm were checked against the results of the other three evaluation methods to ensure that their standard deviations were below 1.0. Provided these requirements were met, the geometric mean of the two 'best' reference genes was calculated for each sample. Effect of treatment was then evaluated for these geometric mean values using an Independent Samples T-Test or ANOVA. Having met these requirements, these geometric mean values were used as the normalization values. If these requirements were not met, the geometric mean per sample of all potential normalization standards was calculated and assessed for an effect of treatment. Again, if the requirements were fulfilled, the geometric mean values of all potential reference genes were used as the normalization standard. Normalization standard values were then subtracted from the averaged Cts for each sample/lncRNA primer pair combination. The resultant normalized Ct values were used to calculate a $2^{-\Delta\Delta Ct}$ value for each sample that ultimately underwent statistical analysis.

SPSS Statistics 22 (IBM, Armonk, NY) was used to conduct all statistical analyses. As appropriate, One-way ANOVA (with post hoc Fisher's LSD tests) and Independent Samples T-tests were performed to determine statistical significance of fold changes in lncRNA expression resulting from treatment. Grubbs Outlier Tests were performed before application of these tests to ensure elimination of outliers in the data.

II.2 lncRNA Expression in Untreated and Ethanol-Treated Neurospheres

Treatment groups for this experiment consisted of twenty untreated control samples and twenty samples treated with 320 mg/dl ethanol. Each sample corresponded to one treated or untreated T-75 culture flasks. All details of cell culture generation and treatment, RNA extraction and quantification, cDNA synthesis and qPCR followed the procedures outlined in the 'General Methods' section above. Data generated were non-normally distributed and positively skewed. A logarithmic transformation was performed prior to statistical analysis via an Independent Samples T-Test. The transcripts used to generate the normalization standard for this experiment were HPRT1 and PPIA.

II.3 lncRNA Expression in Neurospheres Treated with Ethanol, Nicotine and Ethanol & Nicotine in Combination

Treatment groups for this experiment are presented in Table 3. Each treatment group consisted of four samples corresponding to each of four treated or untreated T-75 culture flasks. All details of cell culture generation and treatment, RNA extraction and quantification, cDNA synthesis, qPCR and data analysis followed the procedures outlined in the 'General Methods' section above. Transcripts used to generate normalization standards for this experiment were GAPDH, HPRT1 and PPIA.

II.4 Prediction of lncRNA and miRNA Interactions

II.4.1 miRBase and NCBI Nucleotide

miRBase (Griffiths-Jones, 2004, Griffiths-Jones et al., 2006, Griffiths-Jones et al., 2008, Kozomara and Griffiths-Jones, 2011, Kozomara and Griffiths-Jones, 2014) sequences for ethanol-sensitive miRNAs and miRNAs amplified in the Human miRNA Array Panels were used along with the sequences obtained from NCBI Nucleotide for each lncRNA in order to predict lncRNA/miRNA interactions.

Table 3. Ethanol and Nicotine Treatment Groups and Samples Generated

Treatment Group	Sample Size (T-75 flask)
Untreated	4
320 mg/dl EtOH	4
1 μM Nicotine	4
320 mg/dl EtOH + 1 μM Nicotine	4

II.4.2 RNA Hybrid and in silico Analysis of lncRNA/miRNA Interactions

RNA Hybrid Version 2.1 (Rehmsmeier et al., 2004) was used to detect possible binding sites of ethanol-sensitive and nicotine-sensitive miRNAs (Sathyan et al., 2007, Balaraman et al., 2012) with all six lncRNAs of interest. RNA Hybrid Version 2.2 was used to detect possible binding sites of miRNAs amplified in Human miRNA Array Panels (Exiqon, Woburn, MA) run to determine possible primer pairs for normalization standards in Argonaute RNA immunoprecipitation (RIP) experiments. Binding affinity of these miRNAs with TUNA, Emx2os and MIAT (the three lncRNAs assessed in the nuclear and cytoplasmic RIP samples) was assessed. In both cases, only those predicted binding sites with mfe $\leq$ -21.0 and conforming to general miRNA target binding rules outlined in Grimson et al. (2007), specifically 7mer or 8mer binding with the miRNA seed region, were reported as likely interactions.

II.5 Ago2 RNA Immunoprecipitation (RIP)

II.5.1 Treatment Groups

Treatment groups in this experiment were identical to those for the ethanol & nicotine treatment sample set described in Table 3. An additional set of four untreated control samples (0 mg/dl EtOH + 0 μM Nicotine) that did not undergo nuclear and cytoplasmic fractionation or RNA immunoprecipitation was also included in analysis for this experiment.

II.5.2 Formaldehyde Crosslinking

Each neurosphere culture underwent formaldehyde crosslinking according to a previously published procedure (Moran et al., 2012). In brief, neurosphere cultures were pelleted following completion of treatment. These pellets were re-suspended in 10 ml 1X DPBS (Life Technologies) supplemented with 20% paraformaldehyde solution (Electron Microscopy Sciences, Hatfield, PA) to produce a final concentration of 0.3% paraformaldehyde. The mixture was incubated at room temperature with gentle rotation for 10 minutes. Crosslinking was quenched via the addition of 2M glycine (Sigma-Aldrich) to produce a final concentration of 0.125 M glycine. Incubation lasted 5 minutes at room temperature followed by two washes with 1X DPBS. The pellet then

either immediately underwent nuclear and cytoplasmic fractionation or was stored at -80˚C until fractionation could be performed.

Table 4. Immunoprecipitation and Fractionation Samples Generated

	Fractionation	Immunoprecipitation
Untreated	4 Nuclear Fractions	4 Nuclear Supernatants 4 Nuclear RIPs
	4 Cytoplasmic Fractions	4 Cytoplasmic Supernatants 4 Cytoplasmic RIPs
320 mg/dl EtOH	4 Nuclear Fractions	4 Nuclear Supernatants 4 Nuclear RIPs
	4 Cytoplasmic Fractions	4 Cytoplasmic Supernatants 4 Cytoplasmic RIPs
1 µM Nicotine	4 Nuclear Fractions	4 Nuclear Supernatants 4 Nuclear RIPs
	4 Cytoplasmic Fractions	4 Cytoplasmic Supernatants 4 Cytoplasmic RIPs
320 mg/dl EtOH + 1 µM Nicotine	4 Nuclear Fractions	4 Nuclear Supernatants 4 Nuclear RIPs
	4 Cytoplasmic Fractions	4 Cytoplasmic Supernatants 4 Cytoplasmic RIPs

II.5.3 Nuclear and Cytoplasmic Fractionation

Nuclear and cytoplasmic fractionation was performed on each crosslinked sample using the NE-PER Nuclear and Cytoplasmic Extraction kit (Thermo Scientific) according to the manufacturer's instructions. In brief, cell pellets were resuspended in 100 µl CER I solution and incubated for 10 min. on ice. 5.5 µl CER II solution was added prior to a 1 min. incubation on ice and a 5 min. centrifugation at maximum speed. The resulting supernatants containing the cytoplasmic fractions from each pellet were removed and placed into new centrifuge tubes. The remaining pellets (nuclei-rich) were resuspended in 50 µl NER solution and incubated on ice for 40 min. with vortexing every 10 min. All samples were centrifuged at maximum speed for ten minutes and the supernatants containing the nuclear fraction for each sample removed and placed in new tubes. These fractions then either immediately underwent Ago2 RNA immunoprecipitation or were stored at -80˚C until immunoprecipitation could be performed. Both the CER I and the NER solutions were supplemented with Halt protease and phosphatase inhibitor (Thermo Scientific) at a ratio of 10 µl protease inhibitor to 1 ml solution. All samples were supplemented with 2.5 µl RNaseOUT recombinant ribonuclease inhibitor (Life Technologies) upon addition of CER I solution. The samples generated during this step are detailed in Table 4.

II.5.4 Ago2 RNA Immunoprecipitation (RIP)

Immunoprecipitation with 50 µl Dynabeads Protein G (Invitrogen/Life Technologies) and 5 µl anti-Ago2 antibody (Abcam, Cambridge, MA) was performed on all fractions produced during nuclear and cytoplasmic fractionation. One untreated control sample (nuclear and cytoplasmic fractions) underwent immunoprecipitation with 50 µl Dynabeads Protein G and 5 µl anti-alpha tubulin antibody (Sigma Aldrich) to serve as a control for Western blotting. All RIPs were performed following the Dynabeads Protein G instructions supplemented with steps from Moran et al. (2012). Briefly, each nuclear or cytoplasmic fraction was incubated with antibody at 4˚C for 1 hour and 10 minutes with rotation. Immediately following, the sample/antibody solutions were incubated with 50 µl Dynabeads Protein G at 4˚C with rotation for 1 hour. The Dynabeads were pelleted using a magnetic stand and the supernatants transferred to new tubes. The Dynabeads were then washed two times with 200 µl 0.05% Tween 20 (Sigma Aldrich) in 1X DPBS and once in 200 µl 0.02 % Tween 20 in 1X DPBS. Finally, 100 µl 0.02% Tween 20 in 1X DPBS was added to each supernatant sample and used to resuspended each Dynabeads (RIP) sample. A 15 µl aliquot of each Dynabeads sample was then taken and stored to be used as inputs for Western blotting. The supernatants and the remaining Dynabeads samples (with antibody and associated proteins, etc. attached) then either immediately underwent proteinase K digestion/uncrosslinking or were stored at -80˚C until these steps could be performed.

The 15 µl aliquots of Dynabeads were also stored at -80˚C until Western blotting could be performed. The samples generated during this step are summarized in Table 4.

II.5.5 Western Blotting

Western blotting was performed using the Dynabeads aliquots retained at the end of the RIP step. This was undertaken in order to validate the success of the immunoprecipitation. For each sample, 10 µl of each 15 µl aliquot was combined with 4 µl Laemmeli buffer and incubated in a 95˚C heat block for 5 min. Samples were then loaded with 10 µl Kaleidoscope Prestained Standard protein ladder (Bio-Rad) into two 17-well NuPAGE Novex 4-12% Bis-Tris Protein Gels (Life Technologies), one with all 16 nuclear fraction RIP samples and one with all 16 cytoplasmic RIP samples. An XCell SureFit electrophoresis chamber (Life Technologies) was used to run the gels with MOPS buffer (Teknova, Hollister, CA) for 60 min. at 200 Volts. An iBlot transfer system (Life Technologies) was used to transfer proteins to a PVDF membrane (7 min. transfer period). The anti-Ago2 antibody used for RIP was used as the primary antibody for Western blotting at a ratio of 1:1000. A goat anti-mouse-HRP secondary antibody (Santa Cruz Biotechnology, Dallas, TX) was used at a ratio of 1:2500 in conjunction with a Western Lightning Plus ECL kit (PerkinElmer, Waltham, MA) and a FluorChem Q imaging system (4.19 Megapixels CCD camera, 50 mm, f/0.95 fixed/manual lens; ProteinSimple, Santa Clara, CA) for protein detection and quantification. All images were captured with an aperture setting of 2.8, a setting of 2.5 and an exposure time of 1

min. Each membrane was then stripped with Restore Western Blot Stripping Reagent (Life Technologies) and re-probed with anti-alpha tubulin antibody as a control.

An additional Western blot was run to confirm detection of Ago2. The remaining 5 µl of the Dynabeads for one sample from each treatment group/fraction combination (each with 5 µl Laemmeli buffer) was assessed along with the corresponding tubulin RIP samples. All other aspects of the Western blotting process were identical to those described above. Gel setups for the Western blots are detailed in Figure 1. Image processing was performed using ImageJ (Schneider et al., 2012) and Microsoft PowerPoint. Processing with ImageJ included color inversion, auto-adjustment of brightness/contrast, smoothing and/or sharpening, despeckling and horizontal flipping. The extent of processing performed in PowerPoint was straightening and cropping images.

II.5.6 Proteinase K Digestion and Uncrosslinking

All supernatants and Dynabeads/antibody/protein solutions from the nuclear and cytoplasmic fractions of each sample underwent proteinase K digestion at 42˚C for 30 minutes with occasional vortexing. A total volume of 150 µl Proteinase K buffer (117 µl 0.02% Tween 20 in 1X DPBS, 15 µl 10% SDS in nuclease free H_2O, 18 µl proteinase K (Sigma Aldrich)) was added to each supernatant and RIP sample prior to incubation. Uncrosslinking was then performed on a heat block at 65˚C for four hours with vortexing every hour. Supernatants were removed from each RIP sample and placed in

new tubes. All samples then either immediately underwent RNA extraction or were stored at -80˚C until extraction could be performed.

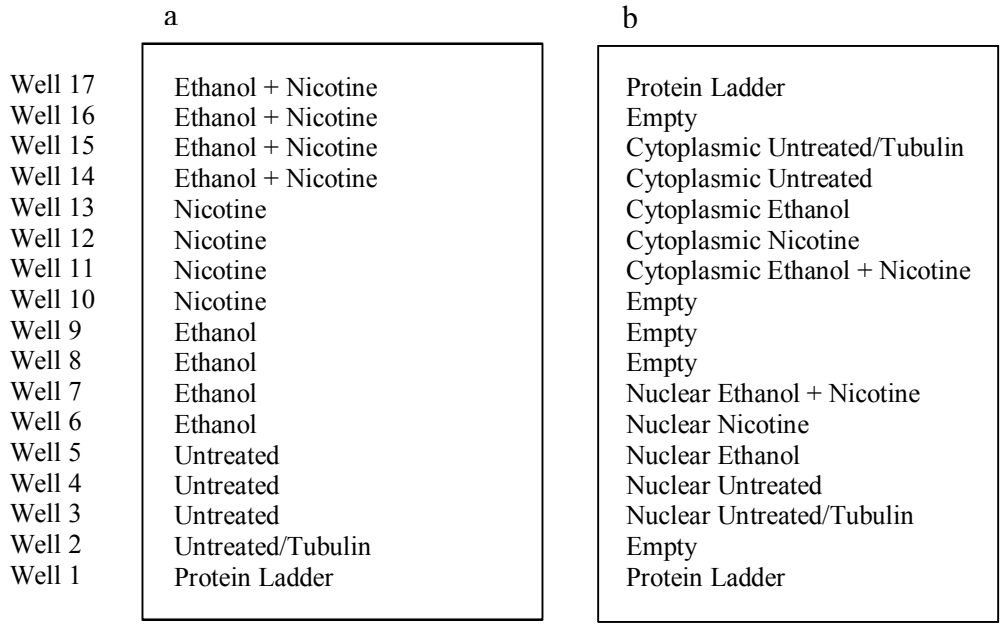

Figure 1. Western Blot Gel Loading Schemes

(a) Original individual nuclear and cytoplasmic RIP blot setup, (b) Follow up blot setup with treatment group representative samples from both nuclear and cytoplasmic RIPs.

II.5.7 RNA Extraction and Quantification

TRIzol® Reagent (Life Technologies) was used to extract total RNA from each nuclear RIP, nuclear supernatant, cytoplasmic RIP and cytoplasmic supernatant sample according to the manufacturer's instructions. Briefly, 500 µl TRIzol® Reagent was added to each supernatant and RIP sample prior to incubation at room temperature for 5 min.

100 µl chloroform was then added to the supernatant and RIP samples and the contents of each tube shaken for 15 seconds. All samples were incubated 2-3 min. and centrifuged for 15 min. at 4˚C to separate the aqueous and organic phases. The aqueous layers containing RNA were then transferred to new tubes. Due to the relatively small sample volumes, 1 µl GlycoBlue carrier (Life Technologies) was added to the aqueous phase prior to RNA precipitation. 250 µl 100% isopropanol was added to each supernatant and RIP aqueous phase. All samples were incubated at room temperature for 10 minutes and then centrifuged for 10 min. at 4˚C. Supernatants were removed and the pelleted RNA washed with 500 µl 75% ethanol for each supernatant and RIP sample. All samples were vortexed and centrifuged for 5 min. at 4˚C followed by air drying of the RNA pellets for 10 min. Finally, each RNA pellet was resuspended in nuclease free H_2O via gentle pipetting and then incubated in a 60˚C heat block for 10 min. Supernatant samples were resuspended in 50 µl nuclease free H_2O and RIP samples were resuspended in 40 µl nuclease free H_2O. All total RNA samples were then either immediately assessed for RNA content or stored at -80˚C until said analysis could be performed. Total RNA content and purity were assessed by $A_{260/280}$ ratio on a Nanodrop 2000 spectrophotometer (Thermo Scientific).

II.5.8 miRNA Array Panels and Ago2 RNA Immunoprecipitation Normalization Standard Selection

Candidate normalization standards were determined for use in qPCR with the nuclear and cytoplasmic RIP samples. To find potential standards, a composite nuclear RIP sample and a composite cytoplasmic RIP sample were generated (~60-70 ng total RNA from each nuclear or cytoplasmic RIP sample) and run on Human miRNA Array Panels (Exiqon) to assess which miRNAs were most highly expressed. Expression levels were determined by normalizing Ct values of amplified products from each fraction to Ct values for each of the products from the Human miRNA Array Panels run with whole cell lysate from untreated fetal cortical neurospheres. Commercially available primers (Exiqon) were then ordered for the most promising candidates. Primer pairs ordered are outlined in Table 5.

II.5.9 cDNA Synthesis, qPCR and Data Analysis

Following cDNA synthesis, each cDNA sample was diluted 1:4 with nuclease free H_2O prior to use in qPCR. In order to detect even low levels of amplified product, 50 cycles were run during qPCR instead of 40-45 as previously outlined. All other details of cDNA synthesis, qPCR and data analysis followed those described in the 'General Methods' section above.

Table 5. Commercial Primer Pairs Assessed as RIP Normalization Standards

Target	Catalog Number	mirBase ID	Fraction
hsa-mir-490-3p	205875	MIMAT0002806	Both
mmu-mir-346	205158	MIMAT0000597	Nuclear
hsa-mir-30a*	204457	MIMAT0000088	Both
mmu-mir-9*	204620	MIMAT0000442	Cytoplasmic
SNORD49A	203904	N/A	Nuclear

CHAPTER III

EXPERIMENTAL RESULTS

III.1 Primer Validation

In order to assess expression levels of Malat1, Cyrano, Sox2ot, TUNA, Emx2os, MIAT, and GM7854 via qPCR, transcript-specific primer pairs were required. After searching the primary literature and commercially available primer sets it was determined that primers would need to be designed and analyzed for specificity. Following qPCR on cDNA from untreated neurosphere cultures, Northern blotting and DNA sequencing were performed on reaction products for each primer pair generated. All but one of these primer sets successfully amplified the target transcript when sequences were assessed for identity matches to the RefSeq database using NCBI BLAST (McGinnis and Madden, 2004).

Primer pairs for Malat1, TUNA, Emx2os, and MIAT all yielded amplification products with the highest sequence cover and identity matches corresponding to the NCBI accession number and sequence used to design them. Sequence cover matches and sequence identity matches for these lncRNAs and primers were as follows: Malat1, cover = 70%, identity = 97%; TUNA, cover = 96%, identity = 99%; Emx2os, cover = 98%, identity = 99%; MIAT, cover = 98%, identity = 85%. While it did not yield an amplicon with a hit to the RefSeq database or the NCBI accession number used to design the primer set, the primer pair for Cyrano did result in a product with high sequence

cover and identity matches to several closely associated transcripts. The *M. musculus* RIKEN cDNA 1700020I14 clone:M5C1004K09 (AK147270.1), *M. musculus* RIKEN cDNA 1700020I14 clone:5031400H20 (AK030275.1), *M. musculus* RIKEN cDNA 1700020I14 clone:4732497J20 (AK029148.1), and *M. musculus* RP23-22A15.2 gene (HG978614.1) all yielded a 92% cover match and a 100% identity match with the product. BLAST comparison of these transcripts with the transcript used to design the Cyrano primer set (NR_027832.1) resulted in the following sequence cover and identity matches: AK147270.1, cover = 97%, identity = 100%; AK030275.1, cover = 96%, identity = 99%; AK029148.1, cover = 96%, identity = 100%; HG978614.1, cover = 98%, identity = 100%. Thus, it was concluded that the target lncRNA was successfully amplified.

Similarly, primers for Sox2ot yielded a product without a BLAST hit to the RefSeq database or the NCBI accession used in their design. However, OTTMUST00000095020.1/Sox2ot gene (HG978904.1) and cDNA RIKEN clone:633044I21 (AK031919.1) both had a sequence cover match of 77% and identity match of 98%. When compared with the Sox2ot sequence used to design the primers, (NR_015580.1) sequence cover was 19% and sequence identity was 100%. Though these results were less convincing than those for Cyrano, the fact that one of the major hits was called “Sox2ot”, and that it is believed *M. musculus* Sox2ot has 16 isoforms, it was concluded that the primer set was specific to the target lncRNA (although presumably to an isoform other than that used to design the primers).

Unlike the rest of the primer sets, the primer pair for GM7854 yielded its highest cover and identity match with a transcript completely unrelated to the target. Results indicated a 95% sequence cover match and an 88% sequence identity match with the predicted *M. musculus* LOC102638050 noncoding RNA (XR_401556.1). In contrast, the sequence cover match with GM7854 (NR_028417.1) was 17% and the identity match was 96%. Therefore, GM7854 was not considered in subsequent experimentation. Percentage sequence cover and identity matches for each target transcript and associated primer pair are outlined in Table 6.

Table 6. Sequence Cover and Identity Matches of Primer Pairs and lncRNAs

Target	Product Coverage Match (%)	Product Identity Match (%)	NCBI Accession Match
Malat1	70	97	NR_002847.2
Cyrano	92	100	AK147270.1 AK030275.1 AK029148.1 HG978614.1
Sox2ot	86	95	AK031919.1 HG978904.1
TUNA	96	99	NR_045047.1
Emx2os	98	99	NR_002863.2
MIAT	98	85	NR_033657.1 NR_003718.2
GM7854	17	96	NR_028417.1

III.2 lncRNA Expression in Untreated and Ethanol-Treated Neurospheres

With validated primer pairs for the majority of the lncRNAs of interest, the next step was to determine their baseline expression levels in NSCs and discover whether or not any of the transcripts exhibited ethanol sensitivity. qPCR successfully amplified the lncRNAs of interest in both control and EtOH-treated samples. Figure 2 shows the expression levels of each transcript in EtOH-treated and untreated neurospheres. Relative expression levels (average $2^{-\Delta\Delta Ct}$) of the six lncRNAs in untreated NSCs were as follows: Malat1, 1.40; Cyrano, 1.46; Sox2ot, 2.01; TUNA, 1.95; Emx2os, 1.73; MIAT, 2.34. Statistical analysis revealed no significant difference in expression levels of the six lncRNAs between untreated controls and EtOH-treated samples (Independent Samples T-Test: Malat1, $p = 0.420$; Cyrano, $p = 0.633$; Sox2ot, $p = 0.594$; TUNA, $p = 0.212$; Emx2os, $p = 0.660$; MIAT, $p = 0.859$). These results indicated that none of the transcripts of interest were ethanol-sensitive.

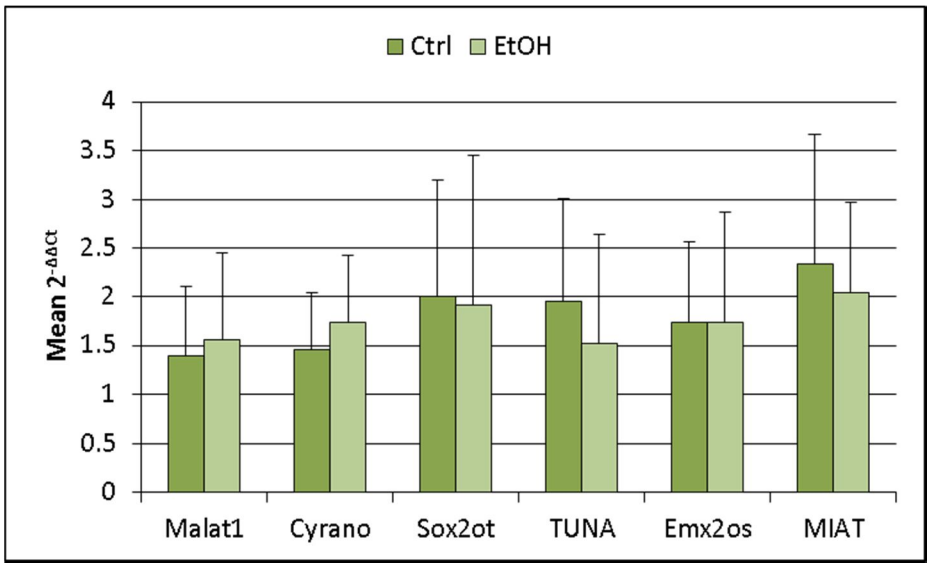

Figure 2. Expression of lncRNAs in EtOH-Treated Neurospheres.

*Mean relative expression levels of the six lncRNAs of interest under two treatment conditions: 0 mg/dl EtOH and 320 mg/dl EtOH. *Statistical significance at α= 0.05.*

III.3 lncRNA Expression in Neurospheres Treated with Ethanol, Nicotine, and Ethanol & Nicotine in Combination

Despite no effect of EtOH exposure on the expression of Malat1, Cyrano, Sox2ot, TUNA, Emx2os, or MIAT, research continued to assess possible effects of the developmental teratogen nicotine on these RNA species in NSCs. Experimentation also considered the effect of nicotine and EtOH exposure in combination. Significant differences in expression were observed for all transcripts except Sox2ot (ANOVA: Malat1, $p = 0.032$; Cyrano, $p = 0.013$; Sox2ot, $p = 0.079$; TUNA, $p = 0.012$; Emx2os, $p = 0.038$; MIAT, $p = 0.013$). Consistent with the previous experiment, no effect of treatment was observed for expression of these lncRNAs following EtOH exposure

alone (LSD: Malat1, p = 0.736; Cyrano, p = 0.553; Sox2ot, p = 0.466; TUNA, p = 0.829; Emx2os, p = 0.536; MIAT, p = 0.326). However, exposure to nicotine resulted in a significant downregulation of all the lncRNAs except Sox2ot and Emx2os (LSD: Malat1, p = 0.023; Cyrano, p = 0.025; Sox2ot, p = 0.107; TUNA, p = 0.015; Emx2os, p = 0.051; MIAT, p = 0.042). Exposure to both nicotine and EtOH in combination also resulted in a significant downregulation of transcript expression for Cyrano (p = 0.027), TUNA (p = 0.017), and MIAT (p = 0.044). This downregulation was not significantly different from that observed with nicotine alone for these three RNA species (Cyrano, p = 0.979; TUNA, p = 0.953; MIAT, p = 0.980). Despite a significant ANOVA result for Emx2os, the only differences observed were between EtOH treatment and treatment with both nicotine and nicotine and EtOH in combination (LSD: EtOH v Nic, p = 0.016; EtOH v EtOH+Nic, p = 0.026). These results are presented graphically in Figure 3.

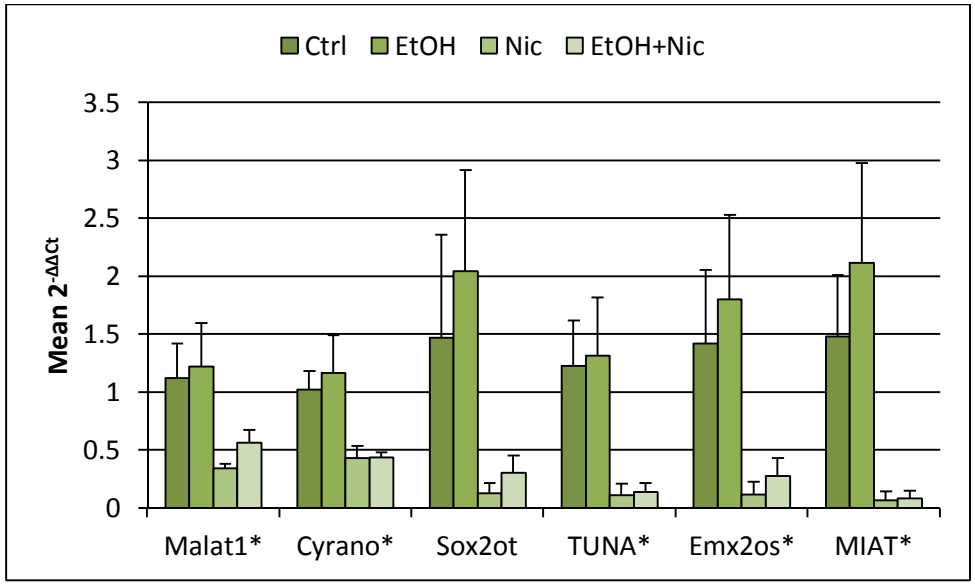

Figure 3. Expression of lncRNAs in EtOH- and Nicotine-Treated Neurospheres.

*Mean expression levels of six lncRNAs of interest under four treatment conditions. * Denotes statistical significance at α= 0.05.*

III.4 Prediction of lncRNA and miRNA Interactions

III.4.1 Teratogen-sensitive miRNAs

Previous research in neurosphere cultures and neurodevelopmental cancer cells determined the existence of several EtOH-sensitive and nicotine-sensitive miRNAs (Sathyan et al., 2007, Huang and Li, 2009, Balaraman et al., 2012). These include miR-140-3p, miR-153-3p, miR-21, miR-335-3p, and miR-9. Table 7 provides a brief overview of these five miRNAs to include their miRBase Accession numbers.

Table 7. Ethanol-Sensitive and Nicotine-Sensitive miRNAs.

miRNA	EtOH and Nicotine Effects in Neurospheres	miRBase Accession
mmu-miR-140-3p	Suppressed by 320 mg/dl EtOH (Balaraman *et al.* 2012), induced by 1μM nicotine (Balaraman *et al.* 2012).	MIMAT0000152
mmu-miR-153-3p	Suppressed by 320 mg/dl EtOH (Sathyan *et al.* 2007, Balaraman *et al.* 2012), induced by 1μM nicotine (Balaraman *et al.* 2012).	MIMAT0000163
mmu-miR-21	Suppressed by 320 mg/dl EtOH (Sathyan *et al.* 2007, Balaraman *et al.* 2012), induced by 60 mg/dl EtOH (Sathyan *et al.* 2007), induced by 1μM nicotine (Balaraman *et al.* 2012).	MIMAT0000530
mmu-miR-335-5p	Suppressed by 320 mg/dl EtOH (Sathyan *et al.* 2007, Balaraman *et al.* 2012), induced by 1μM nicotine (Balaraman *et al.* 2012).	MIMAT0000766
mmu-miR-9	Suppressed by 320 mg/dl EtOH (Sathyan *et al.* 2007, Balaraman *et al.* 2012), induced by 1μM nicotine (Balaraman *et al.* 2012).	MIMAT0000142

Using the RNAhybrid *in silico* analysis tool, the six lncRNAs of interest were assessed for potential binding sites with the seed regions of these EtOH- and nicotine-sensitive miRNAs. Of these miRNAs, miR-335-3p was the only one without any predicted interactions with the transcripts of interest. All of the other miRNAs had at least one predicted interaction. The EtOH/nicotine-sensitive miRNA with the most predicted interactions was miR-9. It had nine predicted interactions each with Malat1 and MIAT, five with TUNA, and one each with Cyrano and Sox2ot. miR-140-3p was

the only miRNA to have predicted interactions with all six lncRNAs of interest. All predicted EtOH/nicotine-sensitive miRNA/lncRNA interactions are presented in Figure 4.

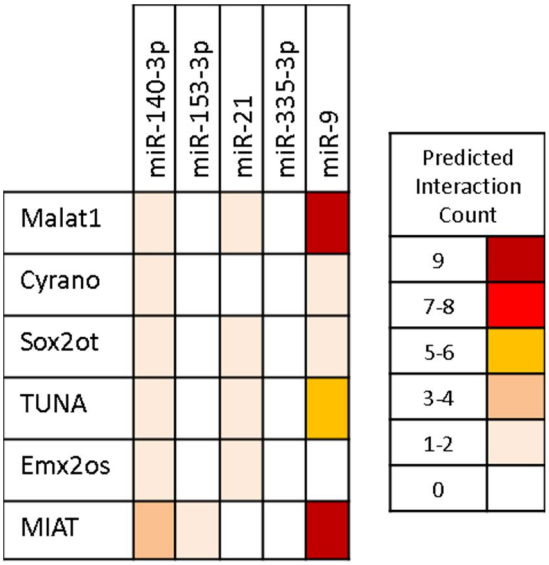

Figure 4. Predicted Interactions of EtOH-Sensitive miRNA and lncRNA.

Heatmap depicting predicted miRNA/lncRNA interactions between the six lncRNAs of interest and previously discovered EtOH-sensitive miRNAs.

III.4.2 Microarray Amplified miRNAs

Human miRNA Array Panels were run with pooled nuclear RIP and cytoplasmic RIP samples. The purpose of this was two-fold: 1) to find candidates for normalization standards for Ago2 RIP qPCR and 2) to determine miRNA species actively associated with RISC that could be assessed for predicted interactions with some of the lncRNAs of

interest. Only TUNA, Emx2os, and MIAT interactions were considered at this phase because these were the only lncRNAs to be assessed during Ago2 RIP qPCR.

Of the 52 miRNAs amplified from the nuclear RIP fraction, three were EtOH/nicotine-sensitive lncRNAs. These included miR-140-3p, miR-21, and miR-9. The only miRNAs without any predicted interactions with the three lncRNAs of interest were miR-21, miR-218-1*, miR-495, miR-543, and miR-598. In general, MIAT had the most predicted interactions. Those miRNAs exhibiting the greatest number of predicted interactions were let-7b (TUNA = 1, Emx2os = 3, MIAT = 12), miR-185* (TUNA = 12, Emx2os = 10, MIAT = 24), miR-141* (TUNA = 5, Emx2os = 2, MIAT = 6), miR-29b-1* (TUNA = 3, Emx2os = 6, MIAT = 13), miR-30a* (TUNA = 2, Emx2os = 5, MIAT = 13), miR-431* (TUNA = 0, Emx2os = 5, MIAT = 9), miR-760 (TUNA = 0, Emx2os = 7, MIAT = 18), miR-877* (TUNA = 2, Emx2os = 1, MIAT = 14), and miR-9 (TUNA = 5, Emx2os = 0, MIAT = 9). Full details regarding the 52 miRNAs amplified and their predicted interactions with TUNA, Emx2os, and MIAT can be found in Figure 5.

A total of 89 miRNAs were amplified following analysis of the pooled cytoplasmic RIP fraction via Human miRNA Array Panels. Once again, the EtOH/nicotine-sensitive miRNAs miR-140-3p, miR-21, and miR-9 were among those actively associated with the RISC component Ago2. Thirteen miRNAs showed no predicted interactions with TUNA, Emx2os, and MIAT. These included miR-10a*, miR-126*, miR-15b, miR-181a, miR-181b, miR-186, miR-21, miR-218-1*, miR-374b, miR-424, miR-543, miR-598, miR-9*, and miR-98. The miRNAs with the most predicted interactions were let-7b (TUNA: 1, Emx2os: 3, MIAT: 12), miR-103-2* (TUNA: 7,

Emx2os: 6, MIAT: 26), miR-130b* (TUNA: 2, Emx2os: 2, MIAT: 14), miR-141* (TUNA: 5, Emx2os: 2, MIAT: 7), miR-182* (TUNA: 2, Emx2os: 4, MIAT: 10), miR-29b-1* (TUNA: 3, Emx2os: 6, MIAT: 13), miR-30a* (TUNA: 2, Emx2os: 5, MIAT: 13), miR-486-3p (TUNA: 4, Emx2os: 8, MIAT: 10), miR-491-5p (TUNA: 8, Emx2os: 6, MIAT: 11), miR-708 (TUNA: 2, Emx2os: 1, MIAT: 18), miR-877* (TUNA: 2, Emx2os: 1, MIAT: 15), miR-9 (TUNA: 5, Emx2os: 0, MIAT: 9), and miR-93* (TUNA: 1, Emx2os: 3, MIAT: 9). Information on the other amplified miRNAs and their predicted interactions with TUNA, Emx2os, and MIAT can be found in Figure 6.

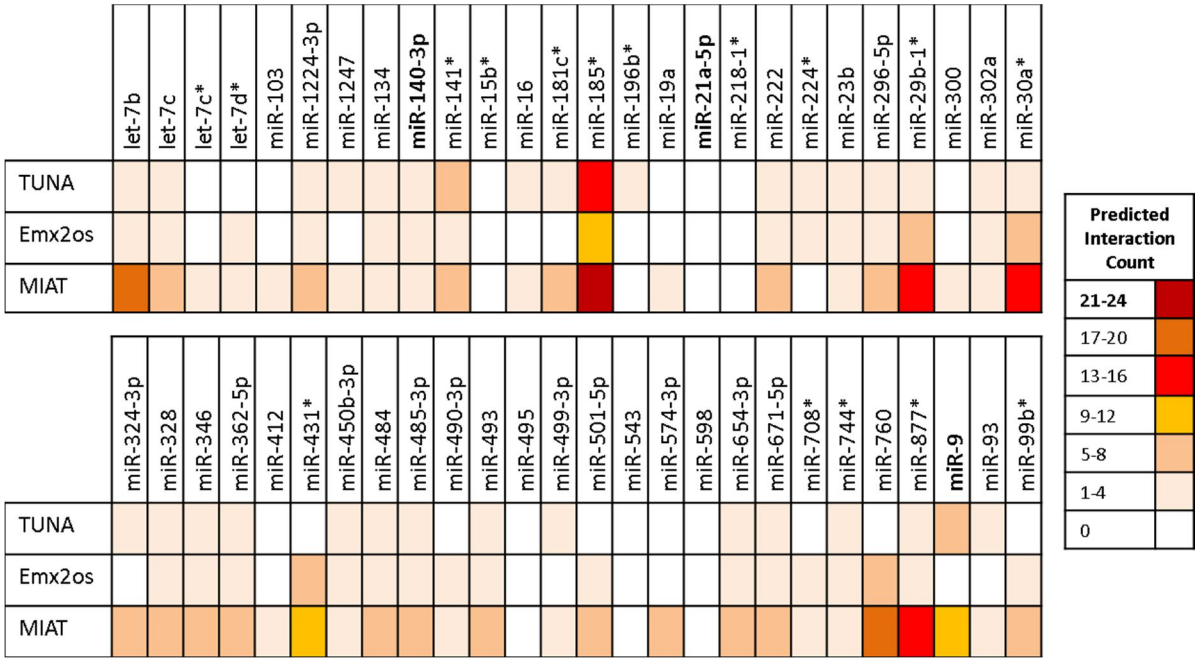

Figure 5. Predicted Interactions of miRNA and lncRNA in Nuclear RIP Fractions.

Heatmap depicting predicted miRNA/lncRNA interactions between TUNA, Emx2os and MIAT and the miRNAs amplified from a pooled nuclear RIP sample run on Human miRNA Array Panels.

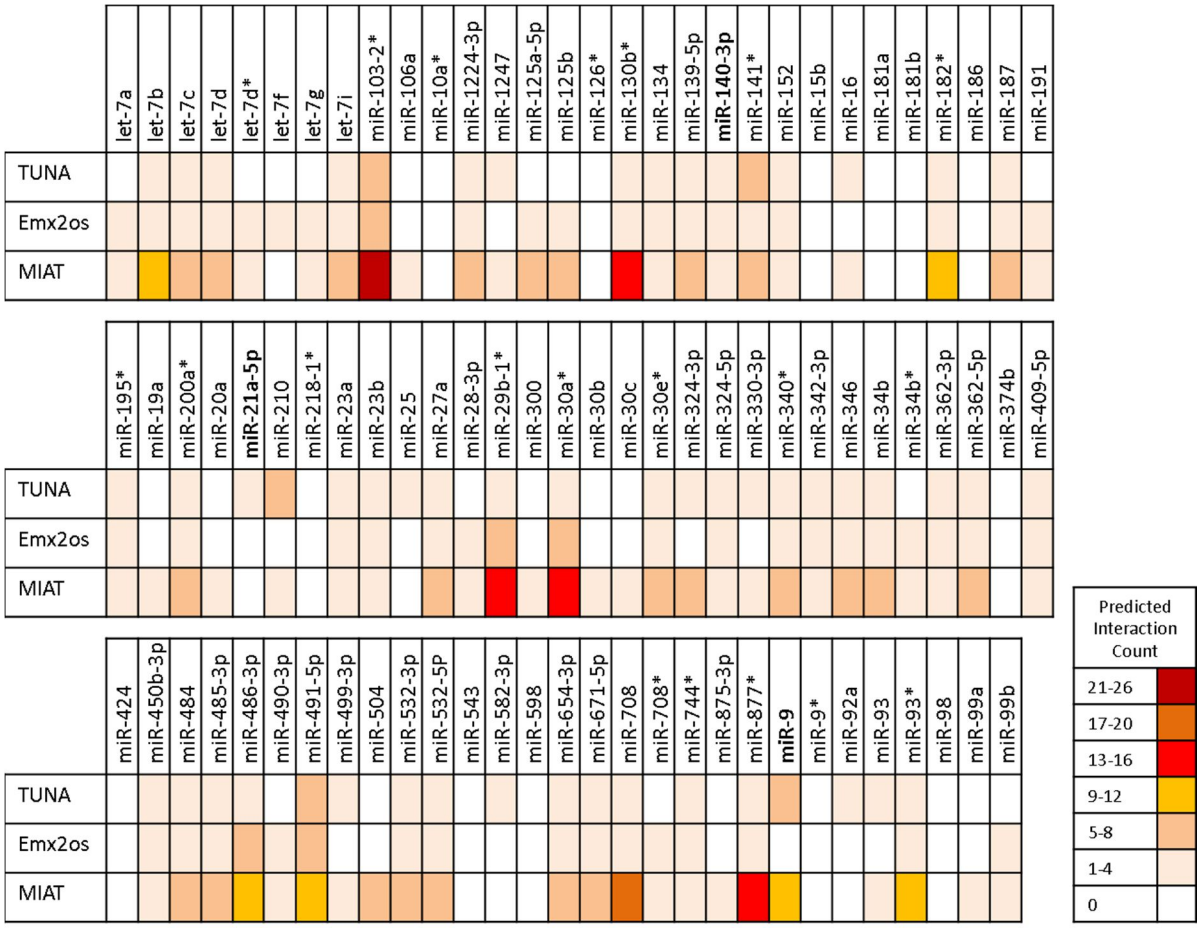

Figure 6. Predicted Interactions of miRNA and lncRNA in Cytoplasmic RIP Fractions.

Heatmap depicting predicted miRNA/lncRNA interactions between TUNA, Emx2os and MIAT and the miRNAs amplified from a pooled cytoplasmic RIP sample run on Human miRNA Array Panels.

When considering both nuclear RIP and cytoplasmic RIP samples, miR-218-1*, miR-543, miR-21, and miR-598 that amplified in Human miRNA Array Panels were the only miRNAs without any predicted interactions with the three lncRNAs of interest. EtOH/nicotine-sensitive miRNAs miR-140-3p and miR-9 were amplified in both fractions and exhibited predicted interactions with at least two of the three lncRNAs.

Table 8. Human miRNA Array Panel Amplified miRNAs

Amplified in Nuclear RIP Fraction Only	Amplified in Both Nuclear and Cytoplasmic RIP Fractions	Amplified in Cytoplasmic RIP Fraction Only	
miR-431*	miR-346	let-7a	miR-30e*
miR-196b*	miR-29b-1*	let-7d	miR-324-5p
miR-185*	miR-490-3p	let-7f	miR-330-3p
miR-328	let-7d*	let-7g	miR-340*
miR-412	let-7b	let-7i	miR-342-3p
miR-99b*	miR-30a*	miR-103-2*	miR-34b
miR-501-5p	miR-140-3p	miR-106a	miR-34b*
miR-181c*	let-7c	miR-10a*	miR-362-3p
miR-224*	miR-543	miR-125a-5p	miR-374b
miR-222	miR-1247	miR-125b	miR-409-5p
miR-15b*	miR-9	miR-126*	miR-424
miR-574-3p	miR-654-3p	miR-130b*	miR-486-3p
miR-302a	miR-744*	miR-139-5p	miR-491-5p
miR-296-5p	miR-21a-5p	miR-152	miR-504
miR-103	miR-708*	miR-15b	miR-532-3p
miR-495	miR-141*	miR-181a	miR-532-5p
let-7c*	miR-484	miR-181b	miR-582-3p
miR-760	miR-16	miR-182*	miR-708
miR-493	miR-362-5p	miR-186	miR-875-3p
	miR-1224-3p	miR-187	miR-9*
	miR-300	miR-191	miR-92a
	miR-23b	miR-195*	miR-93*
	miR-598	miR-200a*	miR-98
	miR-134	miR-20a	miR-99a
	miR-450b-3p	miR-210	miR-99b
	miR-324-3p	miR-23a	
	miR-93	miR-25	
	miR-218-1*	miR-27a	
	miR-19a	miR-28-3p	
	miR-671-5p	miR-30b	
	miR-877*	miR-30c	

Thirty-one miRNAs were amplified from both the nuclear and cytoplasmic RIP fractions. However, the miRNAs listed in Table 8 were not the only amplified miRNAs. A total of 37 miRNAs in the nuclear and cytoplasmic RIPs were amplified in the Human miRNA Array Panels but were either dead entries in miRBase or the human miRNA did

not have a mouse correlate. As such, the 52 miRNAs amplified from nuclear RIPs and the 89 miRNAs amplified from cytoplasmic RIPs considered were those with mouse correlates that closely matched the corresponding human miRNA. All miRNAs assessed for potential interactions with TUNA, Emx2os, and MIAT had Ct values less than 45 with a mean Ct of 35.89 for the nuclear RIP sample and 34.94 for the cytoplasmic RIP sample. The miRNA with the highest Ct value for nuclear RIPs was miR-493 while the lowest Ct value was for miR-346. For the cytoplasmic RIPs the highest Ct value corresponded to miR-491-5p and the lowest Ct was associated with miR-9.

III.5 Ago2 RNA Immunoprecipitation (RIP)

III.5.1 miRNA Microarray Panels and Normalization Standard Selection

The miRNAs amplified in the nuclear and cytoplasmic RIP fractions were assessed for use as possible normalization standards for the RIP fractions during Ago2 RNA immunoprecipitation qPCR analysis. While previous research (Chi et al., 2009) has provided some idea of miRNA transcripts predicted to associate with Argonaute proteins and RISC, no experimental evidence could be found in the primary literature regarding such associations in nuclear or cytoplasmic fractions. As such, it was necessary to determine RNA species present in the RIP fractions that could serve as normalization standard candidates.

Of the 110 miRNAs amplified in the Human miRNA Array Panels from the nuclear and cytoplasmic fractions, five were selected as potential normalization standards. These included miR-346, miR-490-3p, miR-877*, miR-9*, and miR-30a*. All of these miRNAs were amplified in both fractions except miR-9*, which was only found in the cytoplasmic RIP. Ct values for these miRNAs in the composite RIP samples were between 32 and 36. Commercially available primer sets from Exiqon were purchased for each of these miRNAs and assessed via qPCR with untreated control and fractioned RIP samples.

III.5.2 Western Blotting

Following co-IP with Ago2, Western blotting was performed to verify that Ago2 was successfully pulled down. According to the vendor of the anti-Ago2 antibody, a positive Western blot using their antibody yields a band at approximately 85 kDa. For both the nuclear and cytoplasmic RIP blots, a band was confirmed at ~85 kDa for all samples in which anti-Ago2 was the antibody used for pulldown (Figure 7). Further validating this result was the lack of such a band in lanes corresponding to RIP samples utilizing anti-tubulin as the antibody for pulldown. The same results were observed for the combined nuclear and cytoplasmic RIP gel. Blots for all three setups are presented in Figures 7 and 8. Based on these positive results, it was concluded that the Ago2 co-IPs were successful and all qPCR results could be interpreted as lncRNA expression levels associated with Ago2.

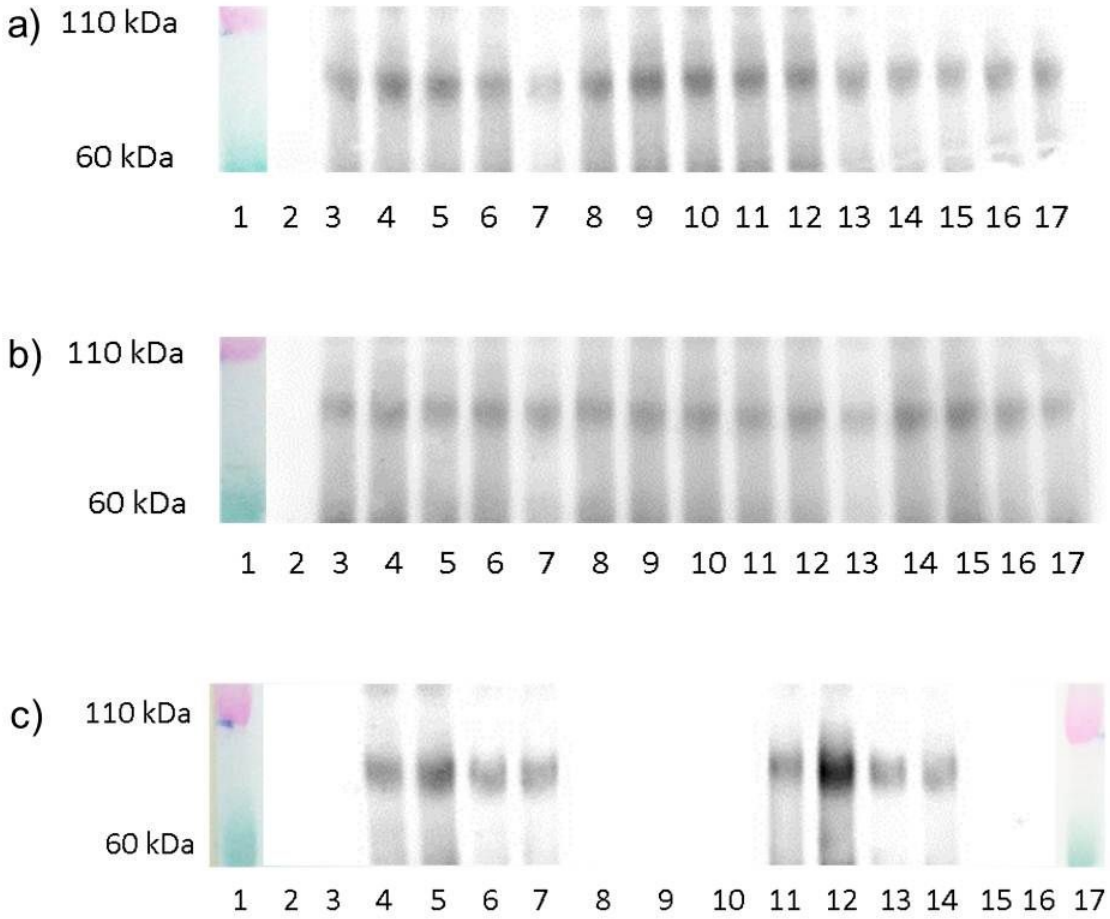

Figure 7. Nuclear and Cytoplasmic RIP Western Blotting.

(a) Cytoplasmic RIP blot probed with anti-Ago2 antibody, (b) NuclearRIP blot probed with anti-Ago2 antibody, (c) Western blot with treatment group representative samples from both nuclear and cytoplasmic RIPs. Colored sections showing the protein ladder are from images of the blots taken with a standard camera aligned with the blots.

III.5.3 qPCR

With strong evidence that the Ago2 RIP was successful, the remaining objectives were three-fold: 1) determine whether or not TUNA, Emx2os, or MIAT were present in the nuclear or cytoplasmic RIP fractions, 2) assess any possible effects of treatment on

interactions between these lncRNAs and Ago2, and 3) quantify the relative levels of these lncRNAs associated with Ago2 in each fraction. To these ends qPCR was performed on the nuclear and cytoplasmic RIPs, nuclear and cytoplasmic supernatants, and control samples.

Despite consistent amplification of all three lncRNAs in the whole cell-derived control samples, qPCR yielded inconsistent amplification of TUNA, Emx2os, and MIAT in all fraction and treatment group combinations. With a cutoff Ct value for amplification of 35, none of the lncRNAs of interest had enough samples in each treatment group and fraction combination amplify. This meant that no additional analyses could be performed. Thus, little could be concluded about potential interactions between the lncRNAs and Ago2 in NSCs. Additionally, nothing could be assessed with regard to effect of treatment on lncRNA/Ago2 complexation or localization.

Specifics of the amplification that was observed is detailed in Figure 8. In the nuclear RIPs, all three lncRNAs exhibited little to no expression. When all reactions were considered for the individual transcripts of interest, it was clear that TUNA had the greatest number of amplified wells. Yet, none of the control wells exhibited amplification except those for the tubulin pull-down control. Results of the cytoplasmic RIPs were similar with limited amplification overall and TUNA exhibiting the greatest number of amplified wells compared to the other two transcripts. MIAT showed absolutely no amplification in either of the RIP fractions. Conversely, both TUNA and Emx2os had at least two wells with reaction products in each of the RIP samples.

a

	Nuclear RIP				Nuclear Supernatant				Cytoplasmic RIP				Cytoplasmic Supernatant				Total	
	Controls	EtOH	Nic	Nic +EtOH	Controls	EtOH	Nic	Nic +EtOH	Controls	EtOH	Nic	Nic +EtOH	Controls	EtOH	Nic	Nic +EtOH	Amplified	Assessed
TUNA	1	2	4	3	4	11	7	12	2	5	2	1	2	6	11	9	82	264
Total	44								38									

b

	Nuclear RIP				Nuclear Supernatant				Cytoplasmic RIP				Cytoplasmic Supernatant				Total	
	Controls	EtOH	Nic	Nic +EtOH	Controls	EtOH	Nic	Nic +EtOH	Controls	EtOH	Nic	Nic +EtOH	Controls	EtOH	Nic	Nic +EtOH	Amplified	Assessed
Emx2os	0	1	1	0	6	9	7	8	2	0	0	0	5	0	7	9	55	297
Total	32								23									

c

	Nuclear RIP				Nuclear Supernatant				Cytoplasmic RIP				Cytoplasmic Supernatant				Total	
	Controls	EtOH	Nic	Nic +EtOH	Controls	EtOH	Nic	Nic +EtOH	Controls	EtOH	Nic	Nic +EtOH	Controls	EtOH	Nic	Nic +EtOH	Amplified	Assessed
MIAT	0	0	0	0	10	8	5	1	0	0	0	0	9	1	4	6	44	258
Total	24								20									

Figure 8. Amplification of lncRNAs in Ago2 RIP-Derived Samples.

Set of tables outlining the specific amplification from the nuclear and cytoplasmic Ago2 fraction and treatment group combinations for TUNA (a), Emx2os (b), and MIAT (c). All values indicate the number of wells.

Amplification in the supernatants remained inconsistent for all three transcripts. However, the total number of amplified wells observed for each of the lncRNAs was greater than that seen with the RIPs. In the nuclear supernatants, amplification of TUNA wells for the ethanol and ethanol + nicotine treatment groups was nearly complete. Amplification in the controls and nicotine samples were also more consistent than in the RIPs. The cytoplasmic supernatant fractions also yielded greater overall amplification. Consistency of amplification was little improved. Once again, TUNA had more amplified wells than Emx2os and MIAT. Despite this, overall amplification of TUNA in the cytoplasmic supernatants was slightly less than that observed in the nuclear supernatants. Unlike in the two RIP fractions, MIAT amplification occurred. This amplification was mainly observed in the nuclear supernatant with at least one well amplified in each treatment group.

It was unclear whether or not the limited and inconsistent amplification observed for TUNA, Emx2os, and MIAT was unique to these transcripts or if this was indeed a global effect on all RNA.. If it were observed for all RNA species it might suggest a general loss or degradation of RNA at some point in the experimental process. As such, attention was shifted to the RNA species which were chosen as normalization standards for each fraction. For the cytoplasmic supernatant samples, the ribosomal RNA 18S was to be employed. It was successfully amplified in all treatment groups including controls. The small nuclear RNA U6 was intended to serve as a nuclear supernatant normalization standard. As with 18S, U6 was expressed in all controls and supernatants. However, it was more highly expressed in whole cell controls than in any of the fractions. As

described above, several miRNAs were assessed as possible normalization standards for the RIP samples. After some preliminary qPCR runs, miR-490-3p was selected as the normalization standard for both the nuclear and cytoplasmic RIPs. In the nuclear RIPs, this RNA species was amplified in all whole cell controls and in all RIP samples except the untreated tubulin RIP control and one nicotine + EtOH-treated sample. For the cytoplasmic RIPs, miR-490-3p was expressed in all whole cell controls, the untreated tubulin RIP, and all RIP treatment groups. However, it was not amplified in two nicotine-treated RIPs or in one sample from both the EtOH-treated and the nicotine + EtOH-treated groups. These results strongly suggested that the inconsistent amplification seen with the three lncRNAs was not universal for all RNA. Additionally, it does not appear that this inconsistent amplification was due to loss of RNA species during the extraction, fractionation, or RIP steps.

CHAPTER IV

SUMMARY AND DISCUSSION

The aims of this thesis work were multifold. First, determine the expression levels of Malat1, Cyrano, Sox2ot, TUNA, Emx2os, MIAT, and GM7854 in developing NSCs. Second, assess whether or not expression levels of these lncRNAs change in NSCs following exposure to ethanol and/or nicotine. Third, investigate if any of the lncRNAs interact with Argonaute 2 (and miRNAs by proxy) and where within neurosphere cells these complexes localize. Finally, determine whether or not treatment with ethanol and/or nicotine results in changes in interactions between the lncRNAs and Ago2 and compartmentalization of these complexes. Discussion of the major findings regarding each of these aims follows.

IV.1 lncRNAs in Fetal Cortical NSCs: Validated Primers and Baseline Levels of Expression

While preparing to undertake this thesis work an initial difficulty was the lack of previously designed and validated primer pairs. Despite a search of the primary literature, few prior investigations of the seven lncRNAs of interest (Malat1, Cyrano, Sox2ot, TUNA, Emx2os, MIAT, and GM7854) yielded reliable primers for these transcripts. Reasons for this fell into one of two categories: 1) There was no previous research assessing expression of these lncRNAs via qPCR or 2) Provided primer pair

sequences were designed for non-mouse models and proved to have suboptimal specificity. For instance, Ulitsky et al. (2011) details expression of both Cyrano and TUNA in zebrafish embryos and investigates the functional roles of these two lncRNAs in this model organism. However, all of the expression data is based on *in situ* hybridization so no primers were provided. In Tano et al. (2010), expression of Malat1 was assessed in human A549 lung cancer cells and primer pairs were provided in the supplemental information. When these primers were assessed via PrimerBLAST for specificity to the mouse transcript, too many non-specific matches were returned for the primer set to be deemed useful. In the case of GM7854, no research had been conducted on the transcript so finding validated primer pairs was not an option. A final issue with the available primer pairs was that PrimerBLAST analysis revealed that they did not flank conserved regions of the target transcripts. Encompassing these regions in the amplicon was a priority because their inclusion would likely improve specificity while also increasing the relevance of experimental results to other species. Therefore, it was necessary to design primer pairs for all of the lncRNAs of interest and to validate their target specificity before any other experimentation could proceed.

Six of the seven primer pairs designed for use in this work proved to be highly specific to the intended targets; only GM7854 was dropped from subsequent experimentation. Sequencing of the amplified qPCR products of primers for Malat1, TUNA, Emx2os, and MIAT revealed sequence cover matches of at least 70% and identity matches of at least 85% when compared with the design sequences via BLAST. Interestingly, following BLAST analysis, the transcript sequence used to design the

Cyrano primers did not show any direct cover or identity matches with the qPCR products. However, the transcripts with the highest sequence matches to these qPCR products exhibited at least 96% cover and 99% identity matches with the Cyrano sequence used in primer design. Sox2ot qPCR primer products also showed no BLAST match to the design sequence. The products did exhibit a 77% cover match and a 98% identity match with a different transcript designated as the OTTMUST00000095020.1/Sox2ot gene, however. BLAST analysis of this transcript sequence with the design sequence resulted in a cover match of only 19%. However, this 19% of shared sequence had a 100% identity match to the Sox2ot transcript used in primer design.

As was briefly discussed in the Experimental Results chapter, the most likely explanation for this seeming lack of specificity is that the primers amplified a different isoform of Sox2ot. Evidence suggests there are 16 different Sox2ot isoforms in *M. musculus*, resulting from multiple transcription start sites spread across five exons (Amaral et al., 2011, Kersey et al., 2012). Since all of the primer pairs designed for this thesis work sought to capture a highly conserved region of the transcript of interest, it would make sense that the products could represent several of the 16 isoforms. With that being said, the isoform represented by the original design sequence may indeed have been among the amplified products but was not the transcript amplified by this primer pair. This might suggest that the various Sox2ot isoforms could be differentially expressed depending on cell or tissue type, developmental context, or any number of other factors. As such, an interesting avenue for additional research could be to assess

the expression levels of the individual Sox2ot isoforms instead of overall Sox2ot expression, as was done in these investigations.

Regardless, a major contribution of the work presented in this thesis is the design and validation of these six primer pairs. There are now reliable primer sequences that include conserved regions of each transcript available for other investigators to use in their experiments. With these primer pairs others can immediately begin projects on Malat1, Cyrano, Sox2ot, TUNA, Emx2os, or MIAT without spending time and effort on the design and validation of their own original primer sets. Hopefully this will increase overall research on these six lncRNAs by making it easier to study them. This is especially important for Cyrano, TUNA, and Emx2os which have received limited attention to date.

Moving past the primers and on to the major aims of this thesis, results of these experiments indicate that Malat1, Cyrano, Sox2ot, TUNA, Emx2os, and MIAT are all expressed in NSCs derived from the developing cortex of GD 12.5 mice. All six lncRNAs were amplified in untreated NSCs. Average relative expression levels of between 1.4 and 2.4 ($2^{-\Delta\Delta Ct}$) were obtained for these RNA species when normalized to the geometric mean of HPRT1 and PPIA. Another experiment in this thesis work yielded slightly different relative expressions for the six lncRNAs in untreated NSCs utilized as controls. Not counting normal variation in expression of transcripts in each flask of cultured neurospheres, this discrepancy is likely owed to two factors. First, the normalization standards used in the two experiments were different; the subsequent experiment used the geometric mean of HPRT1, PPIA, and GAPDH expressions.

Second, the sample size used to obtain the expression levels reported above was larger than that used in later experiments. Therefore, it is reasonable to believe that the expression levels obtained in the initial experiment are a better representation of actual expression levels of Malat1, Cyrano, Sox2ot, TUNA, Emx2os, and MIAT in this model system. With that being said, the differences in relative expression levels for each lncRNA obtained in the two experiments was less than 1.0 ($2^{-\Delta\Delta Ct}$).

The results of these experiments do not represent the first reports of Malat1, Cyrano, Sox2ot, TUNA, Emx2os, or MIAT in neural tissues and stem cells. Multiple studies have detailed their expression in the developing mouse nervous system, mouse ESCs, and in the adult mouse brain (Blackshaw et al., 2004, Sone et al., 2007, Dinger et al., 2008, Mercer et al., 2008, Amaral et al., 2009, Bernard et al., 2010, Mercer et al., 2010, Rapicavoli et al., 2010, Sheik Mohamed et al., 2010, Spigoni et al., 2010, Nakagawa et al., 2012, Onoguchi et al., 2012, Zhang et al., 2012, Aprea et al., 2013, Barry et al., 2013, Boraska et al., 2014). For instance, TUNA expression was observed in undifferentiated mouse embryonic stem cells and upregulated in these cells under a neural differentiation regime (Lin et al., 2014). Sheik Mohamed et al. (2010) found that MIAT was expressed in E14 mouse ESCs. Another study determined that Malat1 was present in adult mouse cortex, cerebellum, and hippocampus via *in situ* hybridization (Nakagawa et al., 2012). Additionally, Sox2ot is expressed in stem cells and proliferating progenitor cells from the adult mouse subventricular zone (Amaral et al., 2009). Expression of the lncRNAs of interest has also been observed in neuroblastoma cell lines, the brains of patients suffering from neurological diseases, the brains of drug

abusers, the normal adult nervous system, and neural tissues of chicken and zebrafish embryos (Albertson et al., 2006, Amaral et al., 2009, Koshimizu et al., 2010, Michelhaugh et al., 2011, Tsuiji et al., 2011, Ulitsky et al., 2011, Clark et al., 2012, Kryger et al., 2012, Schor et al., 2012, Barry et al., 2013, Valdiglesias et al., 2013, Yang et al., 2013, Boraska et al., 2014, Ishizuka et al., 2014, Lin et al., 2014, Yan et al., 2014).

Despite these studies reporting expression of the lncRNAs of interest in a variety of neural tissues and developmental contexts, only two of the transcripts have previously been assessed in cells of the developing cortex. Spigoni et al. (2010) observed expression of Emx2os in periventricular cortical precursor cells derived from the brains of E12.5 mouse embryos. Another study found that MIAT expression was present in progenitor cells derived from the lateral cortex of E14.5 mice (Aprea et al., 2013). As such, the findings of this thesis support the results of previous studies on MIAT and Emx2os expression in cortical NSCs and serve as the first direct evidence for Malat1, Cyrano, Sox2ot, and TUNA expression in proliferative cells of the fetal cortex.

Yet, the studies by Aprea et al. (2013) and Spigoni et al. (2010) also observed differential expression of MIAT and Emx2os in proliferating vs. differentiating progenitors. These findings led researchers to surmise that these transcripts play roles in the regulation of stem cell maintenance and neural lineage specification. In particular, Aprea et al. (2013) observed subtle differential expression patterns for MIAT between proliferative progenitors, differentiating progenitors, and new neurons in E14.5 mouse cortex. Results indicated that MIAT is upregulated in the differentiating progenitor population and this upregulation is necessary for the fate determination of these cells as

neural progenitors. Other publications on MIAT, as well as studies of TUNA and Sox2ot, report similar regulatory changes in transcript expression linking transcripts to pluripotency maintenance, cell fate determination, and early neuron survival (Amaral et al., 2009, Mercer et al., 2010, Rapicavoli et al., 2010, Sheik Mohamed et al., 2010, Lin et al., 2014).

Previous research in the fetal mouse cortical neurosphere model system employed in this thesis has determined that individual neurospheres are composed of several subpopulations of cells ranging from multipotent stem cells to proliferative and basal progenitors to differentiating progenitors specified to a neural progenitor fate (Santillano et al., 2005, Miranda et al., 2008). The neurosphere cultures are also easily differentiated into bipolar and multipolar cortical neurons when exposed to a mitogen-withdrawal media regime (Santillano et al., 2005, Miranda et al., 2008, Camarillo and Miranda, 2008). Furthermore, flow cytometry-based cell sorting can be used to distinguish cellular subpopulations based on cell surface markers (Santillano et al., 2005, Tingling et al., 2013). Therefore, this model system could provide an excellent opportunity to further characterize differential expression patterns of the six lncRNAs of interest in cell types present throughout the process of cortical neurogenesis. Such information would be especially beneficial for the under-studied transcripts Cyrano, TUNA, and Emx2os.

IV.2 lncRNA Expression and the Effects of Ethanol and Nicotine

The effect of toxic compounds on lncRNAs in a neurodevelopmental context has received limited investigation. Actually, relatively few researchers have considered the impacts of toxins on expression of lncRNAs regardless of tissue type or life stage. This knowledge gap is surprising given the prevalence of molecular toxicology, including a large body of work outlining the impacts of various compounds on miRNA expression (Pogribny et al., 2007, Ichi et al., 2010, Lema and Cunningham, 2010, Shookhoff and Gallicano, 2010, Fukushima et al., 2011, Halappanavar et al., 2011, Aluru et al., 2013, Yokoi and Nakajima, 2013, Taki et al., 2014, Oh et al., 2015, Lu et al., 2016). To better illustrate this, consider a search of the PubMed database. When the search terms "long non-coding RNA" and "toxicology" are entered only 57 publications are returned. In comparison, the same search with "microRNA" substituted for "long non-coding RNA" yields 524 publications.

Despite the limited publication history, several developmental toxicology studies involving lncRNA. For the most part, these publications involve H19 and Xist, some of the first members of this ncRNA class to be studied. For example, several investigators have reported epigenetic effects of prenatal alcohol exposure on H19 gene methylation in gametes and mouse embryos (Haycock and Ramsay, 2009, Ouko et al., 2009, Stouder et al., 2011). A study by Kumamoto and Oshio (2013) found evidence for downregulation of Xist in the forebrains of female postnatal mice exposed to bisphenol A during fetal development. However, there was one study on an lncRNA other than

H19 or Xist. Nan et al. (2016) determined that lead-induced nerve injury reduces expression of the lncRNA Uc.173 in the hippocampus and serum of mice. Thus, the experiments undertaken in this thesis build on these studies and expand research on the developmental toxicology of lncRNAs. More specifically, this research constitutes the first investigation of specific toxicological effects on lncRNA expression in NSCs of the developing cortex.

Ethanol and nicotine were chosen as the toxins of interest for this thesis for five major reasons. First, both are highly addictive neuroactive compounds commonly used and abused throughout the world (Kandel et al., 1997, Weiss and Porrino, 2002, Vengeliene et al., 2008, Fagerstrom and Furberg, 2008, Benowitz, 2009, Lingford-Hughes et al., 2010, Dutta et al., 2014). As a result, it is not unusual for some women to continue their use well into pregnancy (Center for Behavioral Health Statistics and Quality, 2014). Second, ethanol and nicotine are often co-abused, even during pregnancy (Mick et al., 2002, Funk et al., 2006, Duncan et al., 2015, Center for Behavioral Health Statistics and Quality, 2015). Third, previous research indicates that other noncoding RNA classes are differentially regulated following ethanol and nicotine exposure (Sathyan et al., 2007, Wang et al., 2008, Huang and Li, 2009, Wang et al., 2009, Guo et al., 2010, Balaraman et al., 2012, Guo et al., 2012, Tal et al., 2012, Soares et al., 2012, Ng et al., 2013, Takahashi et al., 2013, Qi et al., 2014, Taki et al., 2014). For example, one study found that Malat1 was significantly upregulated in the brains of alcoholics (Kryger et al., 2012). Although not a direct study on the impacts of nicotine on noncoding RNA, another investigation identified 12 long noncoding RNA transcripts

(termed long stress-induced noncoding transcripts, or LSINCTs) that were upregulated in normal human bronchial epithelial cells exposed to the nicotine-derived tobacco carcinogen NNK (Silva et al., 2010). Fourth, alcohol and nicotine are linked to disruptions in neuroanatomy and behavioral outcomes in exposed offspring. It is widely known that ethanol exposure during gestation is associated with fetal alcohol spectrum disorder and its suite of physical and behavioral deficits (Haycock, 2009, Alfonso-Loeches and Guerri, 2011, Laufer et al., 2013). Additionally, some investigators have described specific disruptions to neural crest cells and cortical precursors due to *in utero* alcohol exposure (Miller and Dow-Edwards, 1988, Rovasio and Battiato, 2002, Tsai et al., 2014). Similarly, nicotine use during pregnancy is associated with a high incidence of ADHD and emotional problems among offspring (Slotkin, 1998, Mick et al., 2002, Roza et al., 2007, Cents et al., 2012). Prenatal nicotine exposure is also linked to reduced offspring head size, an early switch from replication to differentiation of cells in the developing CNS, and impairment of the autonomic nervous system resulting in a higher incidence of sudden infant death syndrome, or SIDS (Slotkin, 1998, Atluri et al., 2001, Roza et al., 2007, Takarada et al., 2012, Lee et al., 2014). The fifth and final reason for assessing ethanol and nicotine effects on the developing cortex is that preliminary *in silico* analysis for this thesis predicted multiple potential seed-region binding sites for ethanol-sensitive and nicotine-sensitive miRNAs within the sequences of Malat1, Cyrano, Sox2ot, TUNA, Emx2os, and MIAT.

Despite this promising information, results of the subsequent experiments indicate no significant dysregulation of the six lncRNAs of interest in NSCs following

exposure to 320 mg/dl ethanol. This holds true for the initial assessment of ethanol treatment alone as well as for the secondary assessment during which effects from nicotine treatment and treatment with ethanol and nicotine in combination were also probed. Once again, the results of the initial experiment are taken to be more meaningful as the sample size is larger. These results suggest that ethanol does not affect expression of these six transcripts. Unlike ethanol, exposure to 1 μM nicotine significantly reduced expression of all transcripts except Sox2ot and Emx2os. As such, this research provides the first evidence that Malat1, Cyrano, TUNA, and MIAT are dysregulated in NSCs exposed to nicotine.

The results of combined exposure to ethanol and nicotine on the transcripts of interests are especially interesting. Similar to the effects of nicotine exposure alone, the combination of 320 mg/dl ethanol and 1 μM nicotine yielded a significant downregulation of each lncRNA except Sox2ot, Emx2os, and Malat1. In fact, there was no significant difference between the effects of nicotine treatment alone and treatment with both ethanol and nicotine for Cyrano, TUNA, and MIAT. One previous study has assessed how concurrent ethanol and nicotine exposure impacts noncoding RNA expression during cortical development. Balaraman et al. (2012) reported that exposure to ethanol alone resulted in a significant downregulation of miR-9, miR-21, miR-153, miR-335-3p, and miR-140-3p. Conversely, nicotine exposure alone led to upregulation of these miRNAs. When neurosphere cultures were exposed to the two teratogens simultaneously, their opposing actions caused levels of these miRNAs to normalize. Prior to beginning the experiments described in this thesis, it seemed likely that if the

lncRNAs of interest mediated the expression of these ethanol- or nicotine-sensitive miRNAs the impacts of EtOH and nicotine on these transcripts would be opposite that observed by Balaraman and colleagues. Additionally, co-exposure would lead to a similar normalizing effect. However, it has been determined that Cyrano, TUNA, and MIAT levels in NSCs remain dysregulated when exposed to nicotine and ethanol in combination.

Given the limited understanding of the functional means by which these two compounds impact lncRNA levels in this model system, there was no reason to assume that these lncRNAs would behave in the same fashion as miR-9, miR-21, miR-153, miR-335-3p, and miR-140-3p. Yet, it is interesting that no recovery was observed whatsoever for three of the four nicotine-sensitive lncRNAs. Considering that ethanol maintained expression of these lncRNAs within the range observed in untreated controls, it would seem likely that combined exposure would at least result in an expression level intermediate to those observed for ethanol and nicotine individually. This would indicate an additive and inverse regulatory effect of these two teratogens on expression of the lncRNAs, similar to that observed by Balaraman et al. (2012). However, the fact that combined ethanol and nicotine exposure results in expression levels nearly identical to those observed with nicotine alone for Cyrano, TUNA, and MIAT indicates that the effects of ethanol and nicotine on these transcripts are completely decoupled; co-abuse will not counteract dysregulation of the lncRNAs of interest due to nicotine exposure.

Interestingly, it does appear that the actions of ethanol and nicotine on Malat1 expression could be related. The average relative expression for Malat1 obtained from

combined exposure to ethanol and nicotine is roughly 51% of the average relative expression of this transcript in untreated NSCs. Alone, ethanol does not yield any dysregulation while expression of Malat1 is significantly reduced by nicotine treatment. Based on research by Leucci et al. (2013) it is possible that this relationship is the result of miR-9 regulating Malat1 transcript levels. According to their report, Leucci and colleagues (2013) found evidence that miR-9 and Malat1 interact via the binding of miR-9-guided RISC complexes at two canonical sites in the Malat1 sequence. This leads to Malat1 degradation in the nucleus. It is possible then, that nicotine exposure increases miR-9 levels, as described by Balaraman et al. (2012), and this subsequently reduces Malat1 levels in cortical NSCs. However, when ethanol exposure occurs simultaneously, the downregulation of miR-9 by that compound partially ameliorates the action of nicotine leading to a less potent downregulation of Malat1. Clearly, more work would need to be done before the existence of such a relationship could be confirmed in this context. Regardless, it is an interesting possibility that warrants further investigation, especially since Leucci et al. (2013) also found that Ago2 was a component of the RISC complexes involved in miR-9-mediated Malat1 degradation. With that being said, future research should also attempt to uncover the mechanisms by which nicotine downregulates Cyrano, TUNA, and MIAT.

For ethanol and nicotine treatment alone and in combination, it would be reasonable to investigate how other concentrations might effect lncRNA expression. Yet, care would need to be taken to ensure that assessments consider real-world correlates of exposure to developing organisms as well as ethanol and nicotine levels that could

realistically be achieved in pregnant females. If concentrations tested are so high that a person could not survive with the equivalent BAC or blood nicotine level, then such investigations carry little meaning. The concentration of 320 mg/dl ethanol (BAC= 0.32%) used in this thesis falls within the range observed in alcoholics (Gottesfeld et al., 1990, Adachi et al., 1991). Although it is possible for a woman to attain a higher concentration in her system, 320 mg/dl nicely approximates the BAC of individuals at highest risk for continuing alcohol use during pregnancy. Similarly, the 1 μM nicotine concentration assessed in this thesis represents a reasonable approximation of the blood nicotine levels attainable by smokers (Russell et al., 1980, Benowitz and Jacob, 1984, Williams et al., 2010, Jarvis et al., 2014).

Since the experiments in this thesis were only performed with a single ethanol and nicotine concentration, it could be argued that different effects of treatment may be observed at either higher or lower concentrations. In preliminary analyses NSCs were also exposed to 120 mg/dl ethanol (BAC= 0.12%), which roughly approximates BACs achievable with binge drinking (Gottesfeld et al., 1990, Adachi et al., 1991). Results of these experiments revealed no significant effect of treatment on any of the lncRNAs. However, since even small amounts of alcohol consumption during pregnancy can result in offspring with symptoms on the fetal alcohol syndrome spectrum, it may be wise to assess effects of concentrations below 120 mg/dl. At this time, ethanol concentrations higher than 320 mg/dl have not been assessed in this model system and, thus, the possibility that an effect of treatment could exist at higher concentrations cannot be dismissed. With regard to nicotine, effects of concentrations both higher and lower than

1 μM have yet to be considered. Again, it is important that any future research assessing the effects of higher concentrations of either ethanol or nicotine consider concentrations that approximate physiologically relevant BACs and blood nicotine levels.

Regardless of whether or not ethanol and/or nicotine exposure play a role in the expression levels of Malat1, Cyrano, Sox2ot, TUNA, Emx2os, and MIAT in mouse fetal NSCs, this collection of experiments is the first to investigate how these compounds affect lncRNAs in the developing nervous system. Ideally these findings will spur others to further explore the effects of nicotine and ethanol on lncRNA expression as well as the impacts of other toxins.

IV.3 lncRNAs and Ago2 Complexation: Expression Levels, Compartmentalization, and the Effects of Ethanol and Nicotine

The remaining aims of this thesis involve the determination of whether or not the lncRNAs actively associate with Ago2 in NSCs, where these lncRNA/Ago2 complexes localize within cells, and if ethanol and nicotine exposure disrupt normal patterns of association and compartmentalization. Unlike the previous studies, a subset of the six lncRNAs of interest were considered in this phase of experimentation. Only TUNA, Emx2os, and MIAT were assessed in nuclear and cytoplasmic Ago2 RIP fractions. This decision was in part due to the feasibility of undertaking such assessments. To investigate expression of a single lncRNA in each RIP-generated sample run in triplicate, it takes a total of 240 reactions. Therefore, assessing all six lncRNAs of

interest, not including potential normalization standard transcripts, would require 1440 reactions. However, the selection of these three lncRNA as the focus of the RIP experiments has more to do with the results of the expression level studies involving ethanol and nicotine exposure. TUNA, Emx2os, and MIAT are representative of all the lncRNAs considered in this work with regard to three factors: effect of treatment on expression, prior evidence of a compartmentalization pattern, and body of research on the transcript. TUNA exhibits significant downregulation as a result of nicotine treatment and it has received little attention in the primary literature with only two papers published to date. However, one of these studies determined that TUNA localizes to both the nucleus and cytoplasm of mouse embryonic stem cells (Lin et al., 2014). Like TUNA, MIAT shows an effect of treatment with nicotine exposure. Yet, significantly more research has been published regarding MIAT (approximately 15 publications), to include evidence suggesting that it is enriched in the nucleus (Sone et al., 2007, Rapicavoli et al., 2010, Ip and Nakagawa, 2012, Ishizuka et al., 2014). Emx2os is the only lncRNA assessed in Ago2 RIP fractions that is not downregulated following nicotine exposure. While it is the subject of limited study, three investigations have dealt with Emx2os compared to only two for TUNA. Despite that, no localization data has been generated. Thus, by selecting these lncRNAs, the subsequent experiments considered two teratogen-sensitive lncRNAs and one unaffected "control" of sorts. Additionally, assessment of TUNA and Emx2os serve to further expand the knowledge base for these noncoding RNAs. With the compartmentalization pattern evidence documented by other researchers for MIAT and TUNA, their assessment in these

experiments allow for the opportunity to determine agreement with the primary literature and potentially better assess disruptions to localization as a result of treatment.

If evidence for complexation between the three lncRNAs of interest and Ago2 was discovered, it would provide the preliminary evidence needed to suggest that these noncoding transcripts were interacting with RISC and, therefore, with miRNAs in the developing cortex. The impetus for such investigations stems from account in the primary literature detailing regulatory interactions between lncRNAs and miRNAs. Commonly this involves regulation of an lncRNA by a miRNA via RNA induced silencing. An example of this type of interaction between Malat1 and miR-9 was presented in the last section (Leucci et al., 2013). More recently, Wang et al. (2015) have also described how miR-101 and miR-217 silence Malat1 in esophageal cancer cells via RISC. The other lncRNA/miRNA interaction that has been gaining attention in the past few years involves lncRNAs acting as competing endogenous RNAs (ceRNAs), or miRNA sponges. In this case, the lncRNA contains at least one binding site for a miRNA and competitively binds and sequesters copies of the transcript; thus, reducing regulatory effects on the miRNA targets (Cesana et al., 2011, Cesana and Daley, 2013, Hansen et al., 2013, Liu et al., 2014, Zhou et al., 2014). This past year, researchers reported evidence of ceRNA roles for both Malat1 and MIAT. Yan et al. (2015) observed that MIAT overexpression partially rescued VEGF mRNA from repression by miR-150-5p by binding the transcript in vascular epithelial cells. Similarly, Malat1 promotes myogenesis by easing miR-133-mediated regulation of the SRF transcription factor through competitively binding of this miRNA (Han et al., 2015).

Another reason lncRNA/Ago2 complexation was assessed as a proxy for lncRNA/miRNA associations in this thesis stems from the results of preliminary *in silico* analyses. RNA Hybrid was used to determine the potential for interactions between the six lncRNAs of interest and known ethanol- and nicotine-sensitive miRNAs. Previous lab members cited the existence of several ethanol-sensitive miRNAs including miR-335-3p, miR-21, miR-153-3p, and miR-9 (Sathyan et al., 2007, Balaraman et al., 2012). In addition evidence from the primary literature pointed to miR-140-3p as a nicotine-sensitive miRNA (Huang and Li, 2009). According to the *in silico* results, miR-335-3p was the only teratogen-sensitive miRNA exhibiting no predicted seed region-mediated interactions with TUNA, Emx2os, or MIAT. Conversely, miR-140-3p had predicted binding sites with all three transcripts. Thus, the potential for interactions between these lncRNAs and miRNAs seemed plausible.

Unfortunately, qPCR results indicate no significant or consistent expression of these three transcripts in nuclear or cytoplasmic Ago2 RIP samples. This pattern is seen in untreated RIP controls and across each of the three treatment groups (ethanol, nicotine, ethanol + nicotine). All three lncRNAs are amplified consistently in whole cell controls, however. Thus, there is no evidence suggesting interaction between Ago2, TUNA, Emx2os, or MIAT in NSCs. This finding can be extended to a lack of evidence for interactions between these lncRNAs and miRNAs, including those exhibiting ethanol- and nicotine-sensitivity. However, it is important to keep in mind that only those interactions between these noncoding RNAs and Ago2 were probed in these experiments despite there being three other Argonaute proteins in mammals (Hutvagner

and Simard, 2008, Ender and Meister, 2010). Since RIPs targeting these other Agos were not performed and assessed for TUNA, Emx2os, or MIAT expression, it is still possible that these transcripts could mediate interactions between the lncRNAs and miRNAs. For that reason, a logical next step for this research would involve expanding it to consider the remaining Ago proteins to determine whether or not they might mediate interactions between TUNA, Emx2os, or MIAT and miRNAs.

While it is possible that TUNA, Emx2os, or MIAT may interact with miRNAs via one of these other Ago proteins, it is also possible that they could play a role in the interactome of ethanol- or nicotine-sensitive miRNAs at some other level of regulation. Since this experimentation does not indicate a role for these lncRNAs in direct post-transcriptional associations with RISC and miRNAs, they may instead affect miRNA expression via splicing of target molecules, regulation of protein and transcription factor activity, or genetic regulation (Hutchinson et al., 2007, Wilusz et al., 2009, Anko and Neugebauer, 2010, Malecova and Morris, 2010, Tsai et al., 2010, Saxena and Carninci, 2011, Geisler and Coller, 2013, Kornienko et al., 2013, Bergmann and Spector, 2014). Indeed, evidence suggests that MIAT is involved in the control of splicing factors and that Emx2os and the transcription factor Emx2 are part of a regulatory feedback loop (Spigoni et al., 2010, Tsuiji et al., 2011, Aprea et al., 2013, Barry et al., 2013, Ishizuka et al., 2014). Future studies need to explore the whether or not the lncRNAs of interest exert such regulatory controls over miRNAs in NSCs.

Instead of pulling down everything actively associated with Ago2, another method for this experiment would have been to use the teratogen-sensitive miRNAs

themselves as RIP targets. That would require the introduction of biotinylated oligonucleotide miRNA mimics into the cells followed by crosslinking and pull down of these tagged mimics with any interacting molecules. Indeed, this would have been a logical next step had there been solid evidence suggesting any of these lncRNAs were interacting with Ago2. Realistically, results of miRNA mimic pull downs may have been more powerful because any lncRNA amplification in the resultant RIP fractions would indicate a direct relationship between a specific miRNA and a specific lncRNA. However, as an initial assessment for potential interactions, this option seemed inappropriate.

Several pitfalls associated with miRNA mimic pull downs exist. However, for these experiments, the major concern was the potential for a high false positive rate. This often occurs in miRNA mimic pull downs because expression of the target miRNA in cells is altered resulting in concentrations that differ greatly from endogenous expression levels. Due to this effective excess of target miRNA expression in cells, associations that do not normally occur often or at all may be detected (Thomas et al., 2010, Thomson et al., 2011). Similarly, while co-immunoprecipitations always carry some risk of false positives due to target binding following cell lysis, this could be magnified in the case of miRNA mimic pull down due to the abnormal levels of transcript present; any excess miRNA mimics not loaded in RISC could be loaded after cell lysis (Riley et al., 2012). Since the goal of the RIP experiments was to assess the potential for lncRNA/miRNA interactions under normal cellular conditions and to observe whether or not ethanol and nicotine treatment changed these interactions, Ago RIP was chosen for this thesis.

Argonaute RIP was also deemed more appropriate as a major aim of the research was to expand knowledge on the lncRNAs of interest. Pull downs with miRNA mimics would have provided limited additional information about TUNA, Emx2os, or MIAT if they were not amplified in the resultant samples.

To maintain a focus on the lncRNAs, a similar technique could be employed by creating oligonucleotide mimics for some of the predicted binding sites between a lncRNA and miRNA pair. Still, this scenario would likely suffer from many of the same pitfalls faced in the miRNA mimic pull down. It would also be complicated by the lack of commercially-available, validated mimics for these binding sites. Another challenge is that while it is possible to create a mimic for a full miRNA sequence, making a similar mimic for an entire lncRNA sequence would be extremely difficult due to the size. On a related note, the feasibility of instead assessing each predicted binding site for a lncRNA/miRNA pair using mimics for these potential binding sites would be severely limited by the fact that there were up to nine predicted binding sites detected for a single miRNA and lncRNA pair in the initial RNA Hybrid analyses. That would mean a minimum of nine RIPs would need to be performed in such an experiment to assess all potential binding sites.

No evidence regarding compartmentalization of lncRNA/Ago2 complexes can be gleaned from the results of qPCR performed on the RIP-generated samples. However, taking care not to attribute too much significance to the limited and inconsistent amplification that was detected in nuclear and cytoplasmic fractions, some general localization patterns for the individual lncRNAs can be suggested. All three lncRNAs

were amplified in both the nuclear and cytoplasmic fractions. Additionally, TUNA, Emx2os, and MIAT were more highly amplified in the nuclear fraction than in the cytoplasm. Nine more wells were amplified for Emx2os in nuclear fractions while six and four more were amplified for TUNA and MIAT, respectively. Since there are no other records of cellular localization for Emx2os, no comparisons can be made to the prior findings. Therefore, this represents the first investigation of this and defines a new characteristic of the lncRNA. The general amplification pattern observed for MIAT in these experiments agrees with previous works mentioned above detailing MIAT enrichment in the nuclear compartment (Sone et al., 2007, Rapicavoli et al., 2010, Ip and Nakagawa, 2012, Ishizuka et al., 2014). The same is true for TUNA. Results of this thesis point to expression of this lncRNA in both the nucleus and the cytoplasm. However, given that the report by Lin et al. (2014) did not specify expression amounts in each compartment, it is unclear whether or not the higher amplification observed in the nuclear fraction in these experiments agrees with that previous work. It is also tempting to note that, of the three transcripts, TUNA appears to show the greatest potential for interactions with Ago2. Whereas MIAT was not amplified in the nuclear or cytoplasmic RIPs at all and amplification of Emx2os was only observed in a combined total of four wells, a total of 10 wells each were amplified for TUNA in RIP samples from each cellular compartment. Yet, given the inconsistent amplification and the inability to assess the results statistically, these “trends” in localization and amplification should be taken only as preliminary findings to inform future investigation.

Poor amplification of TUNA, Emx2os, and MIAT in the Ago2 RIP experiments warrants additional discussion. As mentioned in the Experimental Results chapter, this may point toward loss or degradation of RNA during the experimental process. Alternatively, since there were some initial issues with RNA purification following extraction from the Ago2 RIP samples, these results may be associated with the presence of contaminants in the template interfering with qPCR. For instance, it is well documented that the presence of proteins, salts, carbohydrates, DNA, residual guanidine-thiocyanate, and residual phenol can lead to qPCR inhibition (Pinto, Thapper, Sontheim, and Lindblad, 2009; Carvalhais, Delgado-Rastrollo, Melo, and Cerca, 2013; Cleanup Of Trizol Reagent-Purified Total RNA Using The Pureyield RNA Midiprep System). Indeed, A260/A280 ratios for the RIP samples obtained following TRIzol extraction in these experiments were a bit lower than the 1.8-2.0 range attributed to pure RNA (Pinto, Thapper, Sontheim, and Lindblad, 2009; Sah, Kaur, and Kaur, 2014). Attempts were made to further purify the total RNA extracts via a second TRIzol extraction and spin columns. However, this resulted in extremely low RNA yields with little change in A260/A2880 ratio. For that reason, qPCR was run with the original total RNA extracts. While amplification was inconsistent for the lncRNAs of interest, other RNA transcripts assessed as potential normalization standards amplified successfully and consistently from nuclear and cytoplasmic RIPs and supernatants. These included 18S, U6, and miR-490-3p. As will be discussed more fully in the following section, microarrays run using composite RIP samples as the template also successfully amplified 52 miRNAs from the nuclear compartment and 89 miRNAs from the cytoplasmic compartment. Therefore,

these findings do not appear to support either the RNA loss explanation or the impurity explanation.

As such, the most promising explanation for this discrepancy simply appears to be that these transcripts were not present at a high enough concentration in the qPCR templates to allow for consistent detection. After all, the initial samples underwent both a fractionation step and a pull down that yielded four new samples for each original sample. Logically, if a transcript was distributed evenly across each of the four resultant samples, one would only expect to observe 25% of the expression present in whole cell extracts. For this reason, it would be wise to increase the number of cells used to generate the initial samples intended for fractionation and RIP. Certainly, it appears that a single T-75 culture flask at 80-90% confluency may not yield a high enough concentration of TUNA, Emx2os, and MIAT to allow for successful amplification in the resultant fractioned Ago2 RIP samples. For that reason, it would be wise to increase the number of flasks per sample in future RIP experiments. Additional optimization of each step of the RIP process is also advisable.

IV.4 miRNAs and Ago2: Expression Levels and Compartmentalization

In support of the investigations into potential lncRNA/Ago2 complexation and cellular compartmentalization, miRNA microarrays were run with pooled samples of nuclear and cytoplasmic RIP fractions in the hopes of finding normalization standards for these fractions. Though not part of the initial scope of this thesis, the results of these

microarrays also provided the opportunity to explore miRNA expression in NSCs. By assessing the miRNAs amplified from both nuclear and cytoplasmic Ago2 RIP fractions, a snapshot of miRNAs actively associated with RISC in the developing cortex was generated. Although there are prior reports detailing interactions between miRNAs and Argonaute proteins, to the author's knowledge only one publication has reported such associations in the developing brain. Chi et al. (2009) performed an Ago RIP in P13 mouse neocortex followed by high throughput sequencing and bioinformatics analyses. Therefore, this represents the first report of direct, *in vitro* associations between miRNAs and RISC in the prenatal brain. It is also the first report in mouse cortical NSCs to provide an understanding of the compartmentalization patterns of these complexes. Finally, the results of the microarrays allowed for an expanded *in silico* analysis of miRNAs with predicted seed-region binding sites within the sequences of TUNA, Emx2os, and MIAT.

As mentioned briefly in the preceding section, a total of 52 miRNAs are expressed in the nuclear RIP sample and a total of 89 miRNAs are expressed in the cytoplasmic RIP sample. A subset of 33 miRNAs is amplified in both compartments. Among them are miR-140-3p, miR-21, and miR-9; three of the teratogen-sensitive miRNAs originally analyzed for binding sites with all six lncRNAs of interest. With regard to overall expression, miR-9 appears to be more actively associated with Ago2 than either miR-21 or miR-140-3p. Actually, miR-9 was the most highly expressed miRNA in the cytoplasmic RIP pooled sample.

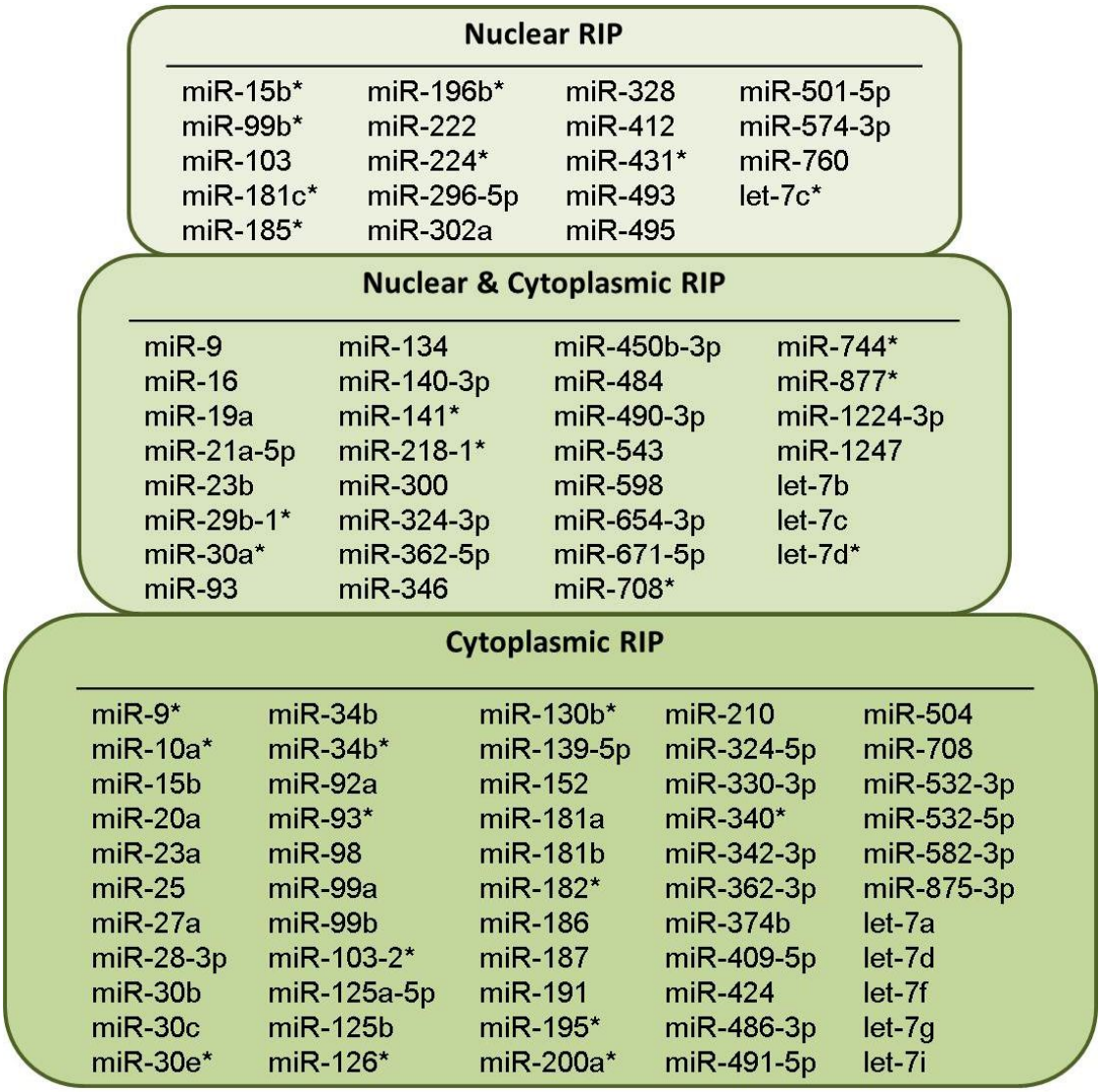

Figure 9. Amplification of EtOH/Nicotine-Sensitive miRNA in Ago2 RIP Samples

EtOH- and nicotine-sensitive miRNAs amplified from nuclear and cytoplasmic Ago2 RIP fractions via qPCR..

Attempts to learn more about the other miRNAs found to be actively associated with Ago2 in the RIP samples turned up evidence for several more ethanol- and nicotine-sensitive species. For example, Huang and Li (2009) observed dysregulation of

25 miRNAs in rat adrenal pheochromocytoma PC12 and human neuroblastoma cells following exposure to nicotine. In addition to miR-140-3p, ten of the other dysregulated miRNAs found in this study are also amplified in the nuclear or cytoplasmic RIPs. These include miR-328, miR-93, miR-181b, miR-125b, miR-25, miR-186, miR-152, miR-30c, miR-210, and miR-98. Similarly, Soares et al. (2012) reported miRNA dysregulation in zebrafish embryos exposed to two different concentrations of ethanol. Among the ethanol-sensitive transcripts observed were let-7c and miR-23a. Based on the results of this thesis, let-7c is expressed in both nuclear and cytoplasmic RIPs while miR-23a is expressed in the cytoplasmic RIP only. These studies are only two of several describing other nicotine- and ethanol-sensitive miRNAs amplified in the miRNA microarray experiments. Additionally, several more studies provide support for the ethanol sensitivity of miR-9 (Wang et al., 2009, Tal et al., 2012). Figure 9 outlines all nicotine- and ethanol-sensitive miRNAs from the primary literature that were amplified in the nuclear and cytoplasmic RIP fractions. In addition, Table 9 provides details about the publications in which these miRNAs were described as ethanol and/or nicotine sensitive.

Table 9. Primary Literature on EtOH- and Nicotine-Sensitive miRNAs

Publication	Treatment	Model System	Representative miRNA
Balaraman, Winzer-Serhan, Miranda, 2012	Ethanol/Nicotine	Mouse fetal cortical neurosphere cultures	miR-9, miR-21, miR-140-3p, miR-153, miR335
Guo, Chen, Carreon, and Qiang, 2012	Ethanol	Mouse fetal primary cortical neuron cultures	miR-504, miR-29b, miR-490, miR-92a, miR-491
Huang and Li, 2009	Nicotine	Rat PC12 cells & Human neuroblastoma SH-SY5Y cells	miR-140-3p, miR-125, miR-30c, miR-93
Maccani and Knopik, 2010	Nicotine	First trimester human placental cell lines	miR-16, miR-21, miR-146a
Ng et al., 2013	Nicotine	Human mesenchymal stem cells and periodontal ligament-derived stem cells	miR-30b, miR-218, miR-15b, miR-3198, miR-7
Sathyan, Golden, and Miranda, 2007	EtOH	Mouse fetal cortical neurosphere cultures	miR-21, miR-335, miR-153, miR-9
Soares et al., 2012	EtOH	Zebrafish embryos	let-7c, miR-153, miR-727, miR-133a
Tal et al., 2012	EtOH	Zebrafish embryos	miR-9, miR-153
Yadav et al., 2011	EtOH	Human neuroblastoma SH-SY5Y cells	miR-497, miR-302b
Yu et al., 2009	Nicotine	Head and neck squamous cell carcinoma	miR-101, miR-9, miR-221, miR-135b, miR-556-3p, miR-1259

According to *in silico* analysis with RNA Hybrid, many of the miRNAs expressed in the Ago2 RIP samples have predicted interactions with TUNA, Emx2os, and MIAT. Interestingly, most of the amplified miRNAs exhibited predicted binding sites with MIAT. Seventy-one of the miRNAs amplified in the cytoplasmic RIP fraction

and 43 of the miRNAs amplified in the nuclear RIP fraction had at least one potential binding site with this lncRNA. In comparison, TUNA and Emx2os exhibited binding sites with 55 and 54 miRNAs in the cytoplasmic RIP and 33 and 32 miRNAs in the nuclear RIP, respectively. Across both RIP fractions only miR-218-1*, miR-543, miR-21, and miR-598 exhibit no potential binding sites with the lncRNAs. However, miR-140-3p and miR-9 are amplified in each RIP fraction and have predicted interactions with TUNA and MIAT. Of the miRNAs amplified in both of the RIP fractions those with the most predicted interactions with the three lncRNAs of interest are miR-141*, let-7b, miR-29b-1*, miR-30a*, miR-877*, and miR-9.

With the information these experiments generated on miRNA/Ago2 associations, the cellular localization of these active complexes, and potential interactions between amplified miRNAs and three of the lncRNAs of interest, a variety of new research topics arise for consideration. Perhaps the most interesting of these is the chance to explore how nicotine and ethanol exposure affect these associations and their compartmentalization. Since it was not possible to investigate such effects on lncRNA/Ago2 complexes, having the opportunity to do so with the miRNA data generated in this thesis is a nice follow on.

IV.5 Conclusions and Future Research

Despite research on noncoding RNAs having increased greatly in the past decade, a variety of unexplored topics and transcripts remain. This work represents an

attempt to probe some of these unknowns and better characterize several under-investigated lncRNAs. A major outcome of these experiments is a better understanding of expression levels of the lncRNAs of interest in the developing brain. None of these RNA species were previously assessed in the mouse fetal cortical neurosphere model system employed in this thesis work. Results of the experiments detailed in the preceding chapters confirm the presence of Malat1, Cyrano, Sox2ot, TUNA, Emx2os, and MIAT in proliferative cells derived from the developing mouse cortex. In addition to gaining a better understanding of general expression patterns for the six lncRNAs of interest, these investigations provide the first description of how *in utero* exposure to ethanol and nicotine impacts expression of these transcripts. While ethanol exposure had no effect on transcripts levels in mouse fetal NSCs, several of the lncRNAs exhibited nicotine sensitivity. The nicotine-mediated downregulation observed for TUNA, Cyrano, and MIAT was unaffected by concurrent exposure to ethanol. This was in contrast to the normalizing effect simultaneous ethanol and nicotine treatment had on Malat1 and teratogen-sensitive miRNAs previously studied in this neurosphere model.

Subsequent experiments sought to assess the potential for interactions between TUNA, Emx2os, MIAT, and teratogen-sensitive miRNAs by proxy of interactions with the RISC complex protein Ago2. Attempts were also made to determine whether or not such associations and their localization within cells were disrupted by ethanol and/or nicotine exposure. However, evidence of any such interactions between TUNA, Emx2os, MIAT, and Ago2 was not observed; thus, preventing further assessments of teratogen-mediated disruption to compartmentalization and complexation. Yet, these

experiments ultimately allowed for the determination of miRNAs actively associated with RISC in cortical progenitor cells. As such, this thesis work resulted in an expanded understanding of how the six lncRNAs of interest are expressed in NSCs and how these levels are modulated in response to ethanol and nicotine exposure. It also serves to better characterize Cyrano, TUNA, and Emx2os. Additionally, this work provides new insight on RISC activity in the developing mouse cortex by generating a set of 108 miRNAs that are actively primed for RNA induced silencing of targets in NSCs.

Throughout this final chapter, details warranting future research have been raised. First, expression level dynamics of the six lncRNAs of interest should be probed in each cellular subpopulation present in NSCs. Extending this investigation to characterize transcript expression in newly generated cortical neurons would provide a complete understanding of how Malat1, Cyrano, Sox2ot, TUNA, Emx2os, and MIAT levels fluctuate throughout cortical neurogenesis. Second, assessment of lncRNA expression following exposure to ethanol and nicotine at different concentrations deserves exploration. Third, it would be meaningful to investigate the mechanisms by which nicotine downregulates Malat1, Cyrano, TUNA, and MIAT expression. A good starting point would be to explore whether or not the regulatory relationship between Malat1 and miR-9 reported in the primary literature occurs in cortical mouse NSCs; thus, explaining the partial amelioration of nicotine-mediated dysregulation of this lncRNA by concurrent ethanol exposure. A fourth area for further consideration is to continue research on potential interactions between the lncRNAs and miRNAs. This can take two paths: 1) determine whether or not the other three Argonaute proteins found in

mammals mediate post-transcriptional interactions between miRNAs and the long noncoding transcripts of interest or 2) assess possible interactions that do not occur at the post-transcriptional level, such as genetic regulation. Fifth, with so little information available on Cyrano and the fact that it is dysregulated by nicotine, this transcript should also be assessed in the Ago2 RIP samples. As with TUNA, even if no amplification is observed, it will serve to increase the limited body of knowledge on this transcript. Sixth, based on information from the miRNA microarrays, it would be interesting to investigate how nicotine and ethanol exposure might impact the loading of specific miRNAs into RISC as well as how these teratogens might affect compartmentalization of such complexes. A final topic requiring future research that was not mentioned before is the assessment of ethanol and nicotine effects on Malat1, Cyrano, Sox2ot, TUNA, Emx2os, and MIAT expression in other tissues. Special attention to expression patterns in other regions of the developing brain would afford the opportunity to determine if the actions of ethanol and nicotine on lncRNAs observed in this thesis are universal in the developing brain or specific to the cortex.

REFERENCES

Adachi J, Mizoi Y, Fukunaga T, Ogawa Y, Ueno Y, et al. (1991) Degrees of alcohol intoxication in 117 hospitalized cases. Journal of Studies on Alcohol 52:448-453.

Albertson DN, Schmidt CJ, Kapatos G, Bannon MJ (2006) Distinctive profiles of gene expression in the human nucleus accumbens associated with cocaine and heroin abuse. Neuropsychopharmacology 31:2304-2312.

Alfonso-Loeches S, Guerri C (2011) Molecular and behavioral aspects of the actions of alcohol on the adult and developing brain. Critical Reviews in Clinical Laboratory Sciences 48:19-47.

Aluru N, Deak KL, Jenny MJ, Hahn ME (2013) Developmental exposure to valproic acid alters the expression of microRNAs involved in neurodevelopment in zebrafish. Neurotoxicology and Teratology 40:46-58.

Amaral PP, Neyt C, Wilkins SJ, Askarian-Amiri ME, Sunkin SM, et al. (2009) Complex architecture and regulated expression of the Sox2ot locus during vertebrate development. RNA 15:2013-2027.

Amaral PP, Clark MB, Gascoigne DK, Dinger ME, Mattick JS (2011) lncRNAdb: a reference database for long noncoding RNAs. Nucleic Acids Research 39:D146 -151.

Andersen CL, Jensen JL, Orntoft TF (2004) Normalization of real-time quantitative reverse transcription-PCR data: a model-based variance estimation approach to identify genes suited for normalization, applied to bladder and colon cancer data sets. Cancer Research 64:5245-5250.

Anko ML, Neugebauer KM (2010) Long noncoding RNAs add another layer to pre mRNA splicing regulation. Molecular Cell 39:833-834.

Aoyama Y, Toriumi K, Mouri A, Hattori T, Ueda E, et al. (2016) Prenatal nicotine exposure impairs the proliferation of neuronal progenitors, leading to fewer glutamatergic neurons in the medial prefrontal cortex. Neuropsychopharmacology 41:578-589.

Aprea J, Prenninger S, Dori M, Ghosh T, Monasor LS, et al. (2013) Transcriptome sequencing during mouse brain development identifies long non-coding RNAs functionally involved in neurogenic commitment. EMBO Journal 32:3145-3160.

Arendt T (1994) Impairment in memory function and neurodegenerative changes in the cholinergic basal forebrain system induced by chronic intake of ethanol. Journal of Neural Transmission. Supplementum 44:173-187.

Atluri P, Fleck MW, Shen Q, Mah SJ, Stadfelt D, et al. (2001) Functional nicotinic acetylcholine receptor expression in stem and progenitor cells of the early embryonic mouse cerebral cortex. Developmental Biology 240:143-156.

Balaraman S, Winzer-Serhan UH, Miranda RC (2012) Opposing actions of ethanol and nicotine on microRNAs are mediated by nicotinic acetylcholine receptors in fetal cerebral cortical-derived neural progenitor cells. Alcoholism, Clinical and Experimental Research 36:1669-1677.

Barry G, Briggs JA, Vanichkina DP, Poth EM, Beveridge NJ, et al. (2013) The long non-coding RNA Gomafu is acutely regulated in response to neuronal activation and involved in schizophrenia-associated alternative splicing. Molecular Psychiatry 19(4):486-494.

Bavarva JH, Tae H, Settlage RE, Garner HR (2013) Characterizing the genetic basis for nicotine induced cancer development: a transcriptome sequencing study. PloS One 8(e67252):1-8.

Benowitz NL (2009) Pharmacology of nicotine: addiction, smoking-induced disease, and therapeutics. Annual Review of Pharmacology and Toxicology 49:57-71.

Benowitz NL, Jacob P, 3rd (1984) Daily intake of nicotine during cigarette smoking. Clinical Pharmacology and Therapeutics 35:499-504.

Benson DA, Cavanaugh M, Clark K, Karsch-Mizrachi I, Lipman DJ, et al. (2013) GenBank. Nucleic Acids Research 41:D36-42.

Bergmann JH, Spector DL (2014) Long non-coding RNAs: modulators of nuclear structure and function. Current Opinion in Cell Biology 26:10-18.

Bernard D, Prasanth KV, Tripathi V, Colasse S, Nakamura T, et al. (2010) A long nuclear-retained non-coding RNA regulates synaptogenesis by modulating gene expression. EMBO Journal 29:3082-3093.

Bishop KM, Goudreau G, O'Leary DD (2000) Regulation of area identity in the mammalian neocortex by Emx2 and Pax6. Science 288:344-349.

Blackshaw S, Harpavat S, Trimarchi J, Cai L, Huang H, et al. (2004) Genomic analysis of mouse retinal development. PLoS Biology 2(E247):1411-1431.

Bleich S, Sperling W, Wiltfang J, Maler JM, Kornhuber J (2003) Excitatory neurotransmission in alcoholism. Fortschritte der Neurologie-Psychiatrie 71 (Suppl 1):S36-44.

Boncinelli E, Gulisano M, Spada F, Broccoli V (1995) Emx and Otx gene expression in the developing mouse brain. Ciba Foundation Symposium 193:100-116; discussion 117-126.

Boraska V, Franklin CS, Floyd JA, Thornton LM, Huckins LM, et al. (2014) A genome wide association study of anorexia nervosa. Molecular Psychiatry 19(10):1085 -1094.

Borsani G, Tonlorenzi R, Simmler MC, Dandolo L, Arnaud D, et al. (1991) Characterization of a murine gene expressed from the inactive X chromosome. Nature 351:325-329.

Brannan CI, Dees EC, Ingram RS, Tilghman SM (1990) The product of the H19 gene may function as an RNA. Molecular and Cellular Biology 10:28-36.

Brockdorff N, Ashworth A, Kay GF, Cooper P, Smith S, et al. (1991) Conservation of position and exclusive expression of mouse Xist from the inactive X chromosome. Nature 351:329-331.

Brockdorff N, Ashworth A, Kay GF, McCabe VM, Norris DP, et al. (1992) The product of the mouse Xist gene is a 15 kb inactive X-specific transcript containing no conserved ORF and located in the nucleus. Cell 71:515-526.

Brown CJ, Hendrich BD, Rupert JL, Lafreniere RG, Xing Y, et al. (1992) The human XIST gene: analysis of a 17 kb inactive X-specific RNA that contains conserved repeats and is highly localized within the nucleus. Cell 71:527-542.

Caldwell KK, Sheema S, Paz RD, Samudio-Ruiz SL, Laughlin MH, et al. (2008) Fetal alcohol spectrum disorder-associated depression: evidence for reductions in the levels of brain-derived neurotrophic factor in a mouse model. Pharmacology, Biochemistry, and Behavior 90:614-624.

Camarillo C, Miranda RC (2008) Ethanol exposure during neurogenesis induces persistent effects on neural maturation: evidence from an ex vivo model of fetal cerebral cortical neuroepithelial progenitor maturation. Gene Expression 14:159 -171.

Carnahan MN, Veazey KJ, Muller D, Tingling JD, Miranda RC, et al. (2013) Identification of cell-specific patterns of reference gene stability in quantitative reverse-transcriptase polymerase chain reaction studies of embryonic, placental and neural stem models of prenatal ethanol exposure. Alcohol 47:109-120.

Carvalhais V, Delgado-Rastrollo M, Melo LD, Cerca N (2013) Controlled RNA contamination and degradation and its impact on qPCR gene expression in *S. epidermidis* biofilms. Journal of Microbiological Methods 95:195-200.

CDC - Fact Sheets-Alcohol Use and Health - Alcohol. Atlanta, GA: CDC.gov. N.P., 2016. Web. 24 Oct. 2015. <www.cdc.gov/alcohol/fact-sheets/alcohol-use.htm>

Center for Behavioral Health Statistics and Quality, Results From The 2013 National Survey On Drug Use And Health: Summary Of National Findings. Rockville, MD: Substance Abuse and Mental Health Services Administration, 2014.

Center for Behavioral Health Statistics and Quality, Behavioral Health Trends in the United States: Results From The 2014 National Survey On Drug Use And Health. Rockville, MD: Substance Abuse and Mental Health Services Administration, 2015.

Cents RA, Tiemeier H, Velders FP, Jaddoe VW, Hofman A, et al. (2012) Maternal smoking during pregnancy and child emotional problems: the relevance of maternal and child 5-HTTLPR genotype. American Journal of Medical Genetics. Part B, Neuropsychiatric Genetics : The Official Publication of the International Society of Psychiatric Genetics 159b:289-297.

Cesana M, Cacchiarelli D, Legnini I, Santini T, Sthandier O, et al. (2011) A long noncoding RNA controls muscle differentiation by functioning as a competing endogenous RNA. Cell 147:358-369.

Cesana M, Daley GQ (2013) Deciphering the rules of ceRNA networks. Proceedings of the National Academy of Sciences of the United States of America 110:7112-7113.

Chi SW, Zang JB, Mele A, Darnell RB (2009) Argonaute HITS-CLIP decodes microRNA-mRNA interaction maps. Nature 460:479-486.

Clark MB, Johnston RL, Inostroza-Ponta M, Fox AH, Fortini E, et al. (2012) Genome wide analysis of long noncoding RNA stability. Genome Research 22:885-898.

Cleanup of Trizol Reagent-Purified total RNA using the Pureyield RNA Midiprep System. Madison, WI: Promega, 2006. Web. 6 Oct. 2015. <www.promega.com/~/media/files/resources/promega%20notes/94/cleanup%20o%20trizol%20reagent-purified%20total%20rna%20using%20the%20pureyield%20rna%20midiprep%20system.pdf?la=en>

Clemson CM, Hutchinson JN, Sara SA, Ensminger AW, Fox AH, et al. (2009) An architectural role for a nuclear noncoding RNA: NEAT1 RNA is essential for the structure of paraspeckles. Molecular Cell 33:717-726.

de la Monte SM, Kril JJ (2014) Human alcohol-related neuropathology. Acta Neuropathologica 127:71-90.

Derrien B, Genschik P (2014) When RNA and protein degradation pathways meet. Frontiers in Plant Science 5(161):1-6.

Diederichs S (2014) The four dimensions of noncoding RNA conservation. Trends in Genetics : TIG 30:121-123.

Dinger ME, Amaral PP, Mercer TR, Pang KC, Bruce SJ, et al. (2008) Long noncoding RNAs in mouse embryonic stem cell pluripotency and differentiation. Genome Research 18:1433-1445.

Duncan JR, Randall LL, Belliveau RA, Trachtenberg FL, Randall B, et al. (2008) The effect of maternal smoking and drinking during pregnancy upon (3)H-nicotine receptor brainstem binding in infants dying of the sudden infant death syndrome: initial observations in a high risk population. Brain Pathology 18:21-31.

Duncan JR, Garland M, Stark RI, Myers MM, Fifer WP, et al. (2015) Prenatal nicotine exposure selectively affects nicotinic receptor expression in primary and associative visual cortices of the fetal baboon. brain pathology 25(2):171-181.

Dutta R, Gnanasekaran S, Suchithra S, Srilalitha V, Sujitha R, et al. (2014) A population based study on alcoholism among adult males in a rural area, Tamil Nadu, India. Journal of Clinical and Diagnostic Research 8:Jc01-03.

Dwyer JB, Broide RS, Leslie FM (2008) Nicotine and brain development. Birth Defects Research. Part C, Embryo Today: Reviews 84:30-44.

Ender C, Meister G (2010) Argonaute proteins at a glance. Journal of Cell Science 123:1819-1823.

Fagerstrom K, Furberg H (2008) A comparison of the Fagerstrom Test for nicotine dependence and smoking prevalence across countries. Addiction 103:841-845.

Fagerstrom K (2014) Nicotine: pharmacology, toxicity and therapeutic use. Journal of Smoking Cessation 9.02: 53-59.

Fan Y, Shen B, Tan M, Mu X, Qin Y, et al. (2014) TGF-beta-induced upregulation of malat1 promotes bladder cancer metastasis by associating with suz12. Clinical Cancer 20(6):1531-1541.

Fatica A, Bozzoni I (2014) Long non-coding RNAs: new players in cell differentiation and development. Nature Reviews: Genetics 15:7-21.

Fukushima T, Taki K, Ise R, Horii I, Yoshida T (2011) MicroRNAs expression in the ethylene glycol monomethyl ether-induced testicular lesion. The Journal of Toxicological Sciences 36:601-611.

Funk D, Marinelli PW, Le AD (2006) Biological processes underlying co-use of alcohol and nicotine: neuronal mechanisms, cross-tolerance, and genetic factors. Alcohol Research & Health 29:186-192.

Gagnon KT, Corey DR (2012) Argonaute and the nuclear RNAs: new pathways for RNA-mediated control of gene expression. Nucleic Acid Therapeutics 22:3-16.

Geisler S, Coller J (2013) RNA in unexpected places: long non-coding RNA functions in diverse cellular contexts. Nature Reviews: Molecular Cell Biology 14:699-712.

Global Status Report On Alcohol And Health 2014. Geneva, Switzerland: World Health Organization, 2015. Web. 04 Oct. 2015. <www.who.int/substance_abuse/publications/global_alcohol_report/en/>

Gomes AQ, Nolasco S, Soares H (2013) Non-coding RNAs: multi-tasking molecules in the cell. International Journal of Molecular Sciences 14:16010-16039.

Gottesfeld Z, Morgan B, Perez-Polo JR (1990) Prenatal alcohol exposure alters the development of sympathetic synaptic components and of nerve growth factor receptor expression selectivity in lymphoid organs. Journal of Neuroscience Research 26:308-316.

Griffiths-Jones S (2004) The microRNA Registry. Nucleic Acids Research 32:D109 -111.

Griffiths-Jones S, Grocock RJ, van Dongen S, Bateman A, Enright AJ (2006) miRBase: microRNA sequences, targets and gene nomenclature. Nucleic Acids Research 34:D140-144.

Griffiths-Jones S, Saini HK, van Dongen S, Enright AJ (2008) miRBase: tools for microRNA genomics. Nucleic Acids Research 36:D154-158.

Grimson A, Farh KK, Johnston WK, Garrett-Engele P, Lim LP, et al. (2007) MicroRNA targeting specificity in mammals: determinants beyond seed pairing. Molecular Cell 27:91-105.

Guennewig B, Cooper AA (2014) The central role of noncoding RNA in the brain. International Review of Neurobiology 116:153-194.

Guerri C (2010) New informative and prevention programs in Europe to reduce the risks associated to alcohol consumption during pregnancy and the appearance of Foetal Alcohol Spectrum Disorders. Adicciones 22:97-99.

Guffanti A, Iacono M, Pelucchi P, Kim N, Solda G, et al. (2009) A transcriptional sketch of a primary human breast cancer by 454 deep sequencing. BMC Genomics 10(163):1-17.

Guo F, Li Y, Liu Y, Wang J, Li Y, et al. (2010) Inhibition of metastasis-associated lung adenocarcinoma transcript 1 in CaSki human cervical cancer cells suppresses cell proliferation and invasion. Acta Biochimica et Biophysica Sinica 42:224-229.

Guo Y, Chen Y, Carreon S, Qiang M (2012) Chronic intermittent ethanol exposure and its removal induce a different miRNA expression pattern in primary cortical neuronal cultures. Alcoholism, Clinical and Experimental Research 36:1058-1066.

Gupta RA, Shah N, Wang KC, Kim J, Horlings HM, et al. (2010) Long non-coding RNA HOTAIR reprograms chromatin state to promote cancer metastasis. Nature 464:1071-1076.

Gurtan AM, Sharp PA (2013) The role of miRNAs in regulating gene expression networks. Journal of molecular biology 425:3582-3600.

Gutschner T, Diederichs S (2012) The hallmarks of cancer: a long non-coding RNA point of view. RNA biology 9:703-719.

Gutschner T, Hammerle M, Eissmann M, Hsu J, Kim Y, et al. (2013) The noncoding RNA MALAT1 is a critical regulator of the metastasis phenotype of lung cancer cells. Cancer Research 73:1180-1189.

Halappanavar S, Jackson P, Williams A, Jensen KA, Hougaard KS, et al. (2011) Pulmonary response to surface-coated nanotitanium dioxide particles includes induction of acute phase response genes, inflammatory cascades, and changes in microRNAs: a toxicogenomic study. Environmental and Molecular Mutagenesis 52:425-439.

Hammell CM (2008) The microRNA-argonaute complex: a platform for mRNA modulation. RNA Biology 5:123-127.

Han X, Yang F, Cao H, Liang Z (2015) Malat1 regulates serum response factor through miR-133 as a competing endogenous RNA in myogenesis. FASEB Journal 29:3054-3064.

Hansen TB, Jensen TI, Clausen BH, Bramsen JB, Finsen B, et al. (2013) Natural RNA circles function as efficient microRNA sponges. Nature 495:384-388.

Harper C (1998) The neuropathology of alcohol-specific brain damage, or does alcohol damage the brain? Journal of Neuropathology and Experimental Neurology 57:101-110.

Harper C, Matsumoto I (2005) Ethanol and brain damage. Current Opinion in Pharmacology 5:73-78.

Haycock PC (2009) Fetal alcohol spectrum disorders: the epigenetic perspective. Biology of Reproduction 81:607-617.

Haycock PC, Ramsay M (2009) Exposure of mouse embryos to ethanol during preimplantation development: effect on DNA methylation in the h19 imprinting control region. Biology of Reproduction 81:618-627.

Hou Z, Zhao W, Zhou J, Shen L, Zhan P, et al. (2014) A long noncoding RNA Sox2ot regulates lung cancer cell proliferation and is a prognostic indicator of poor survival. The International Journal of Biochemistry & Cell Biology 53:380-388.

Huang W, Li MD (2009) Nicotine modulates expression of miR-140*, which targets the 3'-untranslated region of dynamin 1 gene (Dnm1). The International Journal of Neuropsychopharmacology 12:537-546.

Hutchinson JN, Ensminger AW, Clemson CM, Lynch CR, Lawrence JB, et al. (2007) A screen for nuclear transcripts identifies two linked noncoding RNAs associated with SC35 splicing domains. BMC Genomics 8(39):1-16.

Hutvagner G, Simard MJ (2008) Argonaute proteins: key players in RNA silencing. Nature Reviews: Molecular Cell Biology 9:22-32.

Ichi S, Costa FF, Bischof JM, Nakazaki H, Shen YW, et al. (2010) Folic acid remodels chromatin on Hes1 and Neurog2 promoters during caudal neural tube development. The Journal of Biological Chemistry 285:36922-36932.

Ip JY, Nakagawa S (2012) Long non-coding RNAs in nuclear bodies. Development, Growth & Differentiation 54:44-54.

Ishii N, Ozaki K, Sato H, Mizuno H, Saito S, et al. (2006) Identification of a novel non coding RNA, MIAT, that confers risk of myocardial infarction. Journal of Human Genetics 51:1087-1099.

Ishizuka A, Hasegawa Y, Ishida K, Yanaka K, Nakagawa S (2014) Formation of nuclear bodies by the lncRNA Gomafu-associating proteins Celf3 and SF1. Genes to Cells 19:704-721.

Jalali S, Bhartiya D, Lalwani MK, Sivasubbu S, Scaria V (2013) Systematic transcriptome wide analysis of lncRNA-miRNA interactions. PloS One 8(e53823):1-9.

Jarvis MJ, Giovino GA, O'Connor RJ, Kozlowski LT, Bernert JT (2014) Variation in nicotine intake among U.S. cigarette smokers during the past 25 years: evidence from NHANES surveys. Nicotine & Tobacco 16:1620-1628.

Ji P, Diederichs S, Wang W, Boing S, Metzger R, et al. (2003) MALAT-1, a novel noncoding RNA, and thymosin beta4 predict metastasis and survival in early-stage non-small cell lung cancer. Oncogene 22:8031-8041.

Johnsson P, Lipovich L, Grander D, Morris KV (2014) Evolutionary conservation of long non-coding RNAs; sequence, structure, function. Biochimica et Biophysica Acta 1840:1063-1071.

Juan L, Wang G, Radovich M, Schneider BP, Clare SE, et al. (2013) Potential roles of in regulating long intergenic noncoding RNAs. BMC Medical Genomics 6(Suppl 1:S7):1-11.

Kandel D, Chen K, Warner LA, Kessler RC, Grant B (1997) Prevalence and demographic correlates of symptoms of last year dependence on alcohol, nicotine, marijuana and cocaine in the U.S. population. Drug and Alcohol Dependence 44:11-29.

Kedmi M, Orr-Urtreger A (2007) Expression changes in mouse brains following nicotine-induced seizures: the modulation of transcription factor networks. Physiological Genomics 30:242-252.

Kersey PJ, Staines DM, Lawson D, Kulesha E, Derwent P, et al. (2012) Ensembl Genomes: an integrative resource for genome-scale data from non-vertebrate species. Nucleic Acids Research 40:D91-97.

Kornienko AE, Guenzl PM, Barlow DP, Pauler FM (2013) Gene regulation by the act of long non-coding RNA transcription. BMC Biology 11(59):1-14.

Koshimizu TA, Fujiwara Y, Sakai N, Shibata K, Tsuchiya H (2010) Oxytocin stimulates expression of a noncoding RNA tumor marker in a human neuroblastoma cell line. Life Sciences 86:455-460.

Kozomara A, Griffiths-Jones S (2011) miRBase: integrating microRNA annotation and deep-sequencing data. Nucleic Acids Research 39:D152-157.

Kozomara A, Griffiths-Jones S (2014) miRBase: annotating high confidence microRNAs using deep sequencing data. Nucleic Acids Research 42:D68-73.

Krishnan J, Mishra RK (2014) Emerging trends of long non-coding RNAs in gene activation. The FEBS Journal 281:34-45.

Kryger R, Fan L, Wilce PA, Jaquet V (2012) MALAT-1, a non protein-coding RNA is upregulated in the cerebellum, hippocampus and brain stem of human alcoholics. Alcohol 46:629-634.

Kumamoto T, Oshio S (2013) Effect of fetal exposure to bisphenol A on brain mediated by X-chromosome inactivation. The Journal of Toxicological Sciences 38:485-494.

Kuo IY, Wu CC, Chang JM, Huang YL, Lin CH, et al. (2013) Low SOX17 expression is a prognostic factor and drives transcriptional dysregulation and esophageal cancer progression. International Journal of Cancer 135(3):563-573.

Lai MC, Yang Z, Zhou L, Zhu QQ, Xie HY, et al. (2012) Long non-coding RNA MALAT-1 overexpression predicts tumor recurrence of hepatocellular carcinoma after liver transplantation. Medical Oncology 29:1810-1816.

Laufer BI, Mantha K, Kleiber ML, Diehl EJ, Addison SM, et al. (2013) Long-lasting alterations to DNA methylation and ncRNAs could underlie the effects of fetal alcohol exposure in mice. Disease Models & Mechanisms 6:977-992.

Lee RC, Feinbaum RL, Ambros V (1993) The C. elegans heterochronic gene lin-4 encodes small RNAs with antisense complementarity to lin-14. Cell 75:843-854.

Lee H, Park JR, Yang J, Kim E, Hong SH, et al. (2014) Nicotine inhibits the proliferation by upregulation of nitric oxide and increased HDAC1 in mouse neural stem cells. In vitro Cellular & Developmental Biology: Animal 50(8):731-739.

Lema C, Cunningham MJ (2010) MicroRNAs and their implications in toxicological research. Toxicology Letters 198:100-105.

Leucci E, Patella F, Waage J, Holmstrom K, Lindow M, et al. (2013) microRNA targets the long non-coding RNA MALAT1 for degradation in the nucleus. Scientific Reports 3(2535):1-6.

Lin R, Maeda S, Liu C, Karin M, Edgington TS (2007) A large noncoding RNA is a marker for murine hepatocellular carcinomas and a spectrum of human carcinomas. Oncogene 26:851-858.

Lin N, Chang KY, Li Z, Gates K, Rana ZA, et al. (2014) An evolutionarily conserved long noncoding RNA TUNA controls pluripotency and neural lineage commitment. Molecular Cell 53:1005-1019.

Lingford-Hughes A, Watson B, Kalk N, Reid A (2010) Neuropharmacology of addiction and how it informs treatment. British Medical Bulletin 96:93-110.

Liu SP, Yang JX, Cao DY, Shen K (2013) Identification of differentially expressed long non-coding RNAs in human ovarian cancer cells with different metastatic potentials. Cancer Biology & Medicine 10:138-141.

Liu XH, Sun M, Nie FQ, Ge YB, Zhang EB, et al. (2014) Lnc RNA HOTAIR functions as a competing endogenous RNA to regulate HER2 expression by sponging miR-331-3p in gastric cancer. Molecular Cancer 13(92):1-14.

Lu H, Zhang C, Hu Y, Qin H, Gu A, et al. (2016) miRNA-200c mediates mono-butyl phthalate-disrupted steroidogenesis by targeting vimentin in Leydig tumor cells and murine adrenocortical tumor cells. Toxicology Letters 241:95-102.

Lykke-Andersen K, Gilchrist MJ, Grabarek JB, Das P, Miska E, et al. (2008) Maternal Argonaute 2 is essential for early mouse development at the maternal-zygotic transition. Molecular Biology of the Cell 19:4383-4392.

Ma L, Bajic VB, Zhang Z (2013) On the classification of long non-coding RNAs. RNA Biology 10:925-933.

Maccani MA, Knopik VS (2012) Cigarette smoke exposure-associated alterations to non-coding RNA. Frontiers in Genetics 3 (53):1-8.

Malecova B, Morris KV (2010) Transcriptional gene silencing through epigenetic changes mediated by non-coding RNAs. Current Opinion in Molecular Therapeutics 12:214-222.

Mamo S, Gal AB, Bodo S, Dinnyes A (2007) Quantitative evaluation and selection of reference genes in mouse oocytes and embryos cultured in vivo and in vitro. BMC Developmental Biology 7(14):1-12.

Mandalos N, Saridaki M, Harper JL, Kotsoni A, Yang P, et al. (2012) Application of a novel strategy of engineering conditional alleles to a single exon gene, Sox2. PloS One 7(e45768):1-9.

Markunas CA, Xu Z, Harlid S, Wade PA, Lie RT, et al. (2014) Identification of DNA Methylation Changes in Newborns Related to Maternal Smoking during Pregnancy. Environmental Health Perspectives 122(10):1147-1153.

McGinnis S, Madden TL (2004) BLAST: at the core of a powerful and diverse set of sequence analysis tools. Nucleic Acids Research 32:W20-25.

Meister G (2013) Argonaute proteins: functional insights and emerging roles. Nature Reviews: Genetics 14:447-459.

Mercer TR, Dinger ME, Sunkin SM, Mehler MF, Mattick JS (2008) Specific expression of long noncoding RNAs in the mouse brain. Proceedings of the National Academy of Sciences of the United States of America 105:716-721.

Mercer TR, Dinger ME, Mattick JS (2009) Long non-coding RNAs: insights into functions. Nature Reviews: Genetics 10:155-159.

Mercer TR, Qureshi IA, Gokhan S, Dinger ME, Li G, et al. (2010) Long noncoding RNAs in neuronal-glial fate specification and oligodendrocyte lineage maturation. BMC Neuroscience 11(14):1-15.

Michelhaugh SK, Lipovich L, Blythe J, Jia H, Kapatos G, et al. (2011) Mining Affymetrix microarray data for long non-coding RNAs: altered expression in the nucleus accumbens of heroin abusers. Journal of Neurochemistry 116:459-466.

Mick E, Biederman J, Faraone SV, Sayer J, Kleinman S (2002) Case-control study of attention-deficit hyperactivity disorder and maternal smoking, alcohol use, and drug use during pregnancy. Journal of the American Academy of Child and Adolescent Psychiatry 41:378-385.

Miller MW, Dow-Edwards DL (1988) Structural and metabolic alterations in rat cerebral cortex induced by prenatal exposure to ethanol. Brain Research 474:316-326.

microRNA Target Identification By RNA Pull Down With Biotinylated microRNA Mimics. Vedbaek, Denmark: Exiqon. Web. 11 Nov. 2015. <www.exiqon.com/ls/Documents/Scientific/RNA-pull-down-with-biotinylated-microRNA-mimics.pdf>

Miranda RC, Santillano DR, Camarillo C, Dohrman D (2008) Modeling the impact of alcohol on cortical development in a dish: strategies from mapping neural stem cell fate. Methods in Molecular Biology 447:151-168.

Mohamadkhani A (2014) Long noncoding RNAs in interaction with RNA binding proteins in hepatocellular carcinoma. Hepatitis Monthly 14(e18794):1-5.

Moran VA, Niland CN, Khalil AM (2012) Co-Immunoprecipitation of long noncoding RNAs. Methods in Molecular Biology 925:219-228.

Morita S, Horii T, Kimura M, Goto Y, Ochiya T, et al. (2007) One Argonaute family member, Eif2c2 (Ago2), is essential for development and appears not to be involved in DNA methylation. Genomics 89:687-696.

Most D, Ferguson L, Harris RA (2014) Molecular basis of alcoholism. Handbook of Clinical Neurology 125:89-111.

Naetar N, Hutter S, Dorner D, Dechat T, Korbei B, et al. (2007) LAP2alpha-binding protein LINT-25 is a novel chromatin-associated protein involved in cell cycle exit. Journal of Cell Science 120:737-747.

Nakagawa S, Ip JY, Shioi G, Tripathi V, Zong X, et al. (2012) Malat1 is not an essential component of nuclear speckles in mice. RNA 18:1487-1499.

Nan A, Zhou X, Chen L, Liu M, Zhang N, et al. (2016) A transcribed ultraconserved noncoding RNA, Uc.173, is a key molecule for the inhibition of lead-induced neuronal apoptosis. Oncotarget 7:112-124.

Ng TK, Carballosa CM, Pelaez D, Wong HK, Choy KW, et al. (2013) Nicotine alters microRNA expression and hinders human adult stem cell regenerative potential. Stem Cells and Development 22:781-790.

Noonan FC, Goodfellow PJ, Staloch LJ, Mutch DG, Simon TC (2003) Antisense transcripts at the EMX2 locus in human and mouse. Genomics 81:58-66.

Oh JH, Son MY, Choi MS, Kim S, Choi AY, et al. (2015) Integrative analysis of genes and miRNA alterations in human embryonic stem cells-derived neural cells after exposure to silver nanoparticles. Toxicology and Applied Pharmacology S0041-008X(15): 30131-30139.

Ohrt T, Muetze J, Svoboda P, Schwille P (2012) Intracellular localization and routing of miRNA and RNAi pathway components. Current Topics in Medicinal Chemistry 12:79-88.

Onoguchi M, Hirabayashi Y, Koseki H, Gotoh Y (2012) A noncoding RNA regulates the neurogenin1 gene locus during mouse neocortical development. Proceedings of the National Academy of Sciences of the United States of America 109:16939-16944.

Ouko LA, Shantikumar K, Knezovich J, Haycock P, Schnugh DJ, et al. (2009) Effect of alcohol consumption on CpG methylation in the differentially methylated regions of H19 and IG-DMR in male gametes: implications for fetal alcohol spectrum disorders. Alcoholism, Clinical and Experimental Research 33:1615-1627.

Ozgur E, Mert U, Isin M, Okutan M, Dalay N, et al. (2013) Differential expression of long non-coding RNAs during genotoxic stress-induced apoptosis in HeLa and MCF-7 cells. Clinical and Experimental Medicine 13:119-126.

Pachnis V, Belayew A, Tilghman SM (1984) Locus unlinked to alpha-fetoprotein under the control of the murine raf and Rif genes. Proceedings of the National Academy of Sciences of the United States of America 81:5523-5527.

Pachnis V, Brannan CI, Tilghman SM (1988) The structure and expression of a novel gene activated in early mouse embryogenesis. EMBO Journal 7:673-681.

Palazzo AF, Lee ES (2015) Non-coding RNA: what is functional and what is junk? Frontiers in Genetics 6(2):1-11.

Patel DJ, Ma JB, Yuan YR, Ye K, Pei Y, et al. (2006) Structural biology of RNA silencing and its functional implications. Cold Spring Harbor Symposia on Quantitative Biology 71:81-93.

Pfaffl MW, Tichopad A, Prgomet C, Neuvians TP (2004) Determination of stable housekeeping genes, differentially regulated target genes and sample integrity: BestKeeper--Excel-based tool using pair-wise correlations. Biotechnology Letters 26:509-515.

Pinto FL, Thapper A, Sontheim W, Lindblad P (2009) Analysis of current and alternative phenol based RNA extraction methodologies for cyanobacteria. BMC Molecular Biology 10(79):1-8.

Pleil KE, Lowery-Gionta EG, Crowley NA, Li C, Marcinkiewcz CA, et al. (2015) Effects of chronic ethanol exposure on neuronal function in the prefrontal cortex and extended amygdala. Neuropharmacology 99:735-749.

Pogribny IP, Tryndyak VP, Boyko A, Rodriguez-Juarez R, Beland FA, et al. (2007) Induction of microRNAome deregulation in rat liver by long-term tamoxifen exposure. Mutation Research 619:30-37.

Ponting CP, Oliver PL, Reik W (2009) Evolution and functions of long noncoding RNAs. Cell 136:629-641.

Qi Y, Zhang M, Li H, Frank JA, Dai L, et al. (2014) MicroRNA-29b regulates ethanol induced neuronal apoptosis in the developing cerebellum through SP1/RAX/PKR cascade. The Journal of Biological Chemistry 289:10201-10210.

Ramsay M (2010) Genetic and epigenetic insights into fetal alcohol spectrum disorders. Genome Medicine 2(27):1-8.

Rapicavoli NA, Poth EM, Blackshaw S (2010) The long noncoding RNA RNCR2 directs mouse retinal cell specification. BMC Developmental Biology 10(49):1-10.

Research Report Series: Tobacco/Nicotine. Rockville, MD: National Institutes on Drug Abuse, 2012. Web. 27 Mar. 2016. <www.drugabuse.gov/publications/research-reports/tobacco/letter-director>

Rehmsmeier M, Steffen P, Hochsmann M, Giegerich R (2004) Fast and effective prediction of microRNA/target duplexes. RNA 10:1507-1517.

Ren S, Liu Y, Xu W, Sun Y, Lu J, et al. (2013) Long noncoding RNA MALAT-1 is a new potential therapeutic target for castration resistant prostate cancer. The Journal of Urology 190:2278-2287.

Riley KJ, Yario TA, Steitz JA (2012) Association of Argonaute proteins and microRNAs can occur after cell lysis. RNA 18:1581-1585.

Roebuck TM, Mattson SN, Riley EP (1998) A review of the neuroanatomical findings in children with fetal alcohol syndrome or prenatal exposure to alcohol. Alcoholism, Clinical and Experimental Research 22:339-344.

Rovasio RA, Battiato NL (2002) Ethanol induces morphological and dynamic changes on *in vivo* and *in vitro* neural crest cells. Alcoholism, Clinical and Experimental Research 26:1286-1298.

Roy TS, Andrews JE, Seidler FJ, Slotkin TA (1998) Nicotine evokes cell death in embryonic rat brain during neurulation. The Journal of Pharmacology and Experimental Therapeutics 287:1136-1144.

Roza SJ, Verburg BO, Jaddoe VW, Hofman A, Mackenbach JP, et al. (2007) Effects of maternal smoking in pregnancy on prenatal brain development. The Generation R Study. The European Journal of Neuroscience 25:611-617.

Russell MA, Jarvis M, Iyer R, Feyerabend C (1980) Relation of nicotine yield of cigarettes to blood nicotine concentrations in smokers. British Medical Journal 280:972-976.

Sah SK, Kaur G, Kaur A (2014) Rapid and reliable method of high-quality RNA extraction from diverse plants. American Journal of Plant Science 05(21): 3129-3139.

Santillano DR, Kumar LS, Prock TL, Camarillo C, Tingling JD, et al. (2005) Ethanol induces cell-cycle activity and reduces stem cell diversity to alter both regenerative capacity and differentiation potential of cerebral cortical neuroepithelial precursors. BMC Neuroscience 6(59):1-17.

Sathyan P, Golden HB, Miranda RC (2007) Competing interactions between micro-RNAs determine neural progenitor survival and proliferation after ethanol exposure: evidence from an ex vivo model of the fetal cerebral cortical neuroepithelium. The Journal of Neuroscience 27:8546-8557.

Saxena A, Carninci P (2011) Long non-coding RNA modifies chromatin: epigenetic silencing by long non-coding RNAs. BioEssays 33:830-839.

Schmidt LH, Spieker T, Koschmieder S, Schaffers S, Humberg J, et al. (2011) The long noncoding MALAT-1 RNA indicates a poor prognosis in non-small cell lung cancer and induces migration and tumor growth. Journal of Thoracic Oncology 6:1984-1992.

Schneider CA, Rasband WS, Eliceiri KW (2012) NIH Image to ImageJ: 25 years of image analysis. Nature Methods 9:671-675.

Schor IE, Lleres D, Risso GJ, Pawellek A, Ule J, et al. (2012) Perturbation of chromatin structure globally affects localization and recruitment of splicing factors. PloS One 7(e48084):1-16.

Shahryari A, Rafiee MR, Fouani Y, Oliae NA, Samaei NM, et al. (2014) Two novel splice variants of SOX2OT, SOX2OT-S1, and SOX2OT-S2 are coupregulated with SOX2 and OCT4 in esophageal squamous cell carcinoma. Stem Cells 32:126-134.

Sheik Mohamed J, Gaughwin PM, Lim B, Robson P, Lipovich L (2010) Conserved long noncoding RNAs transcriptionally regulated by Oct4 and Nanog modulate pluripotency in mouse embryonic stem cells. RNA 16:324-337.

Shookhoff JM, Gallicano GI (2010) A new perspective on neural tube defects: folic acid and microRNA misexpression. Genesis 48:282-294.

Silva JM, Perez DS, Pritchett JR, Halling ML, Tang H, et al. (2010) Identification of long stress-induced non-coding transcripts that have altered expression in cancer. Genomics 95:355-362.

Silver N, Best S, Jiang J, Thein SL (2006) Selection of housekeeping genes for gene expression studies in human reticulocytes using real-time PCR. BMC Molecular Biology 7(33):1-9.

Slikker W, Jr., Xu ZA, Levin ED, Slotkin TA (2005) Mode of action: disruption of brain cell replication, second messenger, and neurotransmitter systems during development leading to cognitive dysfunction--developmental neurotoxicity of nicotine. Critical Reviews in Toxicology 35:703-711.

Slotkin TA (1998) Fetal nicotine or cocaine exposure: which one is worse? The Journal of Pharmacology and Experimental Therapeutics 285:931-945.

Slotkin TA (2004) Cholinergic systems in brain development and disruption by neurotoxicants: nicotine, environmental tobacco smoke, organophosphates. Toxicology and Applied Pharmacology 198:132-151.

Slotkin TA, MacKillop EA, Rudder CL, Ryde IT, Tate CA, et al. (2007) Permanent, sex selective effects of prenatal or adolescent nicotine exposure, separately or sequentially, in rat brain regions: indices of cholinergic and serotonergic synaptic function, cell signaling, and neural cell number and size at 6 months of age. Neuropsychopharmacology 32:1082-1097.

Soares AR, Pereira PM, Ferreira V, Reverendo M, Simoes J, et al. (2012) Ethanol exposure induces upregulation of specific microRNAs in zebrafish embryos. Toxicological Sciences 127:18-28.

Sone M, Hayashi T, Tarui H, Agata K, Takeichi M, et al. (2007) The mRNA-like noncoding RNA Gomafu constitutes a novel nuclear domain in a subset of neurons. Journal of Cell Science 120:2498-2506.

Spigoni G, Gedressi C, Mallamaci A (2010) Regulation of Emx2 expression by antisense transcripts in murine cortico-cerebral precursors. PloS One 5(e8658): 1-13.

Stouder C, Somm E, Paoloni-Giacobino A (2011) Prenatal exposure to ethanol: a specific effect on the H19 gene in sperm. Reproductive Toxicology 31:507-512.

Takahashi K, Yokota S, Tatsumi N, Fukami T, Yokoi T, et al. (2013) Cigarette smoking substantially alters plasma microRNA profiles in healthy subjects. Toxicology and Applied Pharmacology 272:154-160.

Takarada T, Nakamichi N, Kitajima S, Fukumori R, Nakazato R, et al. (2012) Promoted neuronal differentiation after activation of alpha4/beta2 nicotinic acetylcholine receptors in undifferentiated neural progenitors. PloS One 7(e46177):1-14.

Taki FA, Pan X, Zhang B (2014) Chronic nicotine exposure systemically alters microRNA expression profiles during post-embryonic stages in *Caenorhabditis elegans*. Journal of Cellular Physiology 229:79-89.

Tal TL, Franzosa JA, Tilton SC, Philbrick KA, Iwaniec UT, et al. (2012) MicroRNAs control neurobehavioral development and function in zebrafish. FASEB Journal 26:1452-1461.

Tano K, Mizuno R, Okada T, Rakwal R, Shibato J, et al. (2010) MALAT-1 enhances cell motility of lung adenocarcinoma cells by influencing the expression of motility-related genes. FEBS Letters 584:4575-4580.

Tano K, Akimitsu N (2012) Long non-coding RNAs in cancer progression. Frontiers in Genetics 3(219):1-6.

Tay Y, Rinn J, Pandolfi PP (2014) The multilayered complexity of ceRNA crosstalk and competition. Nature 505:344-352.

Thomas M, Lieberman J, Lal A (2010) Desperately seeking microRNA targets. Nature: Structural & Molecular Biology 17:1169-1174.

Thomson DW, Bracken CP, Goodall GJ (2011) Experimental strategies for microRNA target identification. Nucleic Acids Research 39:6845-6853.

Tingling JD, Bake S, Holgate R, Rawlings J, Nagsuk PP, et al. (2013) CD24 expression identifies teratogen-sensitive fetal neural stem cell subpopulations: evidence from developmental ethanol exposure and orthotopic cell transfer models. PloS One 8(e69560):1-16.

Tripathi V, Ellis JD, Shen Z, Song DY, Pan Q, et al. (2010) The nuclear-retained noncoding RNA MALAT1 regulates alternative splicing by modulating SR splicing factor phosphorylation. Molecular Cell 39:925-938.

Tsai MC, Manor O, Wan Y, Mosammaparast N, Wang JK, et al. (2010) Long noncoding RNA as modular scaffold of histone modification complexes. Science 329:689-693.

Tsai PC, Bake S, Balaraman S, Rawlings J, Holgate RR, et al. (2014) MiR-153 targets the nuclear factor-1 family and protects against teratogenic effects of ethanol exposure in fetal neural stem cells. Biology Open 3:741-758.

Tsuiji H, Yoshimoto R, Hasegawa Y, Furuno M, Yoshida M, et al. (2011) Competition between a noncoding exon and introns: Gomafu contains tandem UACUAAC repeats and associates with splicing factor-1. Genes to Cells 16:479-490.

Ulitsky I, Shkumatava A, Jan CH, Sive H, Bartel DP (2011) Conserved function of lincRNAs in vertebrate embryonic development despite rapid sequence evolution. Cell 147:1537-1550.

Ungerer M, Knezovich J, Ramsay M (2013) In utero alcohol exposure, epigenetic changes, and their consequences. Alcohol Research : Current Reviews 35:37-46.

Untergasser A, Cutcutache I, Koressaar T, Ye J, Faircloth BC, et al. (2012) Primer3-new capabilities and interfaces. Nucleic Acids Research 40(e115):1-12.

Valdiglesias V, Fernandez-Tajes J, Mendez J, Pasaro E, Laffon B (2013) The marine toxin okadaic acid induces alterations in the expression level of cancer-related genes in human neuronal cells. Ecotoxicology and Environmental Safety 92:303-311.

Vandesompele J, De Preter K, Pattyn F, Poppe B, Van Roy N, et al. (2002) Accurate normalization of real-time quantitative RT-PCR data by geometric averaging of multiple internal control genes. Genome Biology 3(7):Research0034.1-0034.11.

Vengeliene V, Bilbao A, Molander A, Spanagel R (2008) Neuropharmacology of alcohol addiction. British Journal of Pharmacology 154:299-315.

Wang G, Wang X, Wang Y, Yang JY, Li L, et al. (2008) Identification of transcription factor and microRNA binding sites in responsible to fetal alcohol syndrome. BMC Genomics 9(Suppl 1:S19):1-9.

Wang LL, Zhang Z, Li Q, Yang R, Pei X, et al. (2009) Ethanol exposure induces differential microRNA and target gene expression and teratogenic effects which can be suppressed by folic acid supplementation. Human Reproduction 24:562-579.

Wang KC, Chang HY (2011) Molecular mechanisms of long noncoding RNAs. Molecular Cell 43:904-914.

Wang Y, Xu Z, Jiang J, Xu C, Kang J, et al. (2013) Endogenous miRNA sponge lincRNA-RoR regulates Oct4, Nanog, and Sox2 in human embryonic stem cell self-renewal. Developmental Cell 25:69-80.

Wang J, Wang H, Zhang Y, Zhen N, Zhang L, et al. (2014) Mutual inhibition between YAP and SRSF1 maintains long non-coding RNA, Malat1-induced tumourigenesis in liver cancer. Cellular Signalling 26(5):1048-59.

Wang X, Li M, Wang Z, Han S, Tang X, et al. (2015) Silencing of long noncoding RNA MALAT1 by miR-101 and miR-217 inhibits proliferation, migration, and invasion of esophageal squamous cell carcinoma cells. The Journal of Biological Chemistry 290:3925-3935.

Weiss F, Porrino LJ (2002) Behavioral neurobiology of alcohol addiction: recent advances and challenges. The Journal of Neuroscience 22:3332-3337.

WHO Report On The Global Tobacco Epidemic, 2008: The MPOWER Package. Geneva, Switzerland: World Health Organization, 2008.

WHO Report On The Global Tobacco Epidemic, 2011: Warning About the Dangers of Tobacco. Geneva, Switzerland: World Health Organization, 2011.

Williams JM, Gandhi KK, Lu SE, Kumar S, Shen J, et al. (2010) Higher nicotine levels in schizophrenia compared with controls after smoking a single cigarette. Nicotine & Tobacco Research : Official Journal of the Society for Research on Nicotine and Tobacco 12:855-859.

Wilusz JE, Sunwoo H, Spector DL (2009) Long noncoding RNAs: functional surprises from the RNA world. Genes & Development 23:1494-1504.

Wu Q, Ohsako S, Ishimura R, Suzuki JS, Tohyama C (2004) Exposure of mouse preimplantation embryos to 2,3,7,8-tetrachlorodibenzo-p-dioxin (TCDD) alters the methylation status of imprinted genes H19 and Igf2. Biology of Reproduction 70:1790-1797.

Wu J, Gao M, Taylor DH (2014) Neuronal nicotinic acetylcholine receptors are important targets for alcohol reward and dependence. Acta Pharmacologica Sinica 35:311-315.

Yadav S, Pandey A, Shukla A, Talwelkar SS, Kumar A, et al. (2011) miR-497 and miR-302b regulate ethanol-induced neuronal cell death through BCL2 protein and cyclin D2. The Journal of Biological Chemistry 286:37347-37357.

Yamada K, Kano J, Tsunoda H, Yoshikawa H, Okubo C, et al. (2006) Phenotypic characterization of endometrial stromal sarcoma of the uterus. Cancer Science 97:106-112.

Yan B, Tao Z, Li XM, Zhang H, Yao J, et al. (2014) Aberrant expression of long non coding RNAs in early diabetic retinopathy. Investigative Ophthalmology & Visual Science 55(2):941-951.

Yan B, Yao J, Liu JY, Li XM, Wang XQ, et al. (2015) lncRNA-MIAT regulates microvascular dysfunction by functioning as a competing endogenous RNA. Circulation Research 116:1143-1156.

Yang F, Yi F, Han X, Du Q, Liang Z (2013) MALAT-1 interacts with hnRNP C in cell cycle regulation. FEBS Letters 587:3175-3181.

Ye J, Coulouris G, Zaretskaya I, Cutcutache I, Rozen S, et al. (2012) Primer-BLAST: a tool to design target-specific primers for polymerase chain reaction. BMC Bioinformatics 13(134): 1-11.

Yokoi T, Nakajima M (2013) microRNAs as mediators of drug toxicity. Annual Review of Pharmacology and Toxicology 53:377-400.

Yu MA, Kiang A, Wang-Rodriguez J, Rahimy E, Haas M, et al. (2012) Nicotine promotes acquisition of stem cell and epithelial-to-mesenchymal properties in head and neck squamous cell carcinoma. PloS One 7(e51967): 1-14.

Zhang B, Arun G, Mao YS, Lazar Z, Hung G, et al. (2012) The lncRNA Malat1 is dispensable for mouse development but its transcription plays a cis-regulatory role in the adult. Cell Reports 2:111-123.

Zhang Y, Yang L, Chen LL (2013) Life without A tail: New formats of long noncoding RNAs. The International Journal of Biochemistry & Cell Biology 54:338-349.

Zhao XM, Ren JJ, Du WH, Hao HS, Wang D, et al. (2012) Effect of 5-aza-2' deoxycytidine on methylation of the putative imprinted control region of H19 during the in vitro development of vitrified bovine two-cell embryos. Fertility and Sterility 98:222-227.

Zhou X, Gao Q, Wang J, Zhang X, Liu K, et al. (2014) Linc-RNA-RoR acts as a "sponge" against mediation of the differentiation of endometrial cancer stem cells by microRNA-145. Gynecologic Oncology 133:333-339.

APPENDIX A

MATERIALS AND REAGENTS

General		
Item	**Manufacturer**	**Manufacturer Catalog No.**
Maxymum Recovery Filter Tip Pipet Tips, 0.5-10 µL	Axygen Scientific	TF-300-L-R-S
Maxymum Recovery Filter Tip Pipet Tips, 100 µL	Axygen Scientific	TF-100-L-R-S
Maxymum Recovery Filter Tip Pipet Tips, 1000 µL	Axygen Scientific	TF-1000-L-R-S
PCR Tubes with Caps, 0.2 mL	VWR	20170-010
MaxyClear Microcentrifuge Tubes, 0.6 mL	Axygen Scientific	MCT-060-C-S
Superspin Microcentrifuge Tubes, 1.5 mL	VWR	20170-038
Disposable Individually Wrapped Serological Pipets, 5 mL	Falcon/Corning	357543
Disposable Individually Wrapped Serological Pipets, 5 mL	VWR	89130-896
Disposable Individually Wrapped Serological Pipets, 10 mL	Falcon/Corning	357551
Disposable Individually Wrapped Serological Pipets, 10 mL	VWR	89130-898
Disposable Individually Wrapped Serological Pipets, 25 mL	Falcon/Corning	357525
Disposable Individually Wrapped Serological Pipets, 25 mL	VWR	89130-900
Conical Centrifuge Tubes with Flat Cap, 15 mL	Falcon/Corning	352097
Conical Centrifuge Tubes with Flat Cap, 15 mL	VWR	89039-666
Conical Centrifuge Tubes with Flat Cap, 50 mL	Falcon/Corning	52098
Conical Centrifuge Tubes with Flat Cap, 50 mL	VWR	89039-658
Cryo.s Cryogenic Storage Vials, 2 mL, Yellow Cap	Greiner Bio-One	122278
Kimwipes, 4.4" x 8.4"	Kimberly-Clark	34155
Kimwipes, 11.8" x 11.8"	Kimberly-Clark	34133
Powder-free Soft Nitrile Gloves (S)	VWR	89038-268
Powder-free Soft Nitrile Gloves (M)	VWR	89038-270
Powder-free Soft Nitrile Gloves (L)	VWR	89038-272
1X DPBS, no calcium, no magnesium, no phenol red, 500 mL	Life Technologies/Invitrogen	14190-144

Item	Manufacturer	Manufacturer Catalog No.
1X DPBS, no calcium, no magnesium, no phenol red, 10 x 500 mL	Life Technologies/Invitrogen	14190-250
UltraPure Dnase/Rnase-Free Distilled Water, 500 mL	Life Technologies/Invitrogen	10977-015
UltraPure Dnase/Rnase-Free Distilled Water, 10 x 500 mL	Life Technologies/Invitrogen	10977-023
Water, Dnase- and Rnase-Free, PCR Certified, 1 L	Teknova	W3350
Parafilm M, 4" x 125"	Alcan Packaging	PM996
Ethanol, Pure, 190 Proof (95%), 1 gal	KOPTEC	Bio-Bio Stockroom

Cell Culture		
Item	**Manufacturer**	**Manufacturer Catalog No.**
Tissue Culture Flasks, 75 cm^2, 250 mL	Falcon/Corning	353135
Tissue Culture Flasks, 25 cm^2, 70 mL	Falcon/Corning	353082
AcroVac Filter Units,0.2 µm, 250 mL	Pall Life Sciences	AVFP02S
AcroVac Filter Units, 0.2 µm, 500 mL	Pall Life Sciences	AVFP02M
DMEM/F-12, HEPES, no phenol red, 500 mL	Life Technologies/Invitrogen	11039-021
DMEM/F-12, HEPES, no phenol red, 10 x 500 mL	Life Technologies/Invitrogen	11039-047
Human Fibroblast Growth Factor, Basic (bFGF), 10 x 10 µg	Corning	356061
Heparin, 250 mg	Sigma Aldrich	H4784
Insulin-Transferrin-Selenium-X, 100X, 10 mL	Life Technologies/Invitrogen	51500-056
Progesterone-Water Soluble, 100 mg	Sigma Aldrich	P7556
Human EGF Animal-Free, 1 mg	Peprotech	AF100151MG
Penicillin/Streptomycin	Life Technologies/Invitrogen	15140-122
Human LIF, 5 µg	Alomone Labs	L-200
Ethanol, 200 Proof (99.5+%), ACS Grade	Acros Organics	Bio-Bio Stockroom

cDNA and qPCR		
Item	**Manufacturer**	**Manufacturer Catalog No.**
MicroAmp Optical 384-Well Reaction Plate, 50 plates	Life Technologies/Invitrogen	4309849
MicroAmp Optical Adhesive Film, 100 covers	Life Technologies/Invitrogen	4311971

Item	Manufacturer	Manufacturer Catalog No.
RNaseZap Rnase Decontamination Solution, 6 x 250 mL	Life Technologies/Invitrogen	AM9782
qScript cDNA Synthesis Kit,100 rxn	Quanta Biosciences	95047-100
PerfeCTa SYBR Green Fastmix, 1250 rxn	Quanta Biosciences	95073-012

Western Blotting		
Item	**Manufacturer**	**Manufacturer Catalog No.**
NuPAGE Novex 4-12% Bis-Tris Protein Gels, 1.0 mm, 17 well, 10 gels	Life Technologies/Invitrogen	NP0329BOX
NE-PER Nuclear and Cytoplasmic Extraction Reagents, 15 mL kit	Pierce/Thermo Fisher Sci	78833
TBS 20X Liquid Concentrate, 4 L	EMD Millipore	8320-4L
iBlot Transfer Stack, PVDF, Regular Size, 10 sets	Life Technologies/Invitrogen	IB4010-01
20X MOPS/SDS Running Buffer, 500 mL	Teknova	M1089
BLOTTO, 5% Non-Fat Dry Milk, Immunoanalytical Grade	Rockland Immunochemicals	B501-0500
Western Lightning Plus ECL Kit	PerkinElmer	NEL103001EA
Restore Western Blot Stripping Buffer	Life Technologies/Invitrogen	21059
Goat Anti-rabbit IgG-HRP Secondary Antibody	Santa Cruz	sc-2004
Kaleidoscope Prestained Standard Protein Ladder	Bio-Rad	161-0324
Anti-Ago2/eIF2C2 Rabbit Polyclonal Antibody-ChIP Grade	Abcam	ab32381
Anti-Tubulin	Thermo Fischer Scientific	A11126

RNA Extraction		
Item	**Manufacturer**	**Manufacturer Catalog No.**
Trizol Reagent, 200 mL	Life Technologies/Invitrogen	15596-018
mirVana miRNA Isolation Kit, without phenol	Life Technologies/Invitrogen	AM1561
RNAqueous Total RNA Isolation Kit, 50 preps	Life Technologies/Invitrogen	AM1912
Isopropanol	Sigma Aldrich	190764
Chloroform	Sigma Aldrich	C7559

Immunoprecipitation		
Item	**Manufacturer**	**Manufacturer Catalog No.**
Dynabeads Protein G, 1 mL	Life Technologies/Invitrogen	10003D
Anti-Ago2/eIF2C2 Rabbit Polyclonal Antibody-ChIP Grade	Abcam	ab32381
Anti-Tubulin Mouse Monoclonal Antibody, beta III isoform	EMD Millipore	MAB1637
Tween 20	Sigma Aldrich	P9416

Crosslinking, Fractionation, Proteinase K Digestion, and Uncrosslinking		
Item	**Manufacturer**	**Manufacturer Catalog No.**
OmniPur SDS, 500 g	EMD Millipore	7910-500GM
Proteinase K from *Tritirachium album*	Sigma Aldrich	P2308
Halt Protease and Phosphatase Inhibitor Single-Use Cocktail, 100X, 24 x 100 µL	Pierce/ThermoScientific	78442
Paraformaldehyde 20% Solution, EM Grade	Electron Microscopy Sciences	15713-S
Tween 20	Sigma Aldrich	P9416
RNaseOUT Recombinant Ribonuclease Inhibitor	Life Technologies/Invitrogen	10777-019

APPENDIX B

NEW FUNCTIONAL HANDLE FOR USE AS A SELF-REPORTING CONTRAST AND DELIVERY AGENT IN NANOMEDICINE

B.1 Published Article

Herein is a peer reviewed article to which I have contributed. Though not explicitly related to the principle subject matter of this thesis, I submit the publication as representative of my efforts while a student at Texas A&M University.

B.2 Authorship and Contributions

The authorship of this manuscript (* principle investigator, $^{+}$ first author) is as follows:

University of Warwick; Rachel K O'Rielly*, Mathew P. Robin^{+}, Anne B. Mabire

Texas A&M University; Jeffery E. Raymond*, Ursula H. Winzer-Serhan, Joanne C. Damborsky and Elizabeth S. Raymond (*née* Thom).

B.3 Information Related to Copyright

Reprinted (adapted) with permission from: Robin, M.P.; Mabire, A.B.; Damborsky, J.C.; Thom, E.S.; Winzer-Serhan, U.H.; Raymond, J.E.; O'Reilly, R.K.

New Functional Handle for Use as a Self-Reporting Contrast and Delivery Agent in Nanomedicine. *J. Am. Chem. Soc.* **2013**, *135(25)*, 9518. Copyright 2013 American Chemical Society (See Figure B1).

This appendix has been formatted to fulfill the layout requirements of this thesis document with content only modified to meet this requirement.

Figure B1. Permission of reproduction letter

B.4 Abstract

The synthesis and photophysical characterization of a chromophore-bridged block copolymer system is presented. This system is based on a dithiomaleimide (DTM) functional group as a highly emissive functionality which can readily be incorporated into polymeric scaffolds. A key advantage of this new reporter group is its versatile chemistry, ease of further functionalization, and notably small size, which allows for ready incorporation without affecting or disrupting the self-assembly process critical to the formation of core−shell polymeric contrast and drug delivery agents. We demonstrate the potential of this functionality with a diblock system which has been shown to be appropriate for micellization and, when in the micellar state, does not self-quench. The block copolymer is shown to be significantly more emissive than the lone dye, with a concentration-independent emission and anisotropy profile from 1.5 mM to 0.15 μM. An emission lifetime and anisotropy decay comparison of the block copolymer to its micelle displays that time-domain fluorescence lifetime imaging (FLIM) is able to rapidly resolve differences in the supramolecular state of this block−dye−block polymer system. Furthermore, the ability to resolve these differences in the supramolecular state means that the DTM micelles are capable of self-reporting when disassembly occurs, simply by monitoring with FLIM. We demonstrate the great potential for in vitro applications that this system provides by using FLIM to observe micelle disassembly in different vascular components of rat hippocampal tissue. In total this system represents a

new class of in-chain emitter which is appropriate for application in quantitative imaging and the tracking of particle degradation/disassembly events in biological environments.

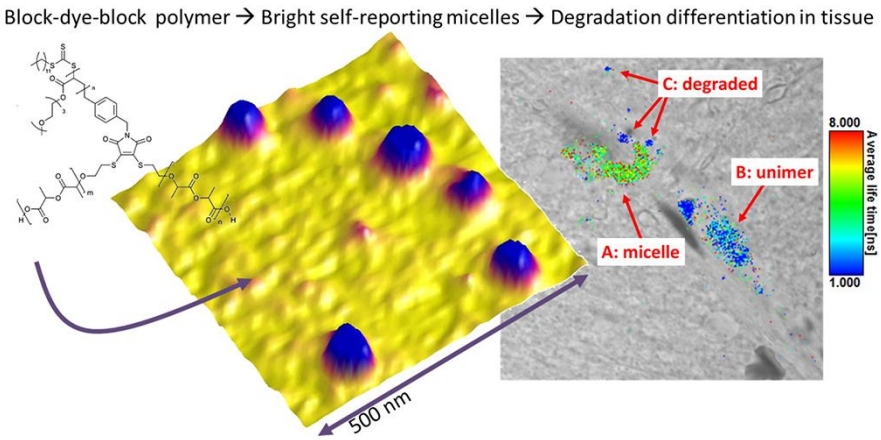

Figure B2. Abstract figure

Reprinted with permission from: Robin, M.P.; Mabire, A.B.; Damborsky, J.C.; Thom, E.S.; Winzer-Serhan, U.H.; Raymond, J.E.; O'Reilly, R.K. New Functional Handle for Use as a Self-Reporting Contrast and Delivery Agent in Nanomedicine. J. Am. Chem. Soc. 2013, 135(25), 9518. Copyright 2013 American Chemical Society.

B.5 Introduction

There has been much recent interest in the use of core−shell polymeric nanoparticles as contrast agents[1] and in-cell delivery platforms in nanomedicine.[2] Strategies for incorporating contrast and bioactive media into these systems have included tethering,[3] cross-linking,[4] and noncovalent interactions.[5] These have included processes at all three particle regions (core,[6] shell,[7] and surface[8]), but little has been done at the core−shell interface. We propose this region is of particular interest given its

environment-shielded nature compared to the surface or shell domain and distinct spatially separated location from encapsulants loaded into the interior of the scaffold. These features are key to ensuring that the emissive properties of the reporter are unaffected by local changes within the scaffold or its immediate surroundings and instead can be reliably correlated to specific whole-system events.

Common issues with conventionally labeled systems, in application, include the inability to readily observe how incubated molecules interact with the host and often no conclusive way to track particle degradation in vitro as it occurs. There is often ambiguity regarding the location of the binding molecule and its mobility in the micellar host, both for contrast agents and with pharmacological payloads. Another problem arising from encapsulation is decreased emission from loaded contrast agents, through either probe−polymer interactions or probe−probe self-quenching events.[9] Furthermore, it is known that incorporation of an emissive handle, often a large hydrophobic molecule, can lead to changes in scaffold size, stability, and even encapsulation potential due to surface modification effects.[2] Thus, new methods for the facile and nondisruptive labeling of nanostructures are required.

One solution to these particular difficulties is the formation of a reporter group system which can be readily incorporated into the polymeric scaffold and used as an emissive reporter with a nonambiguous location in the nanostructure. For this study, we have selected the core−shell interface. In our previous work, we have displayed the versatility of dithiomaleimides (DTMs) as a new highly emissive fluorophore for protein and polymer labeling.[10] In this study we have explored the incorporation of this new

system directly into a block copolymer scaffold, using the facile and well-established ring-opening polymerization (ROP)[11] and reversible addition−fragmentation chain transfer (RAFT) polymerization[12] methods. Indeed, we highlight how this functional handle can be used as a reporter group to track the micellar state and also allow for facile in situ particle tracking using its built-in bright fluorescence and self-reporting properties. This highly emissive and self-reporting system offers great potential for nanomedicine applications. Furthermore, given the ease of synthesis and ready incorporation into polymeric systems, we propose this new probe also has potential in a range of sensing and tracking applications.

B.6 Results and Discussion

B.6.1 Polymer Synthesis

Our investigations have focused on the incorporation of DTM functionality and its exploration as a bright and emissive probe in both polymers and amphiphilic polymer self-assembled structures. Positioning the DTM unit at the core−shell interface required that the hydrophobic and hydrophilic blocks of the amphiphile were polymerized from either end of this functional group by two orthogonal polymerization techniques (Figure B3). To achieve this objective, we utilized a DTM-containing dual ROP/RAFT initiator, **1**, which we have previously shown to be highly tolerant to polymerization conditions.[10] ROP using a thiourea/(−)-sparteine organocatalyst system[13] could first be initiated from

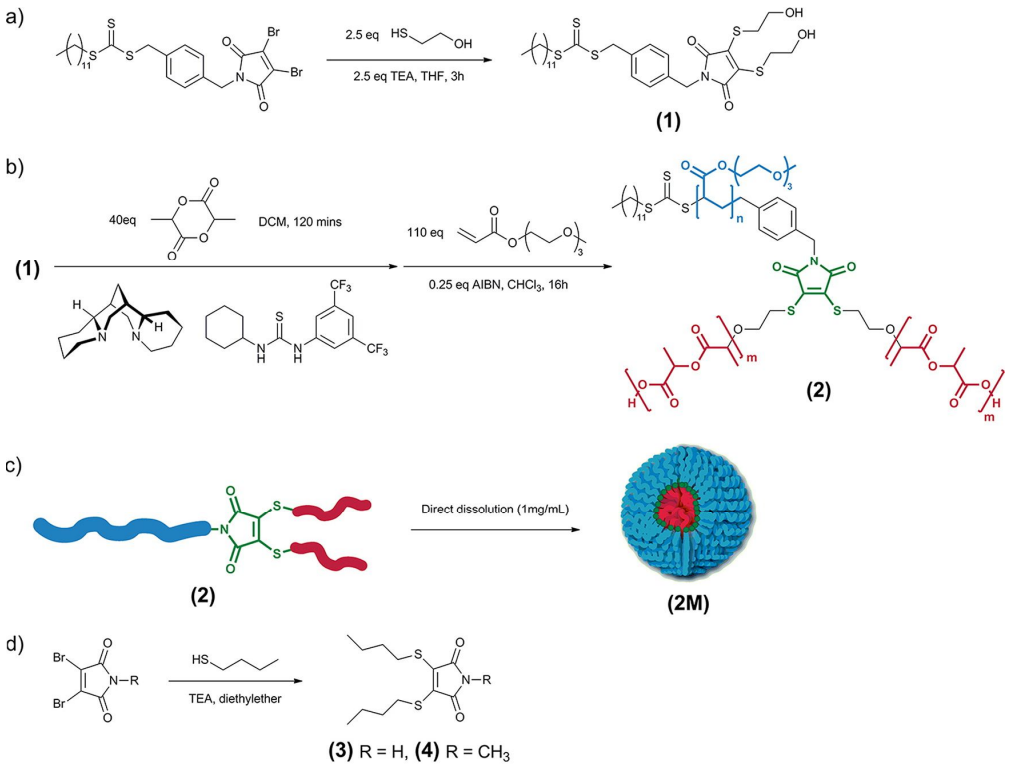

Figure B3. Synthesis of diblock copolymer, micelle formation and model dye.

*(a) Synthesis of Dual ROP/RAFT Initiator **1**, (b) Synthesis of Amphiphilic Copolymer **2** by Sequential ROP and RAFT Polymerization, (c) Self-Assembly of **2** To Give Spherical Micelles **2M**, and (d) Synthesis of Small-Molecule DTMs **3** and **4**. Reprinted with permission from: Robin, M.P.; Mabire, A.B.; Damborsky, J.C.; Thom, E.S.; Winzer-Serhan, U.H.; Raymond, J.E.; O'Reilly, R.K. New Functional Handle for Use as a Self-Reporting Contrast and Delivery Agent in Nanomedicine. J. Am. Chem. Soc. 2013, 135(25), 9518. Copyright 2013 American Chemical Society.*

the hydroxyl groups on the S substituents of the DTM unit to form the hydrophobic poly($_{D,L}$-lactide) block. Then RAFT polymerization from the trithiocarbonate attached through the N of the DTM unit afforded the hydrophilic triethylene glycol monomethyl ether acrylate (TEGA) block. The resultant Y-shaped amphiphilic block copolymer, **2**, was subsequently characterized using 1H NMR spectroscopy and size exclusion chromatography (SEC) ($M_{n,NMR}$ = 28.4 kg·mol^{-1}, $Đ_{SEC}$ = 1.22, Figures B9 and B11,

Supporting Information). To assist with the emissive characterization of the new materials, two further small-molecule DTMs were prepared, **3** and **4**. It should be noted that N-Alkylation (**4**) had only a minor effect on the fluorescence properties (see the Supporting Information), so only **3** will be discussed in detail below.

B.6.2 Micelle Assembly

Self-assembly of polymer **2** into spherical micelles was achieved using direct dissolution methods to afford a solution of micelles (**2M**) at 1 mg/mL. The number-average diameter was found to be 23 nm via dynamic light scattering (DLS), with a polydispersity index (PDI) of 0.17 (Figure B12, Supporting Information). To confirm a micellar structure, atomic force spectroscopy (AFM) was used to observe the micelles on a glass substrate. A micrograph of a typical sampling with a height profile is presented in Figure B4. While the micelles were not stable enough to be imaged on a high-energy surface (mica), which they immediately coated, the AFM images presented from solution-phase imaging on a lower energy surface (glass) were comparable in diameter to the DLS results. Furthermore, the micelles were also imaged in the dried state on a low-contrast graphene oxide support by transmission electron microscopy (TEM) without staining,[14] which confirmed an average diameter of 19.1 ± 2.1 nm (Figure B13, Supporting Information).

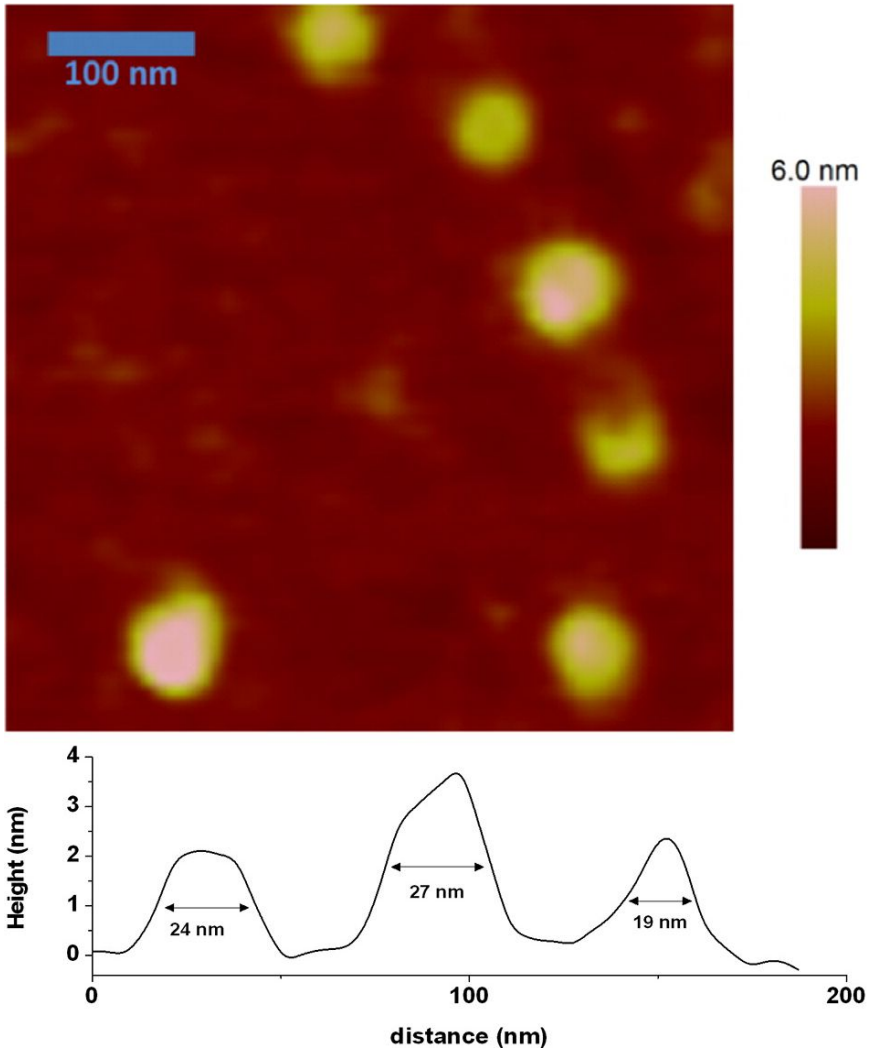

Figure B4. Atomic force microscopy of micelles **2M**.

*Solution-phase AFM micrographs of micelles **2M** imaged on a glass substrate and cross-section depicting typical micelle sizes. Reprinted with permission from: Robin, M.P.; Mabire, A.B.; Damborsky, J.C.; Thom, E.S.; Winzer-Serhan, U.H.; Raymond, J.E.; O'Reilly, R.K. New Functional Handle for Use as a Self-Reporting Contrast and Delivery Agent in Nanomedicine. J. Am. Chem. Soc. 2013, 135(25), 9518. Copyright 2013 American Chemical Society.*

B.6.3 Steady-State Fluorescence and Emission Anisotropy

Both species **2** and **3** possessed similar UV−vis and excitation spectra, with maxima near 403 nm. Steady-state emission spectra for **2** and **3** are presented in Figure B5 from 405 nm excitation. Quantum yield measurements for **2** (10 μM) in methanol resulted in a Φ_{PL} of 0.343 ± 0.004. In comparison, the ca. 30-fold less emissive **3** (12 μM) possessed a Φ_{PL} of 0.011 ± 0.002. In particular, the micelle emission efficiency compares very favorably to other common fluorescent labels, Φ_{PL} of 0.02−0.90,15 without suffering from self-quenching, despite a dye concentration in the micelle which can be calculated from DLS R_h at ca. 0.05 M. The authors attribute this increased emission to the polymeric substituents preventing both solvent/collisional quenching effects and self-quenching, though a planarization effect of the polymer substituents is not entirely ruled out. To observe the effect of concentration on emissivity, a dilution study was also performed (Figure B5). It can be seen from these integrated emission intensities that emission from **3** scales similarly to that of most self-quenching fluorophores,[9] while the micelle forming **2** possesses a relatively flat emission profile over **3** orders of magnitude of concentration.

To confirm the supramolecular state of **2** during this relatively low dependence of emission on concentration, steady state anisotropy spectroscopy was performed. While the anisotropy for emission from **3** remained flat with regard to concentration at r = 0.043 ± 0.001, the anisotropy of **2** changed significantly over the same concentration range (Figure B5). At high concentrations, anisotropy for **2** approaches that of **3**, which

the authors assign to a solvent-in-polymer character where **2**-to-**2** FRET and hopping events may lead to an overall less polarized emission.[16] In the region of uniform emissivity, anisotropy is highest (0.17), typical of a polymer micelle state where a chromophore's tumbling is reduced by incorporation into a structure where mass and volume have increased and collisional quenching with solvent is inhibited.[17] At low concentrations, anisotropy decreases to ca. 0.12 and should be taken to represent a response approaching that of the isolated polymer-in-solvent state. The fact that anisotropy does not decrease in the intermediate concentrations where a micellar state exists is particularly telling. A subtly to note is that the in-micelle local dye concentration is significantly higher than the highest sample concentration investigated (1 mM). Detailed excellently in a topical review by Olaya-Castro and Scholes,[18] increased emissivity and anisotropy from chromophore- dense assemblies are an indication of coherent energy transfer (ET) events in supramolecular structures where regular or semiordered geometries exist between substituents. However, without proximal ordering, these effects are not observed in disordered solutions, even at high concentrations. In this second case, without ordered and constrained architecture, the more conventional ET regime dominates with all of the typical effects of increased concentration (such as decreased anisotropy, quenching, and/or reabsorption) manifesting in turn. In all, both emission and anisotropy trends provide a method for distinguishing between supramolecular conditions via steady-state assessment and point to a system where timeresolved spectra may be particularly pointed in resolving changes in state.

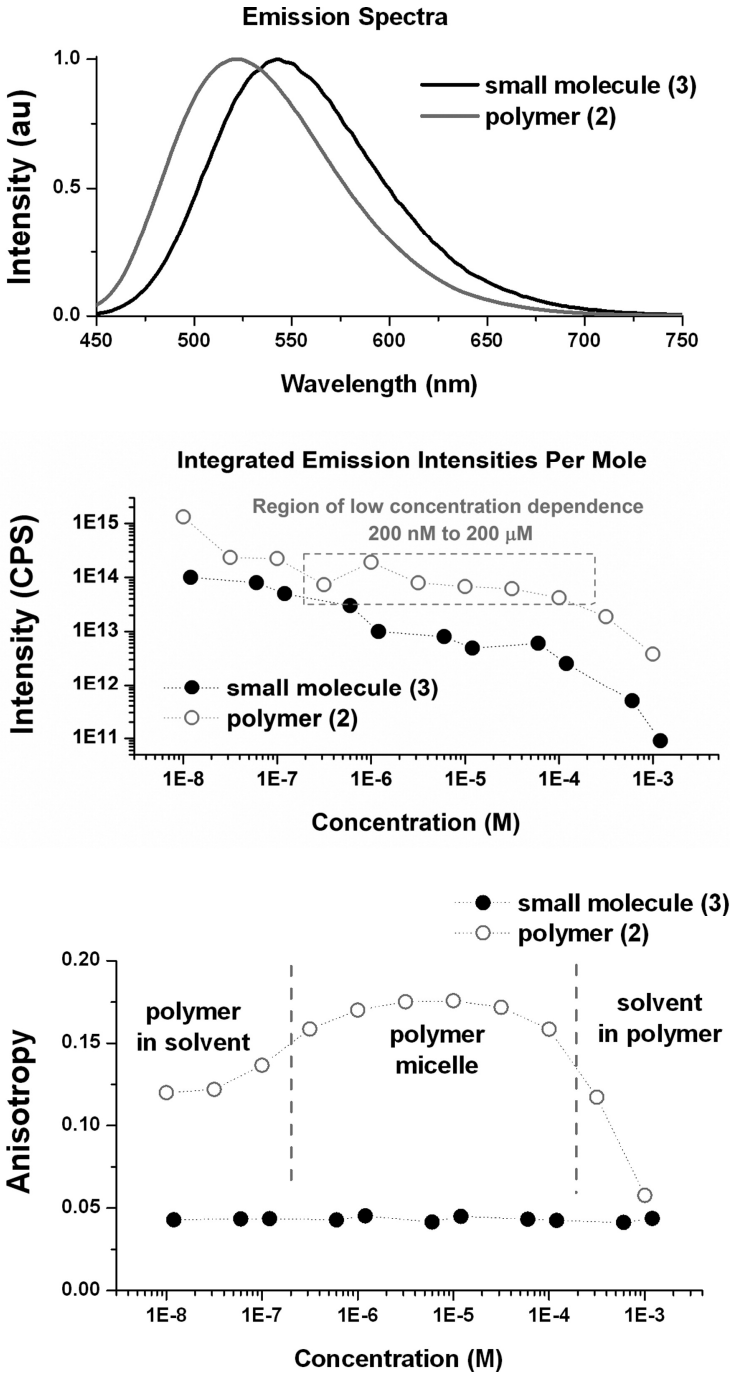

Figure B5. Steady-state emission, emissivity and emission anisotropy.

*Steady-state emission spectra, concentration-based emissivity and emission anisotropy for small-molecule **3** and polymer **2**. Reprinted with permission from: Robin, M.P.; Mabire, A.B.; Damborsky, J.C.; Thom, E.S.; Winzer-Serhan, U.H.; Raymond, J.E.; O'Reilly, R.K. New Functional Handle for Use as a Self-Reporting Contrast and Delivery Agent in Nanomedicine. J. Am. Chem. Soc. 2013, 135(25), 9518. Copyright 2013 American Chemical Society.*

B.6.4 Fluorescence Lifetime and Anisotropy Decay

To assess the viability of this polymer system for fluorescence lifetime imaging microscopy (FLIM), solution-state time-correlated single-photon counting (TCSPC) was performed to determine emission and anisotropy decay profiles. A polymer-in-solvent (**2S**, 10 nM), polymer micelle (**2M**, 1 μM) and chromophore solution (**3X**, 1.2 μM) were assessed with a pulsed 405 nm diode laser (135 ps fwhm), and resultant emission decay and anisotropy decay spectra are presented in Figure B6 with kinetic information in Table B1. All species consistently displayed three components to decay after deconvolution. The lone chromophore **3X** decays almost immediately, with two near-ultrafast lifetimes comprising the majority of decay and one longer decay of ca. 5 ns. The significance of this result can be assigned and summarized as follows: (i) the shortest decays can reasonably be assigned to nonemissive aggregation and solvent-collision effects[19] and (ii) the longer lifetime as an intrinsic relaxation event for this family of emitter, observed also as the τ_1 decay in the **2** series. However, the critical comparison, in terms of application, is of the micellar system **2M** and the solvated polymer **2S** as these differences will be key to observation of particle disassembly in vitro and in vivo. Perhaps easiest to implement is a direct comparison of average lifetimes ($\tau_{av,A}$ = 7.6−13 ns, $\tau_{av,I}$ = 15−20 ns) or emission half-lives, though any of the component extractions are sufficiently different to detect a change in state for this system.

Often even more sensitive to the local environment, anisotropy decay kinetics can also be a powerful tool for the assessment of super-, supra-, and macromolecular states.[16,19,20] For **3X**, decay from $r(0) = 0.11$ to $r(0) =$ ca. 0 occurs immediately during the first nanosecond. Comparison of **2S** and **2M** provides such contrast in anisotropy kinetic character that all components of the fitting can be used to discriminate between the micellar state and the unimer. Most telling is the apparent anisotropy recovery observed in **2S**. This rise is assigned to the emission decay of lower anisotropy states, which results in a greater expression of more anisotropic states, possibly quasi-micellar or aggregate interactions.[16,21] In conjunction with a larger steady-state anisotropy in **2M** as compared to **2S**, these spectra display that the total anisotropy decay profile and all of the extractions are viable signaling channels for monitoring a transition from a micellar state to a disassembled/degraded one.

Taking all emission and anisotropy lifetime information in total, a picture emerges relating kinetics to the polymer assembly state with final assignments as follows: (i) τ_1 in the **2** series and τ_3 in 3X are assigned to intrinsic lifetimes of the species,[20,22] (ii) longer lifetimes and higher amplitudes for τ_2 and τ_3 for **2M** are the result of better fluorophore protection when compared to **2S**,[16] (iii) fast anisotropy decay in **2M** suggests the possibility of coherent effects from localized, similarly oriented dye bridges at the core−shell interface,[19,20] and (iv) the long anisotropy decay in **2M** informs as to the time scale at which micellar tumbling occurs. For a detailed discussion of the emission lifetime and anisotropy decay for **2P** see the Supporting Information.

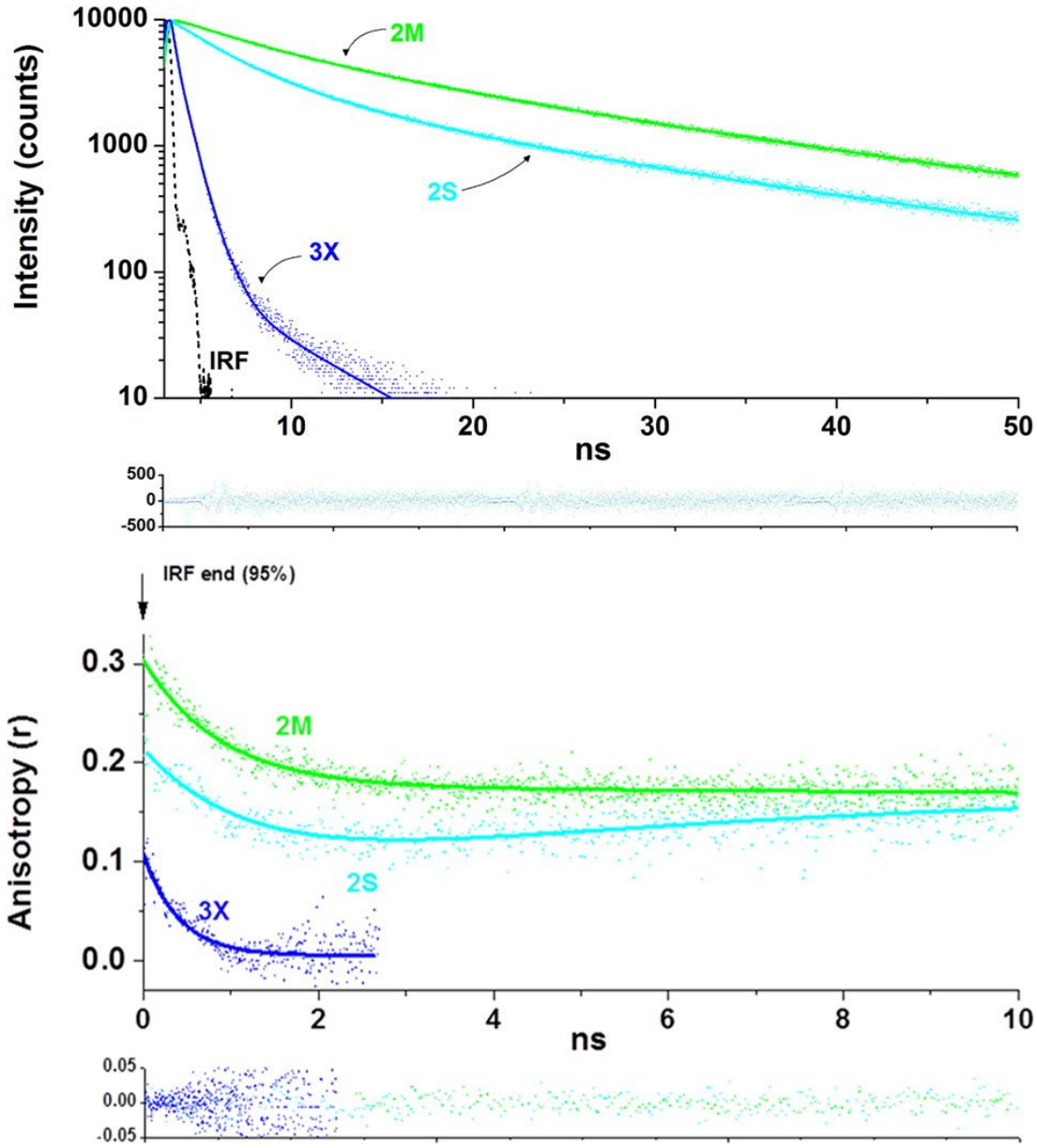

Figure B6. Fluorescence lifetimes and anisotropy decays

*Fluorescence lifetime (top) and anisotropy decay spectra (bottom) for **2M**, **2S** and **3X** with residuals. Reprinted with permission from: Robin, M.P.; Mabire, A.B.; Damborsky, J.C.; Thom, E.S.; Winzer-Serhan, U.H.; Raymond, J.E.; O'Reilly, R.K. New Functional Handle for Use as a Self-Reporting Contrast and Delivery Agent in Nanomedicine. J. Am. Chem. Soc. 2013, 135(25), 9518. Copyright 2013 American Chemical Society.*

	Lifetime								
	A_1	τ_1 (ns)	A_2	τ_2 (ns)	A_3	τ_3 (ns)	$\tau_{av,I}$ (ns)	$\tau_{av,A}$ (ns)	$t_{1/2}$ (ns)
2S	0.66	3.0 ± 0.1	0.29	9.1 ± 0.2	0.15	25.2 ± 0.2	15	7.6	6.9
2M	0.45	5.1 ± 0.2	0.48	17.5 ± 0.1	0.07	39.4 ± 0.5	20	13	10.9
3X	0.68	0.31 ± 0.01	0.31	0.77 ± 0.1	0.01	5.2 ± 0.1	1.0	0.50	3.7
	Anisotropy								
	A_1	τ_1 (ns)	A_2	τ_2 (ns)	$r(0)^a$	$r(\text{inf})^b$	$\langle r \rangle^c$		
2S	0.098	1.3 ± 0.3	0.048[rise]	0.77 ± 0.1	0.22	0.17	0.12		
2M	0.132	0.8 ± 0.1	0.034	50 ± 15	0.31	0.144	0.17		
3X	0.105	0.40 ± 0.02			0.11	0.005	0.04		
	FLIM								
	A_1	τ_1 (ns)	A_2	τ_2 (ns)	A_3	τ_3 (ns)	$\tau_{av,I}$ (ns)	$\tau_{av,A}$ (ns)	$t_{1/2}$ (ns)
2S′	0.27	2.2 ± 0.1	0.32	13.3 ± 0.2	0.41	31.0 ± 0.2	26	17	5.4
2M′	0.08	2.3 ± 0.2	0.43	16.5 ± 0.1	0.49	44 ± 1	37	29	6.9

Table B1. Emission lifetime and anisotropy kinetics for solution- and solid-state systems.

[a]r(0) is the anisotropy fit value after 95% of instrument response function (IRF), with the difference between r(0) and 0.4 taken as the ultrafast decay amplitude. [b]r(inf) is the asymptotic anisotropy reached by 95% of decay intensity. [c]⟨r⟩ is the steady-state anisotropy at emission maxima with 405 nm excitation. Reprinted with permission from: Robin, M.P.; Mabire, A.B.; Damborsky, J.C.; Thom, E.S.; Winzer-Serhan, U.H.; Raymond, J.E.; O'Reilly, R.K. New Functional Handle for Use as a Self-Reporting Contrast and Delivery Agent in Nanomedicine. J. Am. Chem. Soc. 2013, 135(25), 9518. Copyright 2013 American Chemical Society.

B.6.5 FLIM

To display the viability of self-assembled nanoparticles as self-reporting agents for nanomedicine applications, **2S** and **2M** were cast onto glass and the films (**2S′** and **2M′**) inspected by FLIM (excitation 405 nm, 450 nm long-pass collection). The resulting images and spectral data are presented in Figure B7. FLIM images indicate that both systems possess extensive micellization in the solid state. However, polymer scarcity on deposition of **2S**, and a lack of micelle structure predeposition, results in large droplet-like structures and a film background of unassembled polymer. While resolution limits preclude observation of nanoscale micelles in these systems, it is reasonable that the majority of the nanoscale micelles remain in the casting of **2M**

despite some larger (1 μm) structures. Direct lifetime tail fittings of the entire field of view are presented in Table B1. Again, observing the contrast in signals, a poignant difference in contributions to signal for the short lifetime and longer two lifetimes exist, with **2M′** possessing a significantly larger contribution to signal from longer lived states. Component lifetimes are also longer for **2M′** in all cases, as is the half-life. Comparing the average arrival time of emission and the lifetime extraction histograms (fast-FLIM signal) for both systems reveals that, even without formal emission fitting, total photon arrival times per pixel are readily capable of resolving the difference in average supramolecular state of each system (Figure B7). This ability to differentiate between states is of particular importance in terms of end-use application in translational and pharmacological studies. To summarize, the results we detail here mean that in future work with DTM functional nanoparticles it will not be necessary for expert care to be given to spectral analysis. Rather, it should be possible to readily generate biological protocols for the use of this system in a fashion that does not require extensive and overtly time consuming analysis of the decay spectra. As a demonstration of the great potential these self-reporting micellar contrast agents possess, we investigated FLIM of the particles in rat hippocampal tissue.

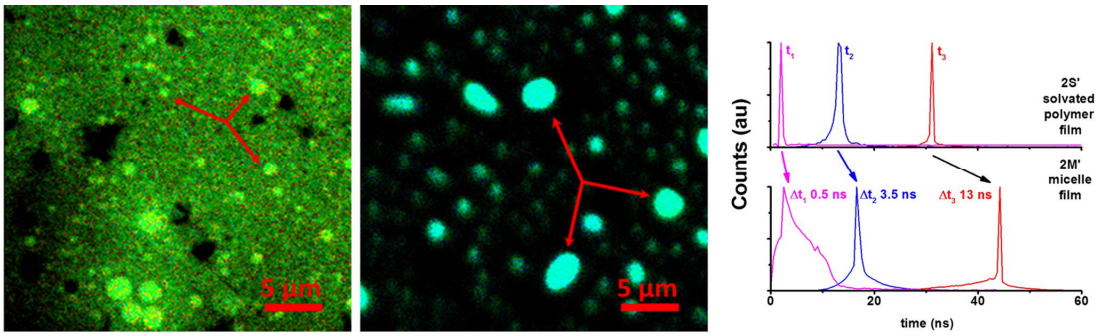

Figure B7. Fluorescence lifetime imaging microscopy of **2M′** and **2S′**.

*FLIM of cast **2M′** (left) and **2S′** (middle) with droplet-like microstructures indicated by arrows and fast-FLIM lifetime extraction histograms (right) from average photon arrival times. Reprinted with permission from: Robin, M.P.; Mabire, A.B.; Damborsky, J.C.; Thom, E.S.; Winzer-Serhan, U.H.; Raymond, J.E.; O'Reilly, R.K. New Functional Handle for Use as a Self-Reporting Contrast and Delivery Agent in Nanomedicine. J. Am. Chem. Soc. 2013, 135(25), 9518. Copyright 2013 American Chemical Society.*

B.6.6 FLIM in Rat Hippocampal Tissue

It is known that polymeric nanoparticles which have not been tailored to penetrate the blood−brain barrier tend to have a variety of interactions with vascular tissues and fluids which inhibit transport into neuronal tissue.[2,23] To provide a proof-of principle test in vitro, a cross-section of living rat hippocampal tissue was subjected to ca. 0.1 mL of 10 mg/mL polymer micelles in phosphate-buffered solution for 1 h, fixed with ethanol, and then imaged via FLIM. It was found that the micelles and degradation products could be found in three forms in the tissue, identified by their respective fluorescence lifetimes, with all states associated with vascular tissue components (Figure B8). In clotted regions (A), it could be observed that micellar (**2M**) emission was retained, while on the vascular wall (B), a shorter lifetime non-micellar polymer (**2S**)

emission can be observed. Emission from blood cells exposed to the micelles (C) displayed the shortest lifetimes. While this may be the result of heme-group emission,[24] the longer lifetime components of the emission profile do not support this theory and suggest instead that degraded polymer may have bound to the cells, resulting in emission similar to that of the solution-phase dye (**3X**). Indeed, emission decay for the C region overlays almost exactly with that of **3X**, with τ_{av} = 1.1 and 1.0 ns, respectively (Figure B19, Supporting Information).

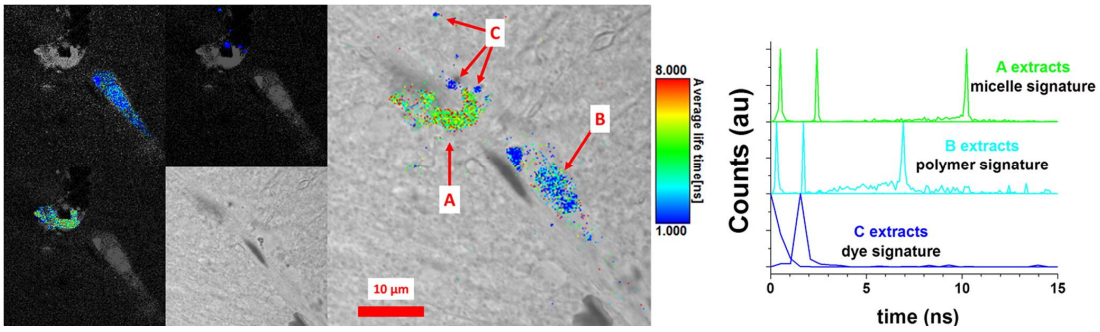

Figure B8. Fluorescence lifetime imaging microscopy *in vitro*.

*FLIM of **2M** in rat hippocampal tissue with fast-FLIM emission lifetime extractions for the clotting region (A), vascular tissue (B), and blood cells (C). Reprinted with permission from: Robin, M.P.; Mabire, A.B.; Damborsky, J.C.; Thom, E.S.; Winzer-Serhan, U.H.; Raymond, J.E.; O'Reilly, R.K. New Functional Handle for Use as a Self-Reporting Contrast and Delivery Agent in Nanomedicine. J. Am. Chem. Soc. 2013, 135(25), 9518. Copyright 2013 American Chemical Society.*

B.6.7 Application of Block-Dye-Block Emitters as Quantitative Contrast Agents and Self-Reporters

The advantage of being able to use a concentration-independent emitter as part of a diblock micelle or cross-linked nanoparticle relates to the generation of a venue for quantitative microscopic techniques in assessing nanomedicine delivery platforms. In short, without ambiguities regarding the state/location of the emitter, it becomes possible to perform cellular imaging where emission intensity is truly an indication of particle density. Similarly, for the determination of small-molecule location and loading/unloading kinetics in a polymeric nanoparticle, it becomes possible to use the FRET signal to or from the built-in chromophore to track molecules moving across the core−shell interface. Given the differences in emission anisotropy and lifetime, these materials may be ideal candidates for FLIM, anisotropy or anisotropy decay imaging of particle incorporation, and degradation both in vitro and in vivo. Lastly, noting the various gross differences in total and component decay parameters (Table B1), an array of possibilities exist for developing biological protocols that provide unambiguous answers regarding micelle location and its supramolecular state (micellar polymer, non-micellar polymer, or degraded). In practice, we suggest use of the fast-FLIM signal, fast-FLIM component signal, or a gating technique[25] for analysis when using FLIM for degradation/disassembly studies in these venues. By gating, the authors refer to selecting the temporal region where **2M** emission intensities have the highest ratio of difference for analysis. This bypasses the arduous assessment of similar fast-lifetime emission

components and allows one to look at trends in specific temporal regions where micelle emission and free polymer emission are distinctly different.

B.7 Conclusion

We present the full synthesis and photophysical properties of a polymeric emitter capable of self-assembly into bright self-reporting nanoparticles. The block–dye–block strategy presented here is the first of a new platform chemistry for generating self-reporting materials for nanomedicine through the incorporation of a specific dithiomaleimide functional group. Spectral analysis of the concentration dependence of the fluorescent polymer shows that supramolecular structuring controls emissivity, emission polarization, and lifetime. This new probe with self-reporting capabilities can be readily incorporated into polymeric nanostructures and, given its small size, can be considered non-invasive. Application methods are both shown and discussed throughout this work to best utilize the unique signaling capabilities of this system. In addition to being shown as a viable self-reporting system for solid-state applications and in-tissue studies, the "at the core–shell interface" strategy provides a route to potentially tracking explicit loading and unloading kinetics from changes in the spectral signature of the DTM from transient species crossing to and from the core.

B.8 Author Information

B.8.1 Corresponding Author

jeffery.raymond@mail.chem.tamu.edu; r.k.o-reilly@warwick.ac.uk

B.8.2 Notes

The authors declare no competing financial interest.

B.9 Acknowledgements

We graciously thank the following agencies for ongoing support of this project: Office of Naval Research (Grant N00014-10-1-0527), Welch Foundation (Grant A-0001), Engineering and Physical Sciences Research Council, European Science Foundation, and the University of Warwick Erasmus program. We also thank Karen L. Wooley (Texas A&M University) for the use of laboratory space and preparative equipment.

B.10 References

1. Xiong, H.-M.; Xu, Y.; Ren, Q.-G.; Xia, Y.-Y. J. Am. Chem. Soc. 2008, 130, 7522.
2. Elsabahy, M.; Wooley, K. L. Chem. Soc. Rev. 2012, 41, 2545.
3. Zhu, M.-Q.; Zhu, L.; Han, J. J.; Wu, W.; Hurst, J. K.; Li, A. D. Q. J. Am. Chem. Soc. 2006, 128, 4303.
4. Sun, G.; Berezin, M. Y.; Fan, J.; Lee, H.; Ma, J.; Zhang, K.; Wooley, K. L.; Achilefu, S. Nanoscale 2010, 2, 548.
5. Lee, V. Y.; Havenstrite, K.; Tjio, M.; McNeil, M.; Blau, H. M.; Miller, R. D.; Sly, J. Adv. Mater. 2011, 23, 4509.
6. Tian, Z.; Li, A. D. Q.; Hu, D. Chem. Commun. 2011, 47, 1258.
7. Xu, J.; Sun, G.; Rossin, R.; Hagooly, A.; Li, Z.; Fukukawa, K.-i.; Messmore, B. W.; Moore, D. A.; Welch, M. J.; Hawker, C. J.; Wooley, K. L. Macromolecules 2007, 40, 2971.
8. Li, Q.; Zhang, L.; Bai, L.; Zhang, Z.; Zhu, J.; Zhou, N.; Cheng, Z.; Zhu, X. Soft Matter 2011, 7, 6958.
9. Anthony, O.; Zana, R. Langmuir 1996, 12, 1967.
10. Robin, M. P.; Wilson, P.; Mabire, A. B.; Kiviaho, J. K.; Raymond, J. E.; Haddleton, D. M.; O'Reilly, R. K. J. Am. Chem. Soc. 2013, 135, 2875.
11. Dove, A. P. Chem. Commun. 2008, 2008, 6446.
12. Moad, G.; Rizzardo, E.; Thang, S. H. Aust. J. Chem. 2012, 65, 985.

13. Pratt, R. C.; Lohmeijer, B. G. G.; Long, D. A.; Lundberg, P. N. P.; Dove, A. P.; Li, H.; Wade, C. G.; Waymouth, R. M.; Hedrick, J. L. Macromolecules 2006, 39, 7863.

14. Patterson, J. P.; Sanchez, A. M.; Petzetakis, N.; Smart, T. P.; Epps, T. H., III; Portman, I.; Wilson, N. R.; O'Reilly, R. K. Soft Matter 2012, 8, 3322.

15. Langhals, H.; Karolin, J.; Johansson, L. B.-Å. J. Chem. Soc., Faraday Trans. 1998, 94, 2919.

16. Beija, M.; Fedorov, A.; Charreyre, M.-T.; Martinho, J. M. G. J. Phys. Chem. B 2010, 114, 9977.

17. Yildiz, I.; Impellizzeri, S.; Deniz, E.; McCaughan, B.; Callan, J. F.; Raymo, F. M. J. Am. Chem. Soc. 2011, 133, 871.

18. Olaya-Castro, A.; Scholes, G. D. Int. Rev. Phys. Chem. 2011, 30, 49.

19. Wang, Y.; Goodson, T., III. J. Phys. Chem. B 2007, 111, 327.

20. Varnavski, O.; Goodson, T., III; Sukhomlinova, L.; Twieg, R. J. Phys. Chem. B 2004, 108, 10484.

21. Qin, A.; Lam, J. W. Y.; Tang, B. Z. Prog. Polym. Sci. 2012, 37, 182.

22. (a) Lahankar, S. A.; West, R.; Varnavski, O.; Xie, X. B.; Goodson, T.; Sukhomlinova, L.; Twieg, R. J. Chem. Phys. 2004, 120, 337. (b) Yoo, H.; Yang, J.; Nakamura, Y.; Aratani, N.; Osuka, A.; Kim, D. J. Am. Chem. Soc. 2009, 131, 1488.

23. Mailänder, V.; Landfester, K. Biomacromolecules 2009, 10, 2379.

24. Chaudhuri, S.; Chakraborty, S.; Sengupta, P. K. Biophys. Chem. 2011, 154, 26.

25. Huang, K. W.; Marti, A. A. Anal. Chem. 2012, 84, 8075.

B.11 Supporting Information for New Functional Handle for Use as a Self-reporting Contrast and Delivery Agent in Nanomedicine

B.11.1 Experimental

B.11.1.1 Materials and Apparatus

Chemicals were used as received from Aldrich, Fluka and Acros. Dry solvents were obtained by passing over a column of activated alumina using an Innovative technologies solvent purification system. ROP reagents were purified according to literature procedures.1 TEGA was synthesized as previously reported and stored below 4 °C.[2]

^{1}H and ^{13}C NMR spectra were recorded on a Bruker DPX-400 spectrometer in $CDCl_3$. Chemical shifts are given in ppm downfield from the internal standard tetramethylsilane. Size exclusion chromatography (SEC) measurements were conducted using a Varian 390-LC-Multi detector suite fitted with differential refractive index (DRI), light scattering (LS) and photodiode array (PDA) detectors equipped with a guard column (Varian Polymer Laboratories PLGel 5 μm, 50×7.5 mm) and two mixed D columns (Varian Polymer Laboratories PLGel 5 μm, 300×7.5 mm). The mobile phase was tetrahydrofuran with 2% triethylamine eluent at a flow rate of 1.0 $ml \cdot min^{-1}$ and data

was analyzed using Cirrus v3.3 with calibration curves produced using Varian Polymer laboratories Easi-Vials linear poly(styrene) standards (162-2.4×105 $g \cdot mol^{-1}$). Dynamic light scattering (DLS) was conducted using a Malvern Zetasizer NanoS instrument operating at 25 °C with a 4 mW He-Ne 633 nm laser module and a detection angle of 173°, with data analysed using Malvern DTS 5.02 software. Transmission electron microscopy (TEM) imaging was performed on a Jeol 2011 200 kV LaB_6 instrument fitted with a Gatan UltraScan™ 1000 camera. Samples were prepared according to literature procedure.[3] UV-Vis spectra were determined with the use of Shimadzu UV-2550 spectrophotometer. All steady state emission, excitation and anisotropy spectra were obtained with a Horiba FluoroMax4 with automatic polarizers. Quantum yield calculations were performed against a tris(2-2'-pispyridyl)dichlororuthenium(II) hexahydrate standard,[4] (8 μL in 0.2 μm filtered deionized water) following the IUPAC standard method.[5] Time correlated single photon counting was employed to obtain all fluorescence lifetime spectra. This was done with a Fluorotime 100 fluorometer and 405 nm solid state ps diode laser source (PicoQuant) in matched quartz 0.7 mL cells (Starna Cell). Instrument response functions (IRF) were determined from scatter signal solution of Ludox HS-40 colloidal silica (0.01% particles in water wt/wt). The phosphate buffered saline was 1X 0.0067 M PO_4 without calcium or magnesium while methanol was anhydrous Atomic force microscopy was performed using a Multimode 8 system (Bruker) with a SA Fluid+ probe (k 0.7 N/ 150 kHz, Bruker). Fluorescence lifetime imaging was performed using a FLIM LSM upgrade kit for the FV1000 (PicoQuant) mounted on a FV1000 (Olympus) confocal microscope on a IX-81 inverted base

(Olympus). A PlanApo N 60x oil lens (NA 1.42, Olympus) was used for all imaging. The FV1000 system was driven with the FV10-ASW v3.1a software platform (Olympus) with scan rates of 4 us/pixel at 256 by 256 pixels. FLIM images and spectra were collected using bins of 16 ps with a 405 nm (LDH-P-C-405B, PicoQuant) driven at 2.5 MHz. FWHM for the 405 nm laser head was 59 ps and maximum power was 0.21 mW (attenuated by variable neutral density filters to prevent count pile up and maintain counting rates below 1% bin occupancy). Steady-state spectra were analyzed in FluoreEssence (Horiba) and in Origin 8.6 Pro (Origin Labs). TCSPC analysis was performed on Fluorofit (PicoQuant) software and confirmed by tail-fitting in Origin 8.6 Pro. AFM images were assessed with Nanoscope Analysis (Bruker). SymphoTime 64 (Picoquant) software was used for collection and analysis of FLIM images and spectra, with spectra confirmed by tail-fitting in Origin 8.6 Pro. All IRF deconvolved exponential fits were performed with the number of exponents selected for completeness of fit as determined by boot-strap chi-squared analysis in Fluorofit, typically three.

B.11.1.2 Animal Tissue Studies

Fresh 300 μm thick adult rat hippocampi slices maintained in artificial cerebrospinal fluid, as outlined in detail elsewhere,[6] were incubated with 0.1 mL of a 10 μM (PBS, Hyclone, Thermo Scientific) solution of **2** immediately after dissection. The rat used was not killed for the purposes of this experiment and all tissues used were excess from an unrelated study. In brief, an adult female Sprague-Dawley rat was

decapitated under isoflurane anesthesia, and its brain was quickly removed and submerged in an ice-cold cutting solution containing (in mM) 0.3 Kynurenic acid, 120 NaCl, 11 D-Glucose, 26 $NaHCO_3$, 6 $MgCl_2$, 3 KCl, 0.5 $CaCl_2$, and 5 HEPES. While still in the cutting solution, 300 μM coronal slices were taken through brain using a Vibratome 3000 Sectioning System. The hippocampi were dissected from the slices, and transferred to artificial cerebrospinal fluid containing (in mM) 124 NaCl, 3 KCl, 1.5 $MgSO_47H_2O$, 1.2 NaH_2PO_4, 2.4 $CaCl_2$, 26 $NaHCO_3$, and 10 D-Glucose bubbled with 95%O_2 /5%CO_2. The solution of micellar **2** was directly applied to the surface of the slices and allowed to incubate for 1 hour, then fixed with ethanol and mounted before imaging.

B.11.1.3 Synthetic Protocols

Compounds **1**, **3**, and poly(D,L-lactide) were prepared as previously reported.[7]

B.11.1.3.1 3μ-[poly(triethyleneglycol monomethyl ether methacrylate)]-b-[poly(D,L-lactide)]2 Star Block Copolymer (2)

A solution of poly(D,L-lactide) (25 mg, 3.71 μmol), TEGA (80.0 μL, 0.408 mmol), and AIBN (0.152 mg, 0.926 μmol) in CHCl3 (240 μL) was added to a polymerization ampoule. The solution was degassed by three freeze-pump-thaw cycles and sealed under N_2. The reaction was stirred at 60°C for 16 hours to a monomer

conversion of 95 %, at which point the reaction was quenched by rapid cooling. The solvent was removed *in vacuo*, and the residue was purified by dialysis (MWCO 6-8000 Da) against distilled water. The product was obtained as a fluorescent yellow waxy solid by lyophilization. $M_{n,NMR}$ = 28.4 kg·mol-1, $M_{n,SEC}$ = 20.1 kg·mol-1, $Đ_{SEC}$ = 1.22. ^{1}H NMR (400 MHz, $CDCl_3$) δ 5.25-5.11 (2H PLA, m, $OCH(CH_3)CO_2$), 4.30-4.04 (2H PTEGA, br, $CO_2CH_2CH_2$), 3.72-3.52 (10H PTEGA, br m, $CO_2CH_2CH_2O[CH_2CH_2O]_2$), 3.39-3.35 (3H PTEGA, br, $[CH_2CH_2O]_3CH_3$), 2.48-2.20 (1H PTEGA, br, $CH(CO_2)CH_2$), 1.53-1.33 (2H PTEGA, br, $CH(CO_2)CH_2$) and (6H PLA, m, $OCH(CH_3)CO_2$); FTIR (neat) νmax / cm-13511 (alcohol), 1732 (C=O ester of PLA and PTEGA), 1453 (aromatic); Fluorescence ($CHCl_3$) λem = 520 nm, λex = 410 and 270 nm

B.11.1.3.2 3,4-bis(butylsulfanyl)-1-methyl-2,5-dihydro-1H-pyrrole-2,5-dione (4)

2,3-Dibromo-N-methylmaleimide (0.956 g, 3.56 mmol) was dissolved in diethyl ether (40 mL). To the solution was added dropwise triethylamine (0.756 g, 7.47 mmol) and butanethiol (0.674 g, 7.47 mmol), whereby an immediate yellow colour was observed and a white precipitate. Upon complete addition, the solution was stirred at room temperature for 24 hours. The solution was filtered and concentrated in vacuo and the crude mixture purified by column chromatography (SiO_2, petroleum ether: ethyl acetate = 97:3) to yield the product as a yellow oil (0.35 g, 34 %). R_f = 0.21. ^{1}H NMR (400 MHz, $CDCl_3$) δ 3.28 (4H, t, J = 7.5 Hz, SCH_2), 3.01 (3H s, NCH_3), 1.63 (4H quin, J = 7.5 Hz, SCH_2CH_2), 1.45 (4H, sex, J = 7.5 Hz, CH_3CH_2), 0.93, (3H, t, J = 7.5 Hz, CH_3);

^{13}C NMR (100 MHz, $CDCl_3$) δ 166.8(C=O), 135.9 (C=C), 32.5 (SCH_2CH_2), 31.6 (SCH_2), 24.4 (NCH_3), 21.7 (CH_3CH_2), 13.6 (CH_3); FTIR (neat) ν_{max} / cm^{-1} 1768 and 1697 (C=O of maleimide); HR-MS (MaXis) m/z found 310.0903, calc. 310.0906 ([M+Na]+, 100 %).

B.11.2 Characterization

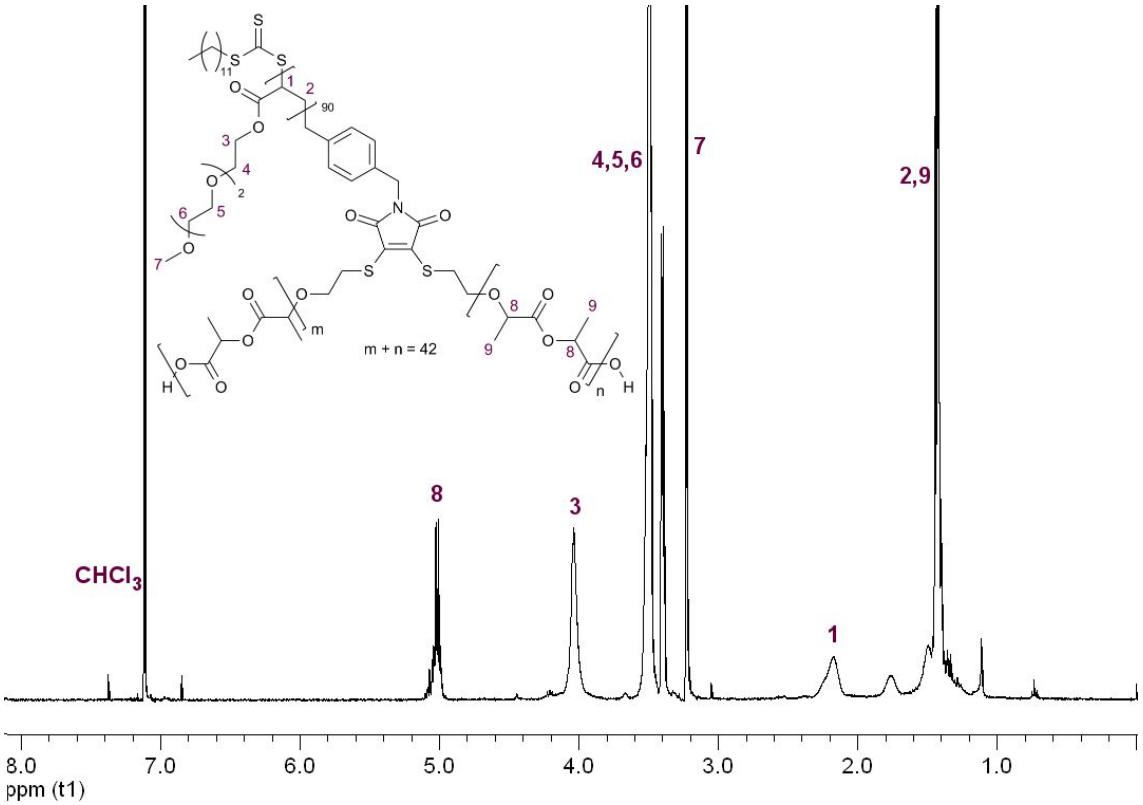

Figure B9. ^{1}H NMR (400 MHz, $CDCl_3$) spectrum of **2**.

Reprinted with permission from: Robin, M.P.; Mabire, A.B.; Damborsky, J.C.; Thom, E.S.; Winzer-Serhan, U.H.; Raymond, J.E.; O'Reilly, R.K. New Functional Handle for Use as a Self-Reporting Contrast and Delivery Agent in Nanomedicine. J. Am. Chem. Soc. 2013, 135(25), 9518. Copyright 2013 American Chemical Society.

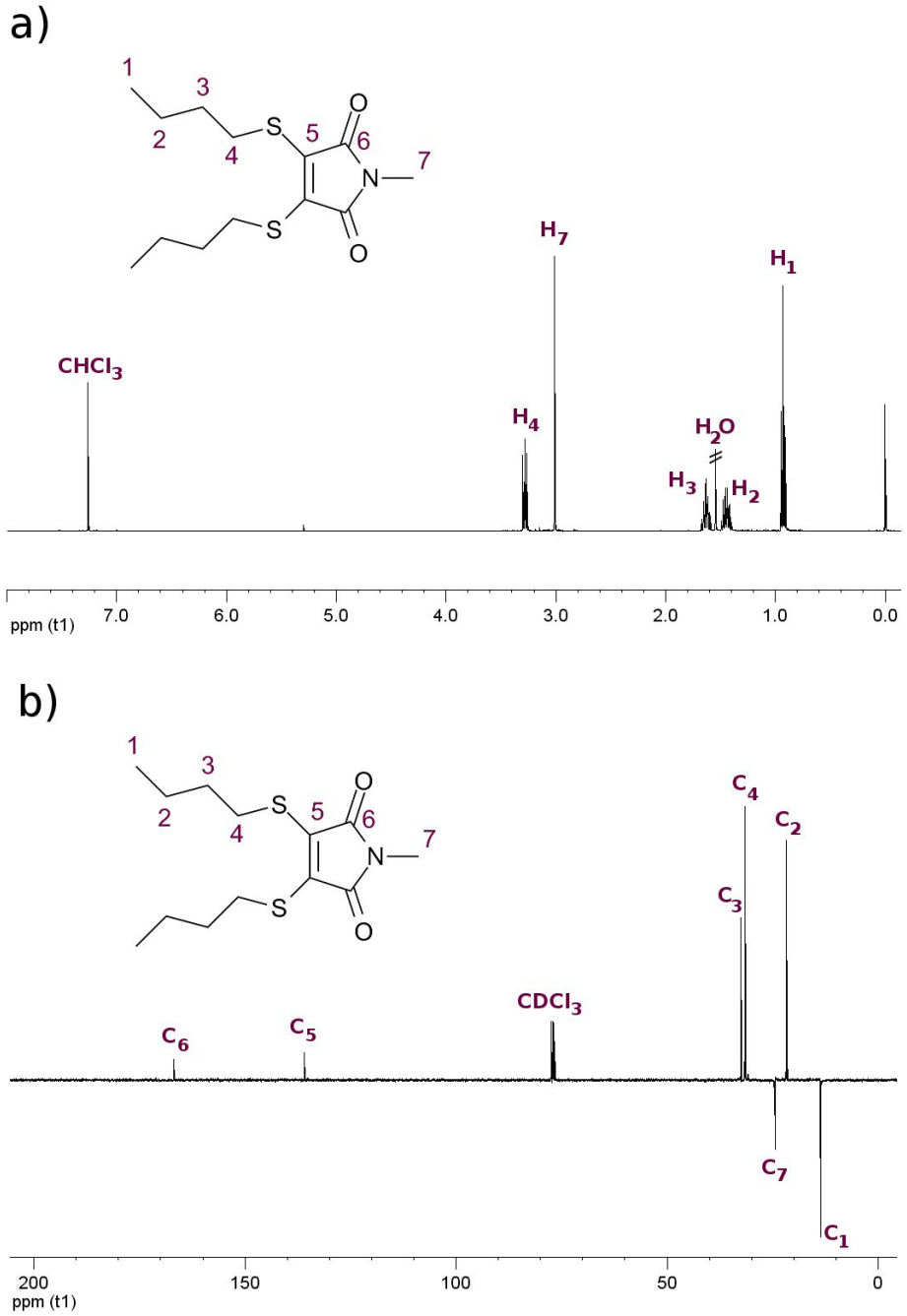

Figure B10. a) ^{1}H NMR (400 MHz, $CDCl_3$) spectrum and b) ^{13}C NMR (100 MHz, $CDCl_3$) spectrum of **4**.

Reprinted with permission from: Robin, M.P.; Mabire, A.B.; Damborsky, J.C.; Thom, E.S.; Winzer-Serhan, U.H.; Raymond, J.E.; O'Reilly, R.K. New Functional Handle for Use as a Self-Reporting Contrast and Delivery Agent in Nanomedicine. J. Am. Chem. Soc. 2013, 135(25), 9518. Copyright 2013 American Chemical Society.

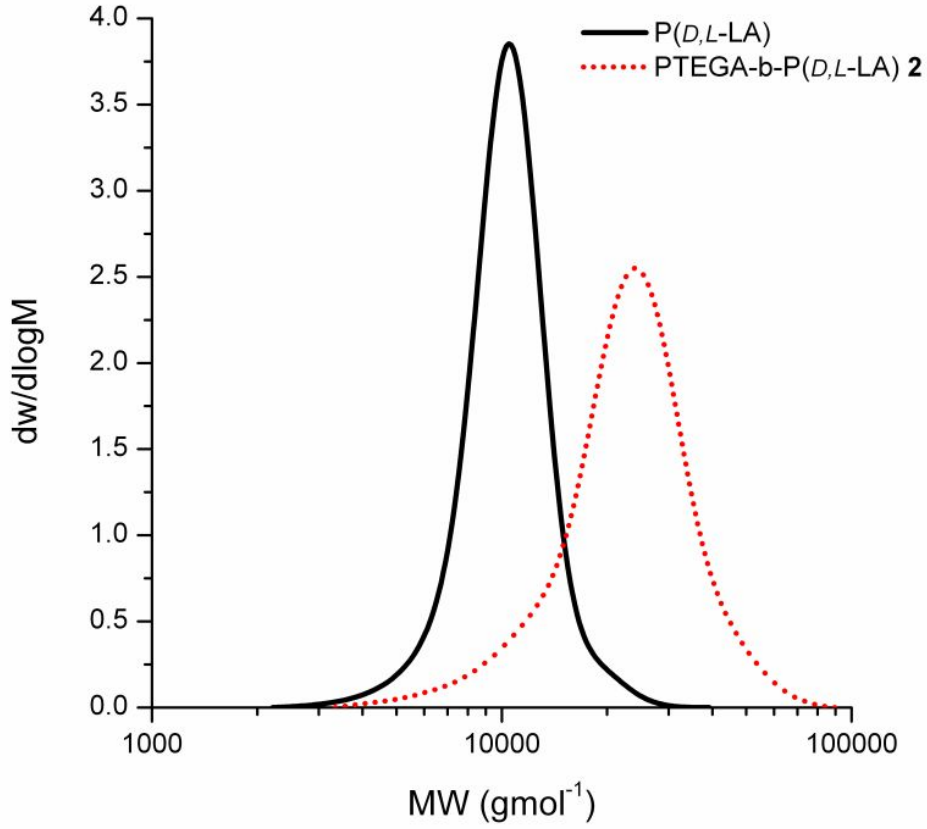

Figure B11. Molecular weight distributions obtained by SEC, with a polystyrene calibration and THF as the eluent for poly(*D,L*-lactide) and poly(TEGA)-*b*-poly(*D,L*-lactide), **2**.

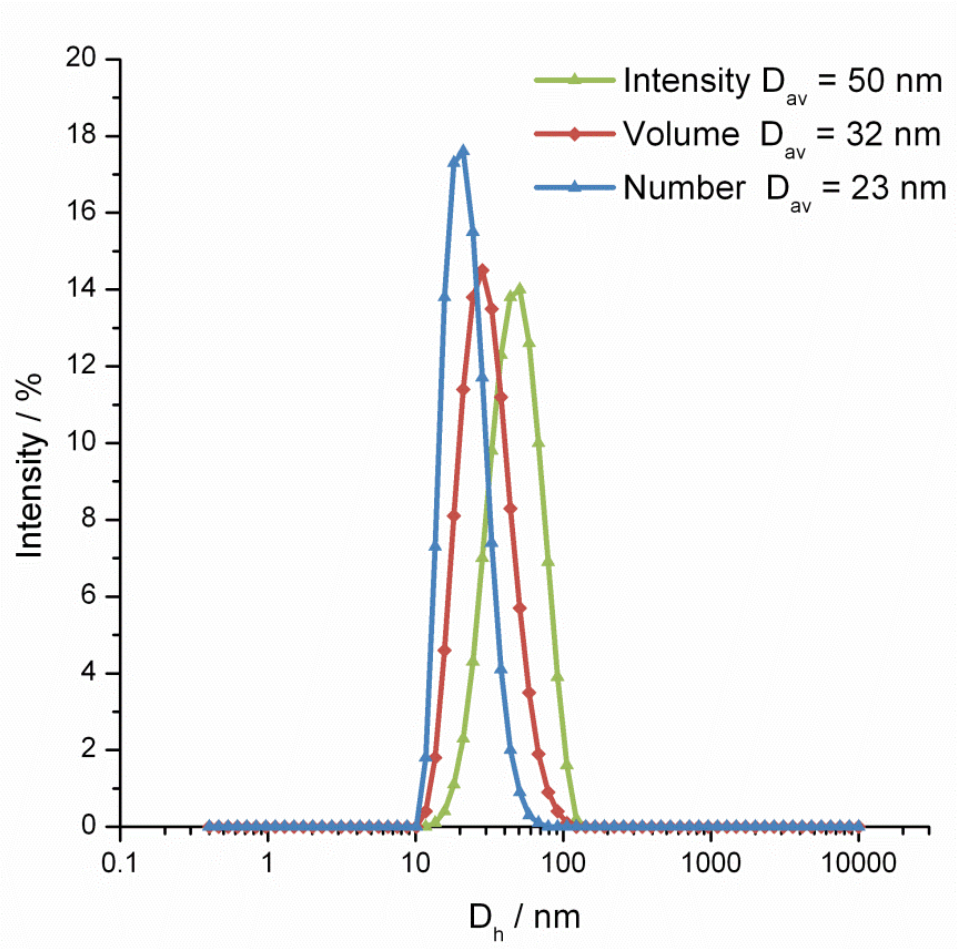

Figure B12. Intensity, Volume and number-weighted micelle size distribution obtained by DLS for **2M**, with average diameters (D_{av}).

Reprinted with permission from: Robin, M.P.; Mabire, A.B.; Damborsky, J.C.; Thom, E.S.; Winzer-Serhan, U.H.; Raymond, J.E.; O'Reilly, R.K. New Functional Handle for Use as a Self-Reporting Contrast and Delivery Agent in Nanomedicine. J. Am. Chem. Soc. 2013, 135(25), 9518. Copyright 2013 American Chemical Society.

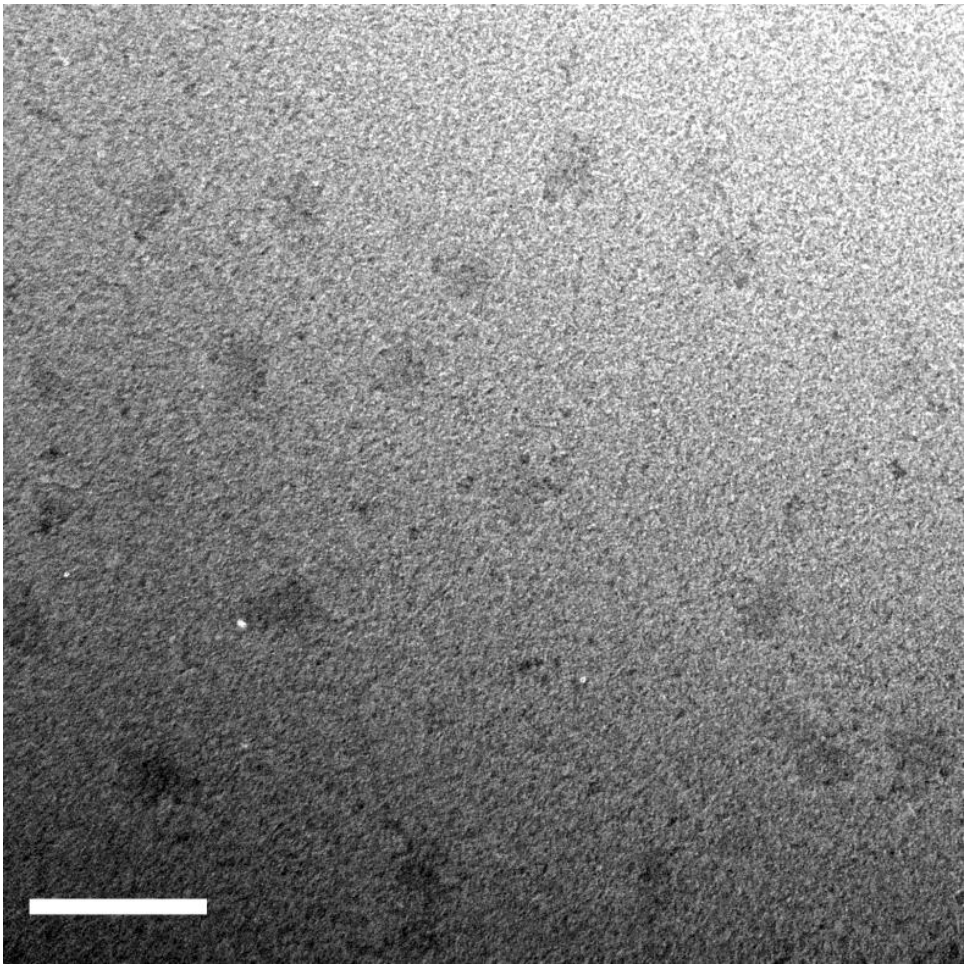

Figure B13. TEM Image of micelles **2M**, dried to a graphene oxide substrate (scale bar = 50 nm).

Reprinted with permission from: Robin, M.P.; Mabire, A.B.; Damborsky, J.C.; Thom, E.S.; Winzer-Serhan, U.H.; Raymond, J.E.; O'Reilly, R.K. New Functional Handle for Use as a Self-Reporting Contrast and Delivery Agent in Nanomedicine. J. Am. Chem. Soc. 2013, 135(25), 9518. Copyright 2013 American Chemical Society.

B.11.3 Effect of N-H Substitution to N-CH_3

In order to confirm that polymeric block-dye-block topology is responsible for the gross change in emission character when comparing **2** and **3**, and not merely the

result of aliphatic substitution of the maleimide N, a second small molecule dye **4** was synthesized (see above for synthetic protocol and characterization).

4 emission was then characterized at 100 μM in methanol and contrasted to **3** emission at 100 μM in methanol, as well as to the emission of **2M**. Steady state UV-Vis/fluorescence spectra are presented in Figure B14 and fluorescence lifetime traces for the two samples are presented in Figure B15, along with a reproduction of **2M** solution spectra for comparison in both figures.

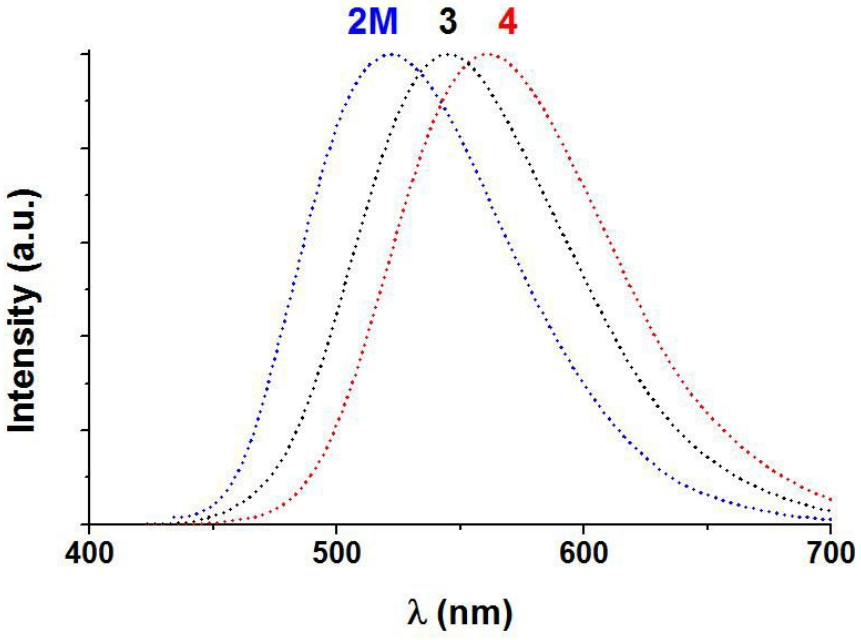

Figure B14. Emission spectra of **4**, **3** and **2M**.

Reprinted with permission from: Robin, M.P.; Mabire, A.B.; Damborsky, J.C.; Thom, E.S.; Winzer-Serhan, U.H.; Raymond, J.E.; O'Reilly, R.K. New Functional Handle for Use as a Self-Reporting Contrast and Delivery Agent in Nanomedicine. J. Am. Chem. Soc. 2013, 135(25), 9518. Copyright 2013 American Chemical Society.

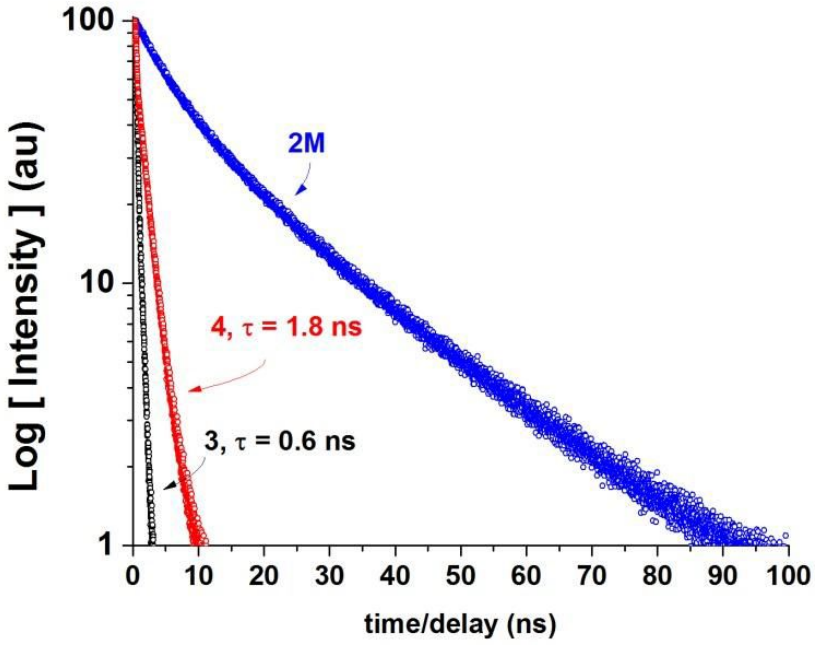

Figure B15. Emission lifetime spectra of **4**, **3** and **2M**.

Reprinted with permission from: Robin, M.P.; Mabire, A.B.; Damborsky, J.C.; Thom, E.S.; Winzer-Serhan, U.H.; Raymond, J.E.; O'Reilly, R.K. New Functional Handle for Use as a Self-Reporting Contrast and Delivery Agent in Nanomedicine. J. Am. Chem. Soc. 2013, 135(25), 9518. Copyright 2013 American Chemical Society.

It can be observed in the steady state emission spectra that incorporation of the dithiomaleimide into the polymer structure results in blue shifted emission (544 nm→522 nm) while the change from a non N-functional DTM (**3**) to an N-alkyl functional DTM (**4**) results in a red shifted emission (544 nm→562 nm). Steady state anisotropy measurements of emission at 550 nm for both **3** and **4** with 405 nm excitation were also made, providing <r> = 0.04 for **3** and <r> = 0.01 for **4**. Corrected for absorption at 405 nm for both solutions, the integrated intensities for emission showed **4** to be *ca.* 2 times more emissive than **3**. The N-methyl **4** displayed an intensity average

lifetime of 1.8 ns compared to 0.6 ns in **3**. Anisotropy decay rates for both were not significantly different (*ca.* 0.4 ns). Together, these measurements support the assertion that the differences in emissive character between **2** and **3** cannot be taken to be the result of N-substitution as the primary mode of 'on-switching' in **2**. Of note, these results suggest that the N-substitution alone provides a very different effect on emission (red shift, decreased anisotropy, nominal increase in emission lifetime and emission efficiency) and that the ultimate blue shift in **2** is primarily a function of the supermolecular architecture and supramolecular state.

B.11.4 Fluorescence of High Concentrations of 2 and 3

The block-dye-block strategy was designed to in part avoid the often laborious, low yield dye conjugation strategies employed in modern core-shell nanotheranostics. Given this target application, it is reasonable to investigate the response of this system at high concentrations, as may be found in application (leukocytes, lymphatic tissue, targeted cell types, etc.). A study of the neat **2** solid and the neat **3** liquid using FLIM was performed on the systems individually and together to be certain that the polymers degradation state at high concentrations can be elucidated. FLIM images for these systems can be found in Figure B16. Emission decay spectra, fittings and intensity average lifetimes are provided in Figure B17.

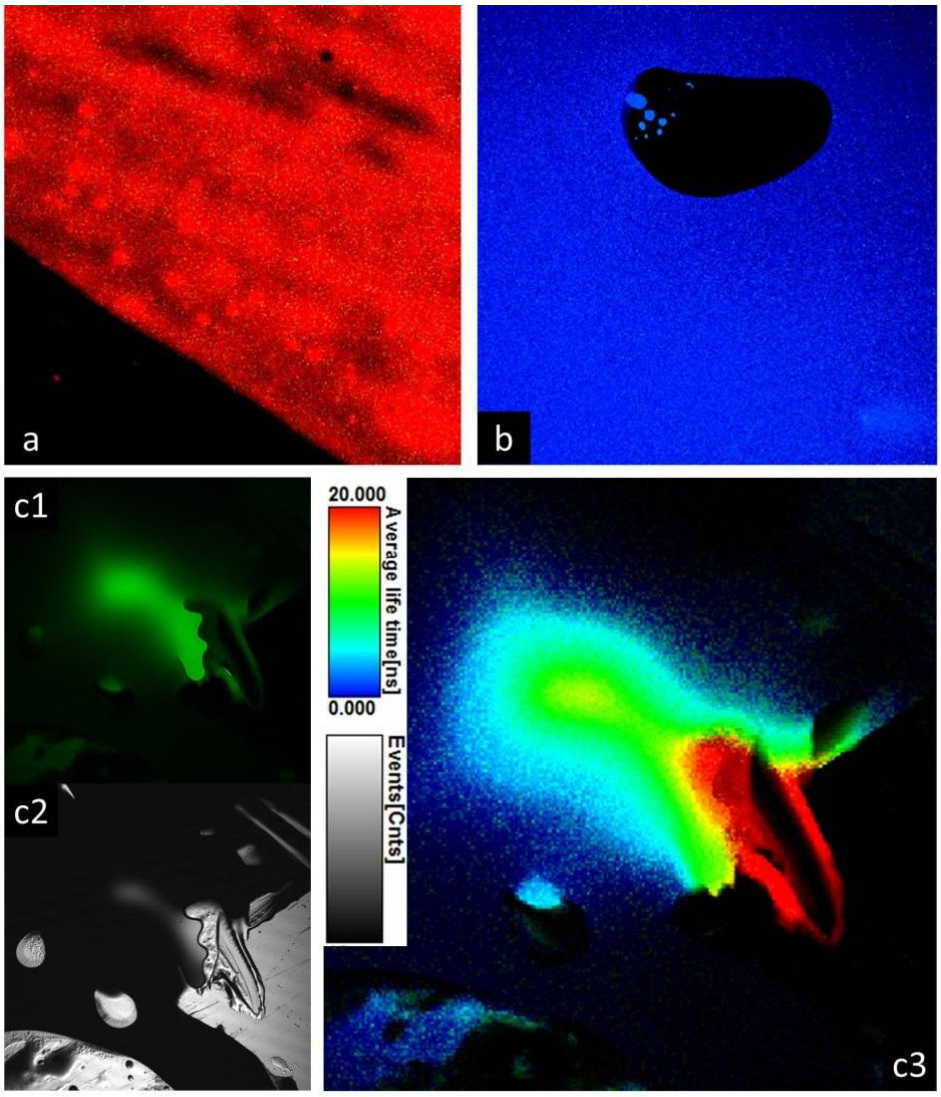

Figure B16. FLIM TCSPC spectral imaging of **2**, **3** and a **2**/**3 b**lend.

*(a) FLIM of neat polymer **2** smeared as a film onto a glass slide; (b) FLIM of neat liquid dye **3** between a glass slide and glass cover slip; (c1-c3) neat polymer **2** pressed between a glass slide and glass cover slip with neat liquid dye allowed to intercalate and interact with some regions of the polymer, (c1) confocal fluorescence image of the blend at the dye advancement front, (c2) DIC image of the same region, (c3) FLIM of the same region. Fast-FLIM lifetime color scale applies to all FLIM images. Intensity (Events) scale in grey indicates emission intensity (a.u.) for c3. Reprinted with permission from: Robin, M.P.; Mabire, A.B.; Damborsky, J.C.; Thom, E.S.; Winzer-Serhan, U.H.; Raymond, J.E.; O'Reilly, R.K. New Functional Handle for Use as a Self-Reporting Contrast and Delivery Agent in Nanomedicine. J. Am. Chem. Soc. 2013, 135(25), 9518. Copyright 2013 American Chemical Society.*

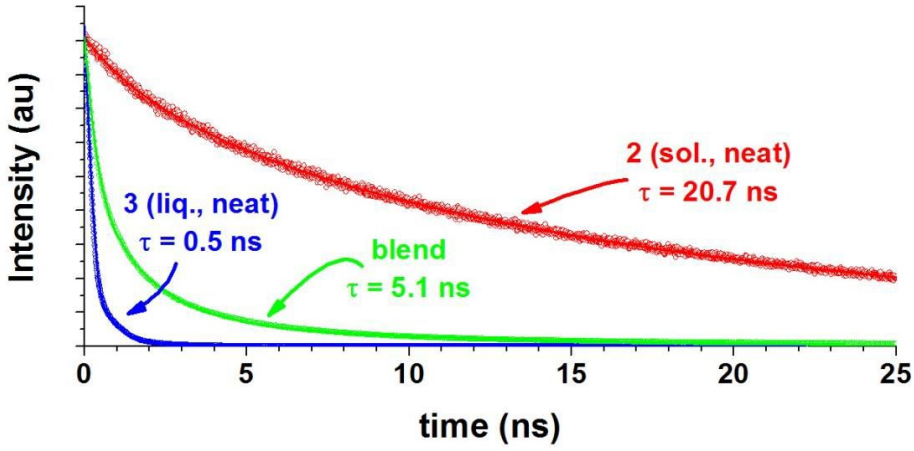

Figure B17. Full-frame emission spectra extracted from FLIM of neat **2**, **3** and **2**/**3** blend.

Raw extracted lifetime spectra for all three systems with fitting (line). Reported average fluorescence lifetime τ from (Σanτn2) / (Σ anτn) and multi-exponential decay fitting. Reprinted with permission from: Robin, M.P.; Mabire, A.B.; Damborsky, J.C.; Thom, E.S.; Winzer-Serhan, U.H.; Raymond, J.E.; O'Reilly, R.K. New Functional Handle for Use as a Self-Reporting Contrast and Delivery Agent in Nanomedicine. J. Am. Chem. Soc. 2013, 135(25), 9518. Copyright 2013 American Chemical Society.

While it is unlikely that concentrations approaching a neat sample would occur in an in vitro or in vivo environment, the differences between states in Figure B16 (c3) indicates that high concentrations of either can be rapidly determined by fast-FLIM lifetime contrast. In this figure the solvent front has advanced from the upper left (blue, low intensity) to the center of the field of view, leaving a region of untouched polymer (red, high intensity) that maintains pure neat **2** signal. For studies, like theranostic clearance studies, where disassembled nanoparticle materials need to be resolved in terms of extent of chain degradation, this contrast will be extremely useful. Additional examples of this contrast can be seen in other blend configurations/regions as presented in Figure B18.

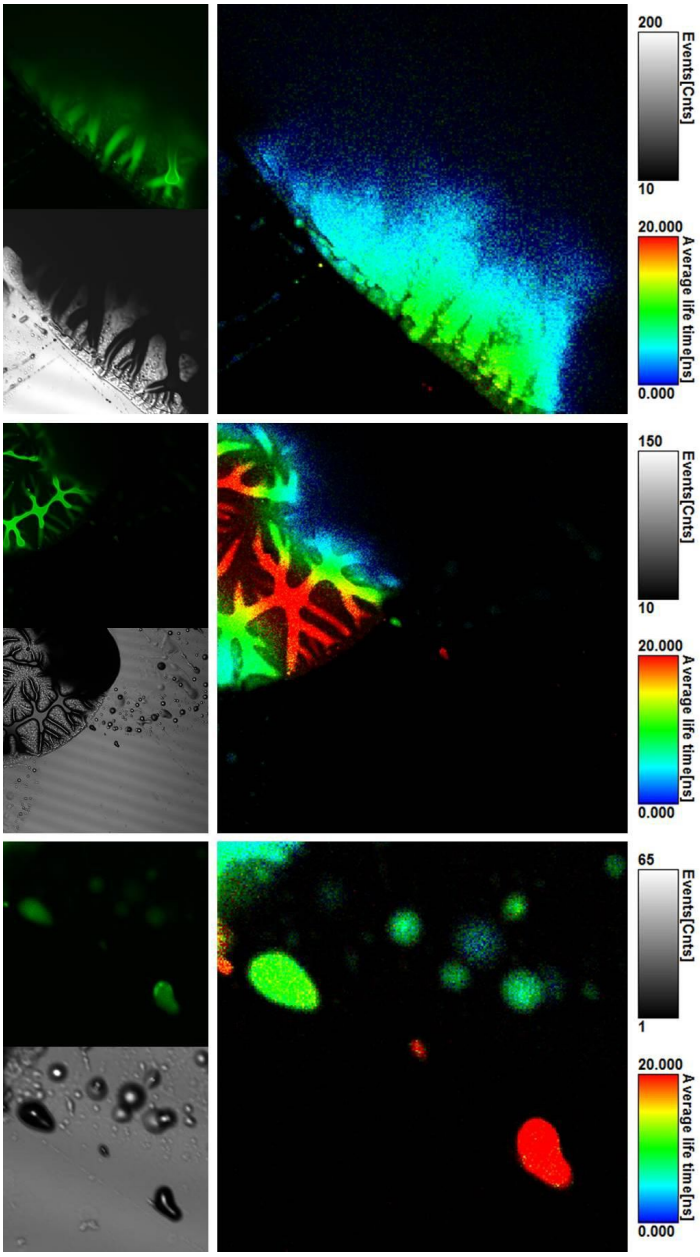

Figure B18. FLIM time domain contrast imaging of **2**/**3** blends.

*Top: fluorescence, DIC and FLIM images of a region where liquid **3** has advanced to the edge of solid **2**. Middle: fluorescence, DIC and FLIM images polymer **2** with advancing liquid **3** on both the left and right and pure neat polymer signal from the untouched region in the center. Bottom: fluorescence, DIC and FLIM images of isolated polymer regions at the dye **2** liquid front, with signal from regions outside of the front possessing longer lifetimes and those within expressing a convolution of **2** and **3** signal. Raw extracted lifetime spectra for all three systems with fitting (line). Reprinted with permission from: Robin, M.P.; Mabire, A.B.; Damborsky, J.C.; Thom, E.S.; Winzer-Serhan, U.H.; Raymond, J.E.; O'Reilly, R.K. New Functional Handle for Use as a Self-Reporting Contrast and Delivery Agent in Nanomedicine. J. Am. Chem. Soc. 2013, 135(25), 9518. Copyright 2013 American Chemical Society.*

A final comparison between the raw decay data for the FLIM signal of the C extracts region (as denoted in Figure B8) to the emission decay of **3X** by solution TCSPC is presented in Figure B19. From this comparison of decays, it is clear that the signal of the C extract region is virtually indistinguishable from the solvated **3X**. This further reinforces the application readiness of our block-dye-block architecture as a self-reporting system where the dye regions are capable of reporting on its degradation state.

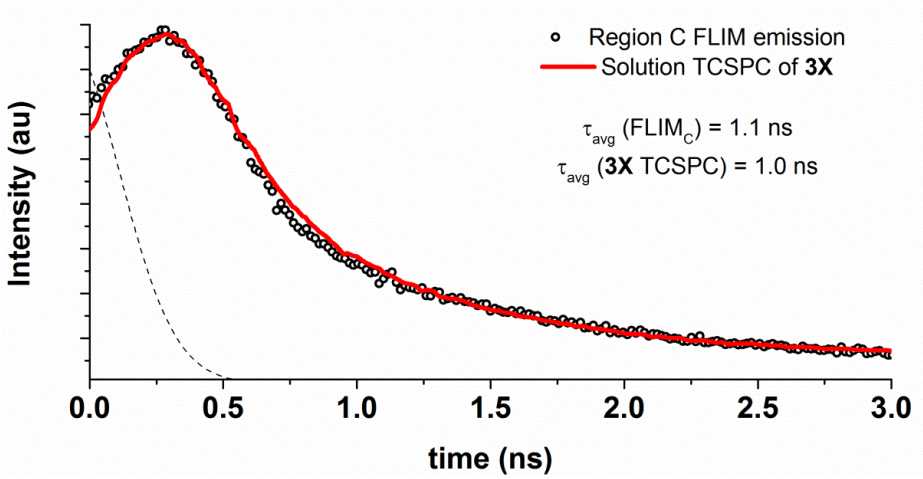

Figure B19. Comparison of raw spectral data from region C in rat hippocampal tissue and **3X** solution.

Reprinted with permission from: Robin, M.P.; Mabire, A.B.; Damborsky, J.C.; Thom, E.S.; Winzer-Serhan, U.H.; Raymond, J.E.; O'Reilly, R.K. New Functional Handle for Use as a Self-Reporting Contrast and Delivery Agent in Nanomedicine. J. Am. Chem. Soc. 2013, 135(25), 9518. Copyright 2013 American Chemical Society.

In order to determine the emission character for disordered, high concentration solutions of **2** in contrast to micellar **2**, a 1 mM (**2P**) solution in methanol was assessed by steady state anisotropy, lifetime and anisotropy decay fluorescence spectroscopies.

Steady state anisotropy from 405 nm excitation and 550 nm emission provided <r> = 0.06. Emission lifetime measurements provided a $\tau_{avg,I}$ of 19.7 ns and $\tau_{avg,A}$ of 12.2 ns and $\tau_{1/2}$ of 6.2 ns. Component lifetimes (amplitude | component lifetime) were 0.54 | 4.8 ns, 0.42 | 18.4 ns and 0.04 | 46 ns. Fluorescence anisotropy decay studies resulted in a fast decay (0.09 | 0.1 ns) and a longer decay (0.05 | 16 ns) with residuals of r_{inf} = 0.13.

When compared to the micellar **2M** solution, the largest differentiation between the two systems can be observed in <r>, the longest component lifetime, the longest anisotropy decay and the amplitude contributions of anisotropy decay. In application, these metrics will be important for distinguishing between micellar emission and high concentrations of non-micellar polymer. Table B2 highlights the key differences in the emissive character of the two systems. Of note (in terms of ease of experimental implementation) the stark contrast in steady state emission anisotropy between the **2M** and **2P** samples emerges as a metric for discrimination that could be readily utilized in wide field collection, without resorting to more costly and time consuming experimental configurations.

Attribute	2M (1μM)	2P (1 mM)	% Change
<r>	0.17	0.06	180%
τ_3	39 ns	46 ns	18%
τ_{r2}	50 ns	16 ns	210 %
a_{r2}/a_{r1}	0.26	0.56	120%

Table B2. Key differences in **2M** and **2P** emission profiles

Reprinted with permission from: Robin, M.P.; Mabire, A.B.; Damborsky, J.C.; Thom, E.S.; Winzer-Serhan, U.H.; Raymond, J.E.; O'Reilly, R.K. New Functional Handle for Use as a Self-Reporting Contrast and Delivery Agent in Nanomedicine. J. Am. Chem. Soc. 2013, 135(25), 9518. Copyright 2013 American Chemical Society.

B.11.5 References

1. Pratt, R. C.; Lohmeijer, B. G. G.; Long, D. A.; Lundberg, P. N. P.; Dove, A. P.; Li, H.; Wade, C. G.; Waymouth, R. M.; Hedrick, J. L. *Macromolecules* **2006**, *39*, 7863.
2. Ryu, J.-H.; Roy, R.; Ventura, J.; Thayumanavan, S. *Langmuir* **2010**, *26*, 7086.
3. Patterson, J. P.; Sanchez, A. M.; Petzetakis, N.; Smart, T. P.; Epps, T. H., III; Portman, I.; Wilson, N. R.; O'Reilly, R. K. *Soft Matter* **2012**, *8*, 3322.
4. Brouwer, A. M. *Pure Appl. Chem.* **2011**, *83*, 2213.
5. Suzuki, K.; Kobayashi, A.; Kaneko, S.; Takehira, K.; Yoshihara, T.; Ishida, H.; Shiina, Y.; Oishic, S.; Tobita, S. *PCCP* **2009**, *11*, 9850.
6. Damborsky, J. C.; Winzer-Serhan, U. H. *Neuroscience* **2012**, *225*, 105.

7. (a) Robin, M. P.; Jones, M. W.; Haddleton, D. M.; O'Reilly, R. K. *ACS Macro Lett.* **2012**, *1*, 222; (b) Robin, M. P.; Wilson, P.; Mabire, A. B.; Kiviaho, J.; Raymond, J. E.; Haddleton, D. M.; O'Reilly, R. K. *J. Am. Chem. Soc.* **2013**, *135*, 2875

APPENDIX C

ENHANCING THE PROTEIN RESISTANCE OF SILICONE VIA SURFACE-RESTRUCTURING PEO-SILANE AMPHIPHILES WITH VARIABLE PEO LENGTH

C.1 Published Article

Herein is a peer reviewed article to which I have contributed. Though not explicitly related to the principle subject matter of this thesis, I submit the publication as representative of my efforts while a student at Texas A&M University.

C.2 Authorship and Contributions

The authorship of this manuscript (* principle investigator, $^{+}$ first author) is as follows:

Texas A&M University; Marc A. Rufin^{+}, Melissa A. Grunlan*, Jeffery E. Raymond*, John A. Gruetzner, Matthew J. Hurley, Melissa L. Hawkins, and Elizabeth S. Raymond.

C.3 Information Related to Copyright

Reproduced by permission of The Royal Society of Chemistry (See Figure C1). To access the original article, please use the following link: http://pubs.rsc.org/en/content/articlelanding/2015/tb/c4tb02042a#!divAbstract.

This appendix has been formatted to fulfill the layout requirements of this thesis document with content only modified to meet this requirement.

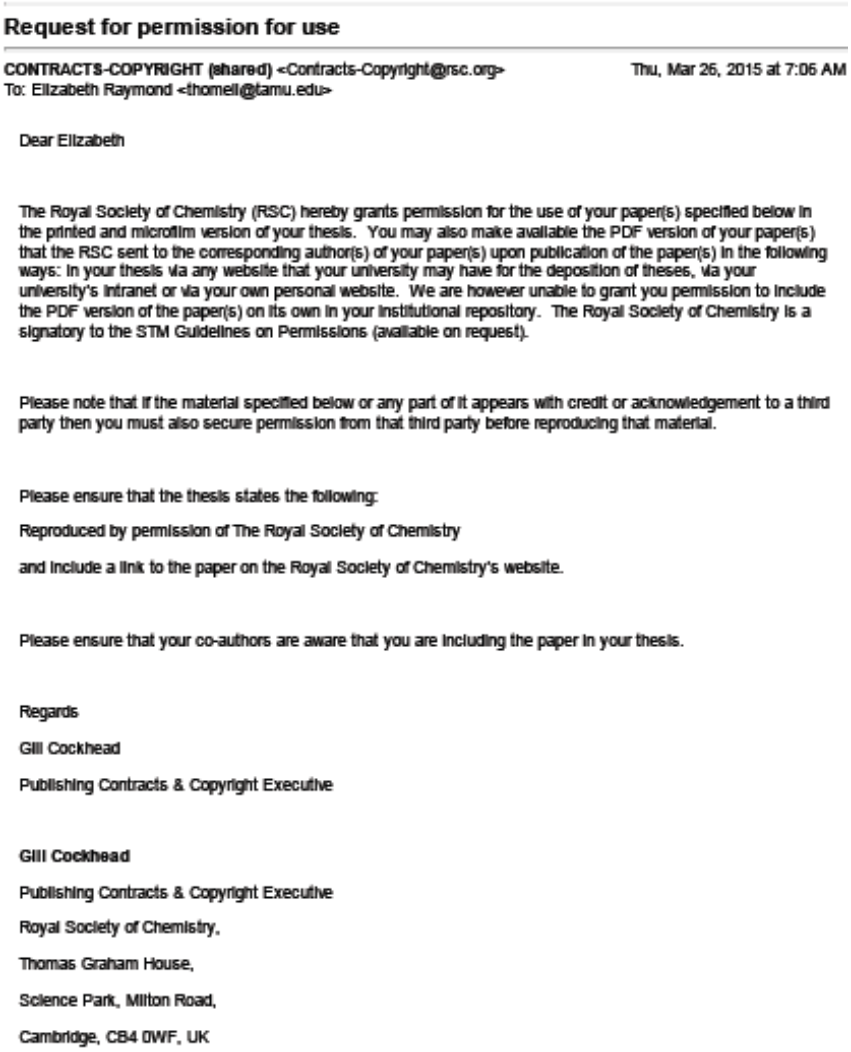

Request for permission for use

CONTRACTS-COPYRIGHT (shared) <Contracts-Copyright@rsc.org> Thu, Mar 26, 2015 at 7:06 AM
To: Elizabeth Raymond <thomeli@tamu.edu>

Dear Elizabeth

The Royal Society of Chemistry (RSC) hereby grants permission for the use of your paper(s) specified below in the printed and microfilm version of your thesis. You may also make available the PDF version of your paper(s) that the RSC sent to the corresponding author(s) of your paper(s) upon publication of the paper(s) in the following ways: in your thesis via any website that your university may have for the deposition of theses, via your university's intranet or via your own personal website. We are however unable to grant you permission to include the PDF version of the paper(s) on its own in your institutional repository. The Royal Society of Chemistry is a signatory to the STM Guidelines on Permissions (available on request).

Please note that if the material specified below or any part of it appears with credit or acknowledgement to a third party then you must also secure permission from that third party before reproducing that material.

Please ensure that the thesis states the following:

Reproduced by permission of The Royal Society of Chemistry

and include a link to the paper on the Royal Society of Chemistry's website.

Please ensure that your co-authors are aware that you are including the paper in your thesis.

Regards

Gill Cockhead

Publishing Contracts & Copyright Executive

Gill Cockhead

Publishing Contracts & Copyright Executive

Royal Society of Chemistry,

Thomas Graham House,

Science Park, Milton Road,

Cambridge, CB4 0WF, UK

Figure C1. Permission of reproduction letter

Tel +44 (0) 1223 432134

Follow the Royal Society of Chemistry:

www.rsc.org/follow

Winner of The Queen's Award for Enterprise, International Trade 2013

From: Elizabeth Raymond [mailto:thomell@tamu.edu]
Sent: 03 March 2015 07:00
To: CONTRACTS-COPYRIGHT (shared)
Subject: Request for permission for use

Hello,

My name is Elizabeth Raymond. I am an author of the following paper:

Enhancing the protein resistance of silicone via surface-restructuring PEO-silane amphiphiles with variable PEO length.

Marc Albert Rufin

, John A. Gruetzner

, Matthew J. Hurley

, Melissa L. Hawkins

, Elizabeth S. Raymond

, Jeffery E Raymond

and Melissa Ann Grunlan

Figure C1. Continued

J. Mater. Chem. B, 2015, Accepted Manuscript

DOI: 10.1039/C4TB02042A
Received 11 Dec 2014, Accepted 10 Feb 2015
First published online 13 Feb 2015

I am trying to put together my Masters thesis and I was planning on including this paper as an appendix. In order to do so, I am required to provide a letter/email from the publisher in my thesis indicating that I have been given permission to republish the work. I attempted to do so via RightsLink and was informed that attempting to reuse material from the article in my thesis was not permitted.

However, everything else I have read on the Royal Society website seemed to indicate that reproduction by an author in a thesis or dissertation is permitted. Am I allowed to reproduce this article in my thesis? If so, how can I receive permission to do so?

I appreciate you taking the time to read my email. I look forward to your response!

Best regards,

Elizabeth S. Raymond

Figure C1. Continued

C.4 Abstract

Silicones with superior protein resistance were produced by bulk-modification with poly(ethylene oxide) (PEO)–silane amphiphiles that demonstrated a higher capacity to restructure to the surface–water interface versus conventional non-amphiphilic PEO–silanes. The PEO–silane amphiphiles were prepared with a single siloxane tether length but variable PEO segment lengths: α-$(EtO)_3Si(CH_2)_2$-oligodimethylsiloxane$_{13}$-*block*-poly(ethylene oxide)$_n$-OCH_3 (n = 3, 8, and 16). Conventional PEO–silane analogues (n

¼ 3, 8, and 16) as well as a siloxane tether-silane (*i.e.* no PEO segment) were prepared as controls. When surface-grafted onto silicon wafer, PEO–silane amphiphiles produced surfaces that were more hydrophobic and thus more adherent towards fibrinogen *versus* the corresponding PEO–silane. However, when blended into a silicone, PEO–silane amphiphiles exhibited rapid restructuring to the surface–water interface and excellent protein resistance whereas the PEO–silanes did not. Silicones modified with PEO–silane amphiphiles of PEO segment lengths $n = 8$ and 16 achieved the highest protein resistance.

C.5 Introduction

Silicones, particularly silica-reinforced, crosslinked poly-dimethylsiloxane (PDMS), are widely used for medical, marine and industrial applications. These include blood-contacting devices (*e.g.* hemodialysis catheters, catheter balloons and cardiac pacing leads)[1–3] and marine coatings.[4] Unfortunately, as a result of their extreme hydrophobicity, the performance of silicones is severely limited by poor resistance to biomolecules such as proteins.[5,6] For example, in the case of blood-contacting devices, the non-specific adsorption of plasma proteins is considered the first step of thrombosis and even infection.[7–9] Various modifications have been utilized to hydrophilize silicones in order to reduce protein adsorption, including physical, chemical and combined approaches.[10–14]

Silicone modification with poly(ethylene oxide) (PEO; or poly(ethylene glycol) (PEG)) represents arguably the most widely utilized method for enhancing hydrophilicity and protein resistance.[15–19] The exceptional protein resistance of PEO is attributed to its hydrophilicity and hydration, as well as its configurational mobility.[20–23] The biocompatibility[24] and recently demonstrated *in vivo* oxidative stability[25] of PEO contributes to its widespread use. Notably, the protein resistance of PEO has largely been assessed for chains surface-grafted onto physically stable substrates such as gold,[26–28] silicon[29–31] and glass.[32,33] For these "model PEO surfaces," PEO chains are maintained at the surface irrespective of the environment (*i.e.* air *versus* water). In contrast, PEO chains incorporated into silicones are subject to surface reorganization upon exposure to a different environment.[34] This process has been studied mainly in terms of hydrophobic recovery (*i.e.* loss of hydrophilicity with exposure to air) such as that observed for plasma treated silicones.[35] This behavior is attributed to the low surface energy of silicones,[36,37] coupled with their high chain flexibility.[38,39] For example, hydrophobic recovery has been observed for PEO-modified silicones formed by bulk crosslinking with triethoxysilylpropyl PEO monomethyl ether [$(EtO)_3Si(CH_2)_3$-$(OCH_2CH_2)_x$-OCH_3][40,41] as well as allyl PEO monomethyl ether [CH_2═$CHCH_2$-$(OCH_2CH_2)_x$-OCH_3].[42] Hydrophobic recovery is also observed for surface-grafted PEO chains such as those prepared with allyl PEO monomethyl ether.[42,43] However, since biofouling events such as protein adsorption occur in an aqueous environment, the rapid and substantial surface restructuring of PEO to the surface–water interface is of critical importance.

Towards the goal of enhancing the protein resistance of silicones, we sought to improve the capacity of PEO to migrate to the surface–water interface by altering its molecular structure. Previously, we reported PEO–silane amphiphiles prepared with a siloxane tether of varying lengths (*m*) separating the PEO segment from the crosslinkable ethoxy silane groups [$\alpha(EtO)_3$-$Si(CH_2)_2$-oligodimethylsiloxane$_m$-$(OCH_2CH_2)_8$-OCH_3; m = 0, 4, and 13].[44] The siloxane tether distinguishes the PEO–silane amphiphiles from the analogous conventional PEO–silanes noted above which contain a short alkane (*e.g.* propyl) spacer.[40–43] The siloxane tether is characterized by high flexibility resulting from the wide bond angle (~145°) and low barrier to linearization (~0.3 kcal mol^{-1}) of Si–O–Si dimethylsiloxane bonds, features that give rise to low glass transition temperatures (*e.g.* PDMS, T_g = -125 °C).38,39 Like a silicone elastomer, the siloxane tether is also hydrophobic, imparting an amphiphilic character to these PEO–silanes. We anticipated that the flexibility and similarly hydrophobic nature of the siloxane tether would facilitate water-driven migration to the surface of a bulk-modified silicone thereby reducing protein adsorption. Indeed, when the PEO–silane amphiphiles (m = 0, 4, and 13) were bulk crosslinked with α,ω-bis(Si–OH) PDMS (M_n = 3000 g mol^{-1}), protein resistance,[44] as well as bacteria and diatom resistance,[45] increased with siloxane tether length. Furthermore, extensive atomic force microscopy (AFM) analysis has confirmed the water-driven migration of PEO to these silicone coating surfaces to form nanocomplex surfaces.[46] Herein, we evaluated the impact of PEO segment length by bulk crosslinking a medical grade RTV silicone with three PEO–silane amphiphiles of different PEO segment lengths (n = 3, 8, and 16) and a single

siloxane tether length (m = 13) (Fig. C2). Given the protein resistance of PEO oligomers when surface-grafted onto a model substrate,[26] the PEO–silane amphiphile (n = 8) was selected for our previous work to enhance the protein resistance of bulk-modified silicones.[44,46–49] Thus, for this study, values of "n" (3, 8, and 16) were chosen as they are "substantially" different from one another (by a factor of approximately two) and thus were predicted to have different restructuring potentials. Analogous conventional PEO–silanes or "PEO-controls" (*i.e.* no siloxane tether, n = 3, 8, and 16) as well as a "siloxanecontrol" (*i.e.* no PEO segment, m = 13) were likewise evaluated to highlight the effect of the siloxane tether. Water-driven surface restructuring was quantified by temporal static contact angle analysis of water droplets, and resistance to fibrinogen was also measured. In addition, PEO–silane amphiphiles, $PEO_{controls}$ and the siloxane-control were each surface-grafted onto silicon wafers in order to evaluate their protein resistance in the absence of surface restructuring. This study therefore represents an effort to better understand the influence of the siloxane tether and PEO segment length on the protein resistance and surface restructuring of PEO–silanes through systematic comparisons *versus* controls.

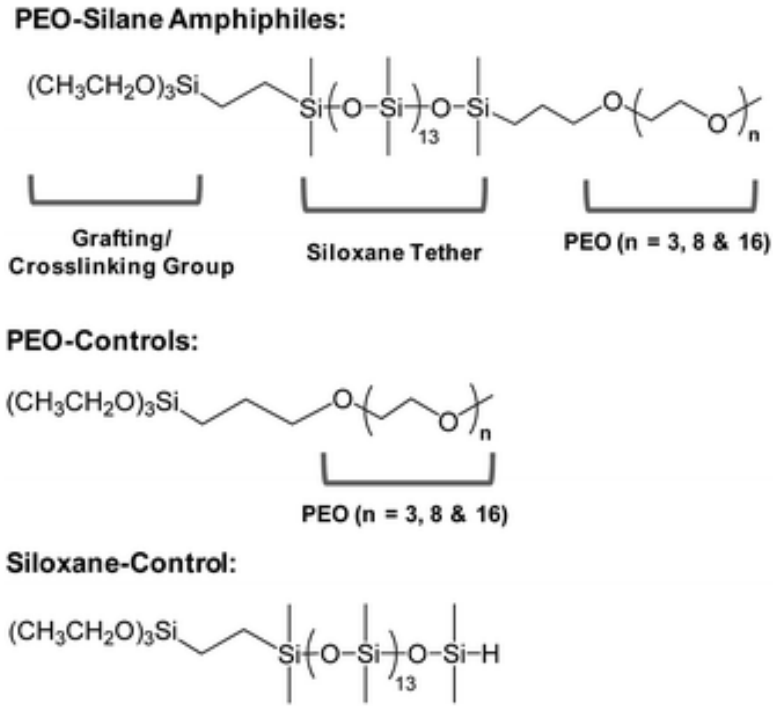

Figure D2. Structures of PEO-silane amphiphiles, PEO-silane controls and siloxane control

C.6 Results and Discussion

C.6.1 Surface-Grafted Coatings on Silicon Wafers

The protein resistance of PEO–silane amphiphiles (n = 3, 8, and 16) in the absence of water-driven restructuring to the surface was evaluated with surface-grafted coatings prepared on silicon wafers. PEO-controls (n = 3, 8, and 16) and the siloxane-control were likewise evaluated to elucidate the impact of the siloxane tether.

C.6.1.1 X-ray Photoelectron Spectroscopy (XPS)

The surface-grafting of conventional PEO–silanes onto silicon wafers has been widely reported.[29–31] Likewise, the successful surface-grafting of PEO–silane amphiphiles (n = 3, 8, and 16) was confirmed via XPS with the PEO-control (n = 8) and siloxane-control serving as controls. Surface elemental atomic percent compositions are reported in Table 1. For the oxidized silicon wafer, the 1s and Si 2p peaks correspond to the wafer composition whereas the carbon (C 1s) is attributed to adsorbed contaminants.[50,51] Following surface-grafting, a decrease in Si 2p and increase in C 1s content was observed as expected. To further confirm surface-grafting, the C 1s peak was deconvoluted into two peaks of different binding energies and normalized to the peak centered at 284.5 eV (Fig. C3). These peaks correspond to the C–C/C–Si (at 284.5 eV) and C–O (at 286.4 eV) of PEO.[43] The areas of the C–C/C–Si and C–O peaks are reported in Table C1. When surfaces were grafted with PEO–silane amphiphiles, C–O content increased with PEO-segment length (n) and a concomitant decrease in C–C/C–Si content was also observed. As expected, the relative quantity of C–O on the surface grafted with the PEO-control was greatest due to the absence of C–Si associated with the siloxane tether that was present on all other samples. Finally, for the surface-grafted siloxane-control, C–O content was very low and may be attributed to residual unreacted ethoxy groups. Together, these results confirm the successful grafting of PEO–silane amphiphiles to silicon wafers.

Surface	C 1s Total	C–Si/C–C 284.5 eV	C–O 286.4 eV	O 1s	Si 2p
Oxidized silica	5			34	61
Siloxane-control	34	94	6	29	38
$n = 3$	24	82	18	29	47
$n = 8$	22	71	29	34	44
$n = 16$	26	48	52	33	42
PEO-control ($n = 8$)	26	38	62	35	38

Table C1. Surface atomic % composition by XPS

Reproduced by permission of The Royal Society of Chemistry. To access the original article, please use the following link: http://pubs.rsc.org/en/content/articlelanding/2015/tb/c4tb02042a#!divAbstract.

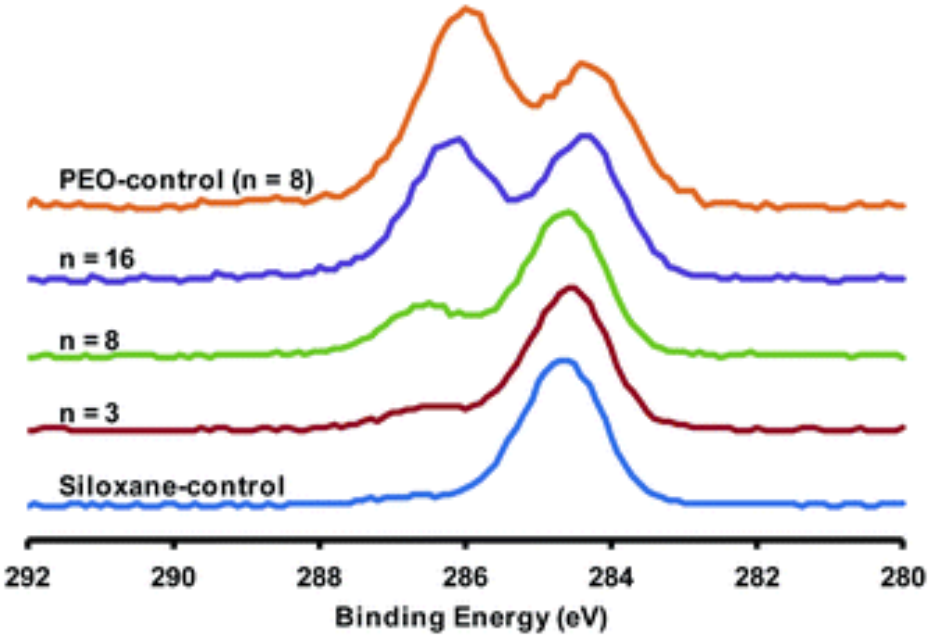

Figure C3. HR C 1s XPS spectra of silicon wafers grafted with PEO–Silane amphiphiles (n = 3, 8, and 16) as well as the PEO-control (n = 8) and Siloxane-control

Reproduced by permission of The Royal Society of Chemistry. To access the original article, please use the following link: http://pubs.rsc.org/en/content/articlelanding/2015/tb/c4tb02042a#!divAbstract.

C.6.1.2 Ellipsometry

As chain spacing is known to influence the protein resistance of grafted PEO coatings,[52,53] it was important to ensure that the graft density was similar for all samples using ellipsometry. Dry thickness values (h) of grafted PEO–silane amphiphiles, PEO-controls, and siloxane-control were measured and the obtained values of h were then used to estimate the chain density (σ) (Table D2):[54–56]

$$\sigma = (h\rho N_A)/M_n \quad (1)$$

where ρ is the density of the dry grafted layer, N_A is Avogadro's number and M_n is the number average molecular weight of the chain. The chain distance or "spacing" (D, nm) (i.e. distance between grafting sites) was also calculated (Table C2):[56]

$$D = (4/\pi\sigma)^{1/2} \quad (2)$$

Surface	M_n (g mol^{-1})	Density ρ (g mL^{-1})	Measured thickness h (nm)	Chain density $\sigma = (h\rho N_A)/M_n$ (chains per nm^2)	Chain spacing $D = (4/\pi\sigma)^{1/2}$ (nm)	PEO Flory spacing $2R_f = 2\ aN^{3/5}$ (nm)	Siloxane Flory spacing $2R_f = 2\ aN^{1/3}$ (nm)
Siloxane-control	1286	1.01	2.5 ± 0.9	1.2 ± 0.4	1.1 ± 0.2	n/a	2.4
PEO-control ($n = 3$)	368	1.04	0.6 ± 0.1	1.0 ± 0.2	1.1 ± 0.1	1.4	n/a
PEO-control ($n = 8$)	588	1.13	2.3 ± 0.2	2.6 ± 0.2	0.70 ± 0.03	2.4	n/a
PEO-control ($n = 16$)	940	1.16	1.2 ± 0.2	0.9 ± 0.2	1.2 ± 0.1	3.7	n/a
Amphiphile ($n = 3$)	1490	1.04	2.1 ± 0.2	0.9 ± 0.1	1.2 ± 0.1	1.4	2.4
Amphiphile ($n = 8$)	1710	1.13	1.7 ± 0.2	0.6 ± 0.1	1.4 ± 0.1	2.4	2.4
Amphiphile ($n = 16$)	2062	1.04	3.1 ± 0.8	0.9 ± 0.2	1.2 ± 0.1	3.7	2.4

Table C2. Surface atomic % composition by XPS

Utilizing the described grafting conditions, all grafted layers were found to have similar chain spacing (D) (1.0–1.5 nm) except for the PEO-control (n = 8). Initially, this particular composition yielded high values of h (~4.3 nm) which are significantly higher than the fully extended chain length of the PEO segment (~2.8 nm),[57] indicative of substantial multilayer formation. To prevent multilayer formation and increase D, the grafting conditions for the PEO-control (n = 8) were adjusted as follows: grafting solution concentration = 0.006 M, exclusion of water droplet from grafting solution, and cure under vacuum at RT.

For all compositions of surface-grafted chains to be in the brush regime, D must be less than twice the Flory radius ($2R_f$).[53] For each chain composition, R_f was calculated on the basis of the length of one monomer (a) and the degree of polymerization (N) as follows:[53,58,59] (i) for the siloxane-control in a poor solvent (water): $R_f = aN^{1/3}$, where a =

0.5 nm and $N = 13$ and (ii) for the PEO-controls in a good solvent (water): $R_f = aN^{3/5}$, where $a = 0.35$ nm and $N = n$. For all of these controls, $D < 2R_f$. Calculation of R_f for the PEO–silane amphiphiles is complicated by the fact that these contain two "blocks" (i.e. siloxane tether and PEO segment) of differing solubility in water. Thus, R_f was individually calculated on the basis of both the siloxane tether and the PEO segment[47] using the aforementioned equations. For all grafted PEO–silane amphiphiles, $D < 2R_f$, even when considering the lower of the two calculated R_f values. Thus, for all grafted chains, a brush regime was obtained.

C.6.1.3 Water Contact Angle Analysis

An oxidized silicon wafer provides a physically stable surface such that the concentration of grafted chains is maintained at the surface, irrespective of an air or water environment. Thus, the impact of PEO–silane amphiphile structure, including PEO segment length, on surface wettability (*i.e.* θ_{static}) may be elucidated by comparing these grafted surfaces to those prepared with the PEO-controls and the siloxane-control. θ_{static} was measured immediately after water droplet deposition (0 s) and at 2 min (Fig. C4; Table C9). For all grafted surfaces, θ_{static} (0 s) was very similar to θ_{static} (2 min) due to the expected lack of surface restructuring. For the siloxane-control grafted surface, the hydrophobicity of the siloxane tether (and the absence of a hydrophilic PEO segment) led to a hydrophobic surface as characterized by $\theta_{static} > 90°$.[60] In the case of PEO-control grafted surfaces, surface hydrophilicity increased (*i.e.* θ_{static} decreased) with

increased PEO-segment length (*n*). This trend was likewise observed for PEO–silane amphiphile grafted surfaces. However, due to the contributions of the PEO–silane amphiphiles' hydrophobic siloxane tethers, these surfaces were substantially more hydrophobic versus the corresponding PEO-controls (*i.e.* same *n*).

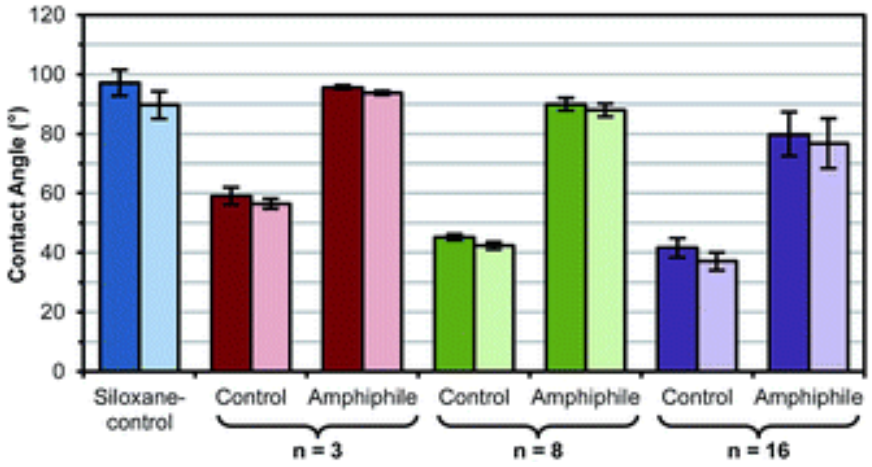

Figure C4. Static contact angle (θ_{static}) of surface-grafted silicon wafers at 0 s (dark) and 2 min (Light) following placement of water droplet

Each bar represents the average and standard deviation of measurements performed in triplicate on four identically prepared samples. Reproduced by permission of The Royal Society of Chemistry. To access the original article, please use the following link: http://pubs.rsc.org/en/content/articlelanding/2015/tb/c4tb02042a#!divAbstract.

C.6.1.4 Protein Adsorption

Human fibrinogen (HF) was chosen as the protein for these adsorption studies due to its well-established influence in surface-induced thrombosis by causing platelet adhesion and activation.[61–66] Its use in evaluating the thromboresistance of materials in

vitro has also been well established.[26,40,46–49,53,54,63,67–71] Adsorption of HF onto surface-grafted silicon wafers was measured by quartz crystal microbalance with dissipation monitoring (QCM-D) (Fig. C5). QCM-D has been widely used for measuring adsorption of proteins on low-fouling grafted monolayers and thin films.[70,72–74] The Sauerbrey model was used to approximate the mass of fibrinogen due to the relatively low dissipation of the adsorbed protein.[68] Furthermore, the changes in frequency and dissipation for the most protein-resistant surfaces were too small for the software to accurately calculate the mass using a viscoelastic (Voigt) model. Mass was calculated from the seventh overtone of frequency.

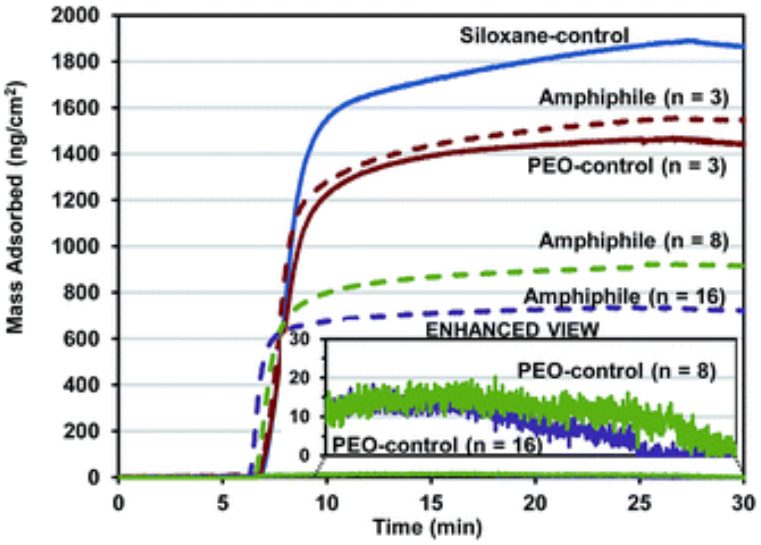

Figure C5. QCM-D-measured adsorption of human fibrinogen (HF) onto silica-coated sensors grafted with the siloxane-control [blue solid line], PEO–Silane mphiphiles (*n* = 3, 8, and 16) [dashed lines] and PEO-Controls (*n* = 3, 8, and 16) [solid lines]

After equilibration for 5 min with PBS, the sensors were exposed to HF for 20 min and then to PBS for 5 min. Reproduced by permission of The Royal Society of Chemistry. To access the original article, please use the following link: http://pubs.rsc.org/en/content/articlelanding/2015/tb/c4tb02042a#!divAbstract.

Proteins, including HF, are known to adsorb more onto hydrophobic versus hydrophilic surfaces.[75,76] Indeed, the degree of hydrophobicity of the grafted surfaces (as indicated by θ_{static} reported in Fig. C4) correlates well with the observed amounts of HF adsorbed (Fig. C5). For instance, the siloxane-control produced the most hydrophobic grafted surface which led to the highest level of HF adsorption. Due to increasing hydrophilicity, the protein resistance of grafted surfaces with PEO–silane amphiphiles as well as PEO-controls increased with PEOsegment length (*n*). Notably, for a given PEO-segment length (*n*), the PEO–silane amphiphile adsorbed more HF than the PEO control which is consistent with the higher hydrophobicity of the former. These results agree with the exceptionally low fouling nature observed for PEO chains grafted onto stable surfaces.[26,28–30,32,33]

C.6.2 Bulk-Modified Silicone Coatings

In order to evaluate the capacity of the silanes to undergo waterdriven surface reorganization and reduce protein adsorption, a medical-grade RTV silicone was bulk-modified with PEO–silane amphiphiles (*n* = 3, 8, and 16), PEO-controls (*n* = 3, 8, and 16) and the siloxane-control. Each silane was introduced at a constant level (50 μmol of silane per 1.0 g silicone) and the solvent-cast films were cured on glass slides (Fig. C6). The thicknesses of all films were measured by an electronic caliper and found to be 0.14 ± 0.01 mm. When modified with the hydrophobic siloxane-control, the coating appearance resembled that of the unmodified silicone. The lack of increased opacity of

these films was attributed to the solubility of the siloxane-control in the silicone matrix. In contrast, silicones modified with PEO-controls were substantially more opaque and notably so when compared to those prepared with the corresponding PEO–silane amphiphiles. Opacity increased, particularly for the PEO-controls, as the PEO-segment length (*n*) increased. The lesser increase in opacity of silicones modified with PEO–silane amphiphiles may be attributed to reduced phase separation stemming from the solubility of the hydrophobic siloxane tether in the silicone matrix.

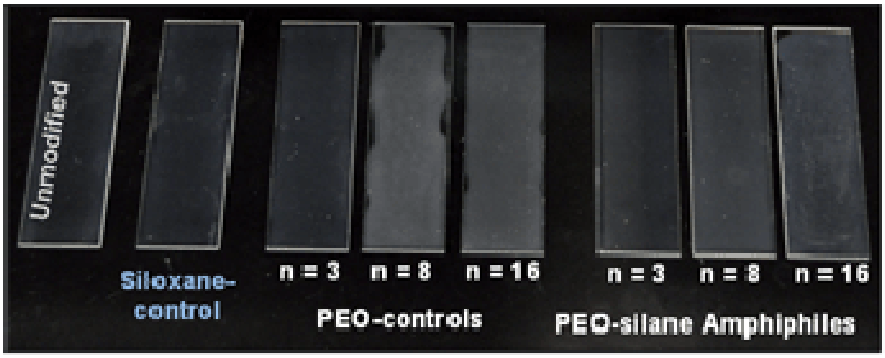

Figure C6. Unmodified silicone and silicones bulk-modified with PEO–silane amphiphiles (*n* = 3, 8, and 16), PEO-controls (*n* = 3, 8, and 16) and the Siloxane-control

C.6.2.1 Water Contact Angle Analysis

As noted, AFM was previously used to confirm the water-driven formation of a PEO-enriched surface for silicone modified with the PEO–silane amphiphile (*n* = 8).[46] Water-driven surface restructuring of bulk-modified silicones was evaluated by

temporally measuring qstatic of a water droplet placed on the surface over a 3 min period (Fig. C7, Table C10). As expected, the unmodified silicone was very hydrophobic and the θ_{static} value did not change significantly during the 3 min measurement. The siloxane-control produced a modified silicone that was also very hydrophobic but displayed a slight decrease in θ_{static} over 3 min (Δ = ~12°). However, at 3 min, θ_{static} was still >90° and therefore hydrophobic.[60] Notably, silicones modified with PEO-controls also remained hydrophobic after 3 min ($\theta_{static,3min}$ > 90°), similarly exhibiting only a moderate decrease in θ_{static} 3 min after droplet deposition (n = 3, Δ = ~19°; n = 8, Δ = ~15°; n = 16, Δ = ~12°). Thus, the PEO-controls demonstrated a limited capacity to migrate to the surface–water interface and hydrophobicity was only slightly diminished with decreased PEO length. In contrast, when modified with PEO–silane amphiphiles, silicone surfaces underwent extensive and rapid water-driven surface reorganization as noted by large decreases in θ_{static} over a 3 min period (n = 3, Δ = ~33°; n = 8, Δ = ~88°; n = 16, Δ = ~59°). Thus, the siloxane tether critically facilitates the migration of PEO segments to the surface–water interface. Due to this enhanced surface reorganization, initially hydrophobic surfaces quickly became more hydrophilic, with hydrophilicity increasing in the order: n = 3 ($\theta_{static,3min}$ = ~84°) < n = 16 ($\theta_{static,3min}$ = ~57°) < n = 8 ($\theta_{static,3min}$ = ~29°). Thus, the PEO segment length of PEO–silane amphiphiles produced an obvious impact. For n = 8, modified silicones displayed the greatest decrease in θ_{static} over 3 min (*i.e.* Δ) and also achieved the highest hydrophilicity (*i.e.* $\theta_{static,3min}$). For n = 16, the longer PEO segment length likely imparts a greater steric challenge for water-driven surface reorganization. In contrast, for n = 3, while short PEO segments may

more readily move to the surface–water interface, the reduced number of PEO repeating units diminishes the relative potential to increase hydrophilicity.

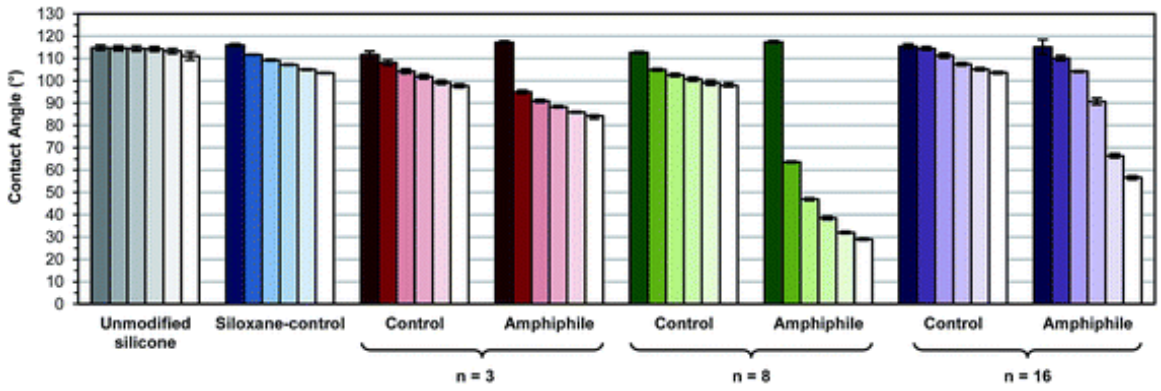

Figure C7. Static water contact angles measured over three minutes on bulk-modified silicone films. Bars are organized as the time after initial drop placement from dark color to light as follows: 0 s, 15 s, 30 s, 1 min, 2 min and 3 min. Each bar represents the average of three contact angles measured at the same time point on the same sample and the error bar is the standard deviation

C.6.2.2 Protein Adsorption

Protein resistance of the bulk-modified silicone "thick" films was determined *via* confocal microscopy.[44,46,48,49] Adsorption of fluorescently-labeled HF (100 μg mL^{-1}) was measured on silicone in terms of absolute fluorescence intensity (Table C11) and that normalized to unmodified silicone (Fig. C8). The unmodified silicone, due to its high hydrophobicity, resulted in characteristically high protein adsorption. Due to its hydrophobic nature, the siloxane-tether produced modified silicones with similarly high

protein adsorption. Despite modification of silicones with PEO-controls (n = 3, 8, and 16), protein adsorption was also high. This is notably contrary to the high protein repellency of PEO-controls when grafted onto silicon wafers (Fig. C5). This can be explained by the contact angle analysis that demonstrates that the PEO segments comprising the PEO-controls are severely inhibited in their migration to the surface–water interface where protein adsorption occurs (Fig. C7). The PEO–silane amphiphile (n = 3), due to its short PEO segment length and corresponding inability to effectively hydrophilize the surface–water interface (Fig. C7), also produced modified silicones that adsorbed high levels of protein. However, distinctively low protein adsorption was observed for silicones modified with PEO–silane amphiphiles (n = 8 and 16), with the PEO–silane amphiphile (n = 8) yielding the lowest of the two. This agrees with the contact angle analysis that shows the rapid transition from a hydrophobic to hydrophilic surface, indicative of highly efficient water-driven PEO surface migration (Fig. C7). Thus, while these PEO–silane amphiphiles demonstrated reduced protein repellency versus the corresponding PEO-controls when surface-grafted onto silicon wafers (Fig. C5), they are superior and highly effective in reducing protein adsorption onto bulk-modified silicones.

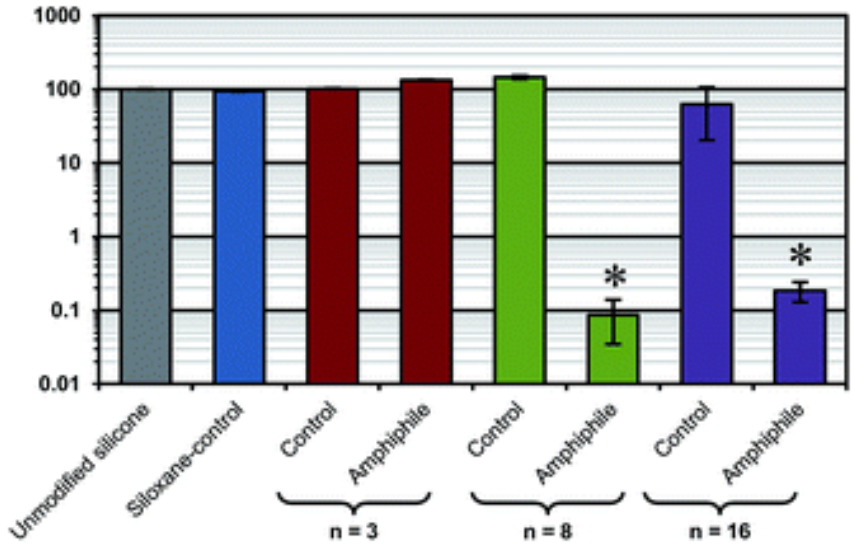

Figure C8. Fibrinogen adsorption on bulk-modified silicones as measured by fluorescence intensity with confocal microscopy. Each bar represents the average and standard deviation of pixel intensity for three images normalized to unmodified silicone. Statistical significance was determined for low-fouling samples by one-way analysis of variance (Holm–Sidak method where * indicates $p < 0.05$)

C.7 Experimental

C.7.1 Materials

Vinyltriethoxysilane (VTEOS), triethoxysilane, α,ω-bis-(SiH)oligodimethylsiloxane [M_n = 1000–1100 g mol^{-1} per manufacturer's specifications; M_n = 1096 g mol^{-1} per ^{1}H NMR end group analysis; ^{1}H NMR (δ, ppm): 0.05–0.10 (m, 78H, $SiCH_3$), 0.19 (δ, J = 2.7 Hz, 12H, $OSi[CH_3]_2H$) and 4.67–4.73 (m, 2H, SiH)] and allyl methyl PEO3 [M_n = 204 g mol^{-1} per manufacturer's specifications; M_n = 204 g mol^{-1}

per ^{1}H NMR end group analysis; ^{1}H NMR (δ, ppm): 3.35 (s, 3H, OCH_3), 3.50–3.67 (m, 12H, OCH_2CH_2), 4.00 (dt, J = 6.0 and 1.5 Hz, 2H, CH_2═$CHCH_2O$), 5.13–5.28 (m, 2H, CH_2═$CHCH_2O$) and 5.82–5.96 (m, 1H, CH_2═$CHCH_2O$)] were purchased from Gelest. Allyl methyl PEO [Polyglykol AM 450, M_n = 292–644 g mol^{-1} per manufacturer's specifications; M_n = 424 g mol^{-1} per ^{1}H NMR end group analysis; ^{1}H NMR (δ, ppm): 3.35 (s, 3H, OCH_3), 3.51–3.66 (m, 32H, OCH_2CH_2), 4.00 (δ, J = 5.4 Hz, 2H, CH_2═$CHCH_2O$), 5.13–5.28 (m, 2H, CH_2═$CHCH_2O$) and 5.82–5.96 (m, 1H, CH_2] $CHCH_2O$)] was graciously provided by Clariant. Anhydrous magnesium sulfate ($MgSO_4$), hydrogen peroxide (H_2O_2) solution (30%), glass microscope slides (75 mm x 25 mm x 1 mm), and phosphate buffer solution (PBS, without calcium and magnesium, pH = 7.4) were purchased from Fisher. Sulfuric acid (H_2SO_4, 95–98%), PEO methyl ether [M_n = 750 g mol^{-1} per manufacturer's specifications, M_n = 736 g mol^{-1} per ^{1}H NMR end group analysis; ^{1}H NMR (δ, ppm): 3.37 (s, 3H, OCH_3) and 3.53–3.73 (m, 64H, OCH_2CH_2)], sodium hydride (NaH; 60 wt% dispersion in mineral oil), allyl bromide, $RhCl(Ph_3P)_3$ (Wilkinson's catalyst), Pt-divinyltetramethyl–disiloxane complex (Karstedt's catalyst), and human fibrinogen (HF; M_w = 340 kDa; lyophilized powder; ≥90% clottable protein) were purchased from Sigma-Aldrich and were used as received. Organic solvents were also purchased from Sigma-Aldrich and were dried over 4 Å molecular sieves prior to use. Silicon wafers (111) were obtained from University Wafer, Inc. Silica-coated QCM-D sensor crystals (QSX-303) were purchased from Q-Sense. Medical-grade RTV silicone (MED-1137) was purchased from NuSil. Per manufacturer specifications, MED-1137 is comprised of α,ω-bis(Si–OH)PDMS, silica

(11–21%), methyltriacetoxysilane (<5%), ethyltriacetoxysilane (<5%), and trace amounts of acetic acid. The Alexa Fluor 546-dye conjugate of HF (AF-546 HF; M_w = 340 kDa; lyophilized) was obtained from Invitrogen.

C.7.2 Synthetic Approach

All reactions were run under a N2 atmosphere with a Teflon-covered stir bar to agitate the reaction mixture. Chemical structures were confirmed with nuclear magnetic resonance (NMR) spectroscopy using a Mercury 300 MHz spectrometer operating in the Fourier transform mode and with CDCl3 as the standard.

C.7.2.1 Synthesis of Allyl Methyl PEO_{16}

Allyl methyl PEO_{16} was prepared using a procedure adapted from literature.[77,78] PEO methyl ether (M_n = 736 g mol^{-1}, 13.98 g, 19 mmol) was dissolved in 90 mL tetrahydrofuran (THF) and added dropwise to a chilled (0 °C) NaH dispersion (6.24 g, 156 mmol) in 120 mL THF. The reaction was then warmed to room temperature (RT) and stirred for 6 h. Next, the PEO solution was chilled, allyl bromide (19.32 g, 160 mmol) in 120 mL THF was added dropwise, and the mixture was warmed to RT and stirred for 16 h. The reaction was then filtered to remove precipitates and volatiles removed under reduced pressure. The resulting orange oil was dissolved in 75 mL de-ionized (DI) water and washed three times with 75 mL toluene. The product was

extracted three times with 50 mL chloroform. The chloroform solution was then dried with anhydrous $MgSO_4$, filtered, and volatiles removed under reduced pressure to yield the final product (8.32 g, 56% yield) as a white, waxy solid. ^{1}H NMR (δ, ppm): 3.36 (s, 3H, OCH_3), 3.51–3.68 (m, 64H, OCH_2CH_2), 4.00 (dt, J = 5.7 and 1.5 Hz, 2H, CH_2═$CHCH_2O$), 5.14–5.28 (m, 2H, CH_2═$CHCH_2O$) and 5.83–5.96 (m, 1H, CH_2═$CHCH_2O$).

C.7.2.2 Synthesis of PEO–Silane Amphiphiles (n = 3, 8, and 16)

PEO–silane amphiphiles (Fig. C2) were prepared as previously reported for n = 8.44 Wilkinson's-catalyzed regioselective hydrosilylation of VTEOS and α,ω-bis-(SiH)oligodimethylsiloxane$_{13}$ produced "**1**" which was then subjected to Karstedt'scatalyzed hydrosilylation with the designated allyl methyl PEO_n. PEO–silane amphiphile (n = 3). **1** (22.11 g, 17.2 mmol), allyl methyl PEO3 (3.50 g, 17.2 mmol) and Karstedt's catalyst were reacted together. In this way, the product (25.76 g, 94% yield) was obtained. ^{1}H NMR (δ, ppm): 0.00–0.15 (m, 90H, $SiCH_3$), 0.48–0.55 (m, 2H, $SiCH_2CH_2CH_2$), 0.56 (s, 3H, $SiCH_2CH_2$), 1.09 (d, J = 7.8 Hz, 1H, $SiCH_2CH_2$), 1.22 (t, J =7.1 Hz, 9H, $SiOCH_2$-CH_3), 1.54–1.66 (m, 2H, $SiCH_2CH_2CH_2$), 3.38 (s, 3H, OCH_3), 3.41 (t, J =7.2 Hz, 2H, $SiCH_2CH_2CH_2$), 3.52–3.69 (m, 12H, CH_2CH_2O) and 3.82 (q, J = 7.0 Hz, 6H, $SiOCH_2CH_3$).

C.7.2.3 PEO–Silane Amphiphile (n = 8)

1 (20.02 g, 15.57 mmol), allyl methyl PEO8 (6.60 g, 15.57 mmol) and Karstedt's catalyst were reacted together.[44] In this way, the product (22.68 g, 85% yield) was obtained. ^{1}H NMR (δ, ppm): -0.02–0.14 (m, 90H, $SiCH_3$), 0.47–0.53 (m, 2H, $SiCH_2CH_2CH_2$), 0.55 (s, 3H, $SiCH_2CH_2$), 1.08 (d, J =7.5 Hz, 1H, $SiCH_2CH_2$), 1.22 (t, J = 7.1 Hz, 9H, $SiOCH_2$-CH_3), 1.52–1.66 (m, 2H, $SiCH_2CH_2CH_2$), 3.37 (s, 3H, OCH_3), 3.40 (t, J = 7.2 Hz, 2H, $SiCH_2CH_2CH_2$), 3.51–3.68 (m, 32H, CH_2CH_2O) and 3.81 (q, J = 7.0 Hz, 6H, $SiOCH_2CH_3$).

C.7.2.4 PEO–Silane Amphiphile (n = 16)

1 (17.98 g, 13.98 mmol), allyl methyl PEO_{16} (10.85 g, 13.98 mmol) and Karstedt's catalyst were reacted together.[44] In this way, the product (23.55 g, 82% yield) was obtained. ^{1}H NMR (δ, ppm): -0.01–0.15 (m, 90H, $SiCH_3$), 0.47–0.54 (m, 2H, $SiCH_2CH_2CH_2$), 0.55 (s, 3H, $SiCH_2CH_2$), 1.09 (d, J = 7.5 Hz, 1H, $SiCH_2CH_2$), 1.22 (t, J = 6.9 Hz, 9H, $SiOCH_2$-CH_3), 1.52–1.66 (m, 2H, $SiCH_2CH_2CH_2$), 3.37 (s, 3H, OCH_3), 3.41 (t, J ¼ 7.2 Hz, 2H, $SiCH_2CH_2CH_2$), 3.52–3.72 (m, 64H, CH_2CH_2O) and 3.82 (q, J = 6.9 Hz, 6H, $SiOCH_2CH_3$).

C.7.3 Synthesis of Siloxane- and PEO-Controls (n ¼ 3, 8, and 16)

PEO-controls (*i.e.* no siloxane tethers) (Fig. C2) were prepared as previously reported for $n = 8$ by the Karstedt's-catalyzed hydrosilylation of triethoxysilane and the designated allyl methyl PEO_n (1.1 : 1.0 molar ratio).[44]

C.7.3.1 PEO-Control ($n = 3$)

Triethoxysilane (5.43 g, 33.1 mmol), allyl methyl PEO_3 (6.14 g, 30.1 mmol) and Karstedt's catalyst were reacted together. In this way, the product (7.53 g, 65% yield) was obtained. ^{1}H NMR (δ, ppm): 0.57–0.65 (m, 2H, $SiCH_2CH_2CH_2$), 1.20 (t, $J = 6.9$ Hz, 9H, $SiOCH_2CH_3$), 1.62–1.74 (m, 2H, $SiCH_2$-CH_2CH_2), 3.36 (s, 3H, OCH_3), 3.41 (t, $J = 6.9$ Hz, 2H, $SiCH_2$-CH_2CH_2), 3.51–3.68 (m, 12H, CH_2CH_2O) and 3.80 (q, $J = 7.1$ Hz, 6H, $SiOCH_2CH_3$).

C.7.3.2 PEO-Control ($n = 8$)

Triethoxysilane (4.24 g, 25.8 mmol), allyl methyl PEO_8 (9.94 g, 23.4 mmol) and Karstedt's catalyst were reacted together.[44] In this way, the product (9.32 g, 68% yield) was obtained. ^{1}H NMR (δ, ppm): 0.57–0.64 (m, 2H, $SiCH_2CH_2$-CH_2), 1.20 (t, $J = 7.1$ Hz, 9H, $SiOCH_2CH_3$), 1.62–1.74 (m, 2H, $SiCH_2CH_2CH_2$), 3.36 (s, 3H, OCH_3), 3.41 (t, $J = 6.8$ Hz, 2H, $SiCH_2CH_2CH_2$), 3.50–3.66 (m, 32H, CH_2CH_2O) and 3.79 (q, $J = 7.0$ Hz,

6H, $SiOCH_2CH_3$). PEO-control (n = 16). Triethoxysilane (1.57 g, 9.57 mmol), allyl methyl PEO_{16} (6.74 g, 8.69 mmol) and Karstedt's catalyst were reacted together. In this way, the product (4.17 g, 50% yield) was obtained. ^{1}H NMR (δ, ppm): 0.57–0.65 (m, 2H, $SiCH_2CH_2CH_2$), 1.20 (t, J = 6.9 Hz, 9H, $SiOCH_2CH_3$), 1.62–1.74 (m, 2H, $SiCH_2$-CH_2CH_2), 3.36 (s, 3H, OCH_3), 3.41 (t, J = 6.9 Hz, 2H, $SiCH_2$-CH_2CH_2), 3.50–3.71 (m, 64H, CH_2CH_2O) and 3.80 (q, J = 7.0 Hz, 6H, $SiOCH_2CH_3$).

C.7.3.3 Siloxane-Control (1)

1 served as the siloxane-control and was prepared as noted above for the rst step of the synthesis of the PEO–silane amphiphiles. VTEOS (3.53 g, 18.6 mmol) and a,ubis-(SiH)oligodimethylsiloxane (20.37 g, 18.6 mmol) were reacted together.[44] In this way, the product (23.65 g, 99% yield) was obtained ^{1}H NMR (δ, ppm): 0.003–0.177 (m, 84H, $SiCH_3$), 0.19 (d, J = 2.7 Hz, 6H, $OSi[CH_3]_2H$), 0.56 (s, 3H, $SiCH_2CH_2$), 1.09 (d, J = 7.5 Hz, 1H, $SiCH_2CH_2$), 1.23 (t, J = 7.1 Hz, 9H, $SiOCH_2CH_3$), 3.83 (q, J = 7.0 Hz, 6H, $SiOCH_2CH_3$) and 4.67–4.73 (m, 1H, SiH).

C.7.4 Coating Preparation

C.7.4.1 Preparation of Surface-Grafted Coatings on Silicon Wafers

Silicon wafers (1" x 1") were cleaned by sequentially sonicating in (10 min) and rinsing with acetone, repeating with DI water and then drying in a 120 °C oven overnight. Next, the surfaces of the wafers were oxidized by submerging in a 7 x 3 v/v concentrated H_2SO_4/30% H_2O_2 (Piranha) solution for 30 min (warning: Piranha solution must be handled with extreme caution), removed, rinsed thoroughly with DI water and dried under a stream of air. In a typical procedure, grafting solutions comprised of each of the PEO–silane amphiphiles, PEOcontrols and the siloxane-control were prepared at a concentration of 0.012 M in isopropanol (IPA) (30 mL). Following the addition of 1 drop of DI water, the grafting solutions were mixed in sealed jars for 1 h on a shaker table. Next, an oxidized wafer was placed into a jar and remained on a shaker table for 12 h. Afterwards, the wafers were removed, air dried, and cured under vacuum (36 mm Hg) at 150 °C for 12 h. To remove unbound chains, the wafers were sequentially soaked (1 h), sonicated (3 min) and rinsed with ethanol, the sequence repeated with DI water and then lastly dried under a stream of air.

C.7.4.2 Preparation of Modified Silicone Coatings

Glass microscope slides were sequentially rinsed with dichloromethane (DCM) and acetone followed by drying in a 120 °C oven overnight. Casting solutions were prepared by combining 2.0 g MED-1137 silicone in 6 g (9 mL) hexane and mixing with a vortexer until a homogenous solution was obtained. The PEO–silane amphiphiles, PEO-controls and siloxane-control were each added to individual casting solutions at 50 mmol of silane per 1.0 g silicone and mixed thoroughly. Solutions were solvent-cast onto leveled glass microscope slides (1.5 mL per slide) and a polystyrene Petri dish cover placed on top of each so as to slow solvent evaporation and prevent bubble formation. The films were allowed to cure for one week at RT and immediately used for designated analyses.

C.7.5 Surface Characterization

C.7.5.1 XPS

Surface composition analysis of surface-grafted coatings on silicon wafers was performed with a KRATO AXIS Ultra Imaging X-ray Photoelectron Spectrometer with a monochromatized Mg K_α source and operating at a base pressure of ~2% x 10^{-9} mbar. The area of analysis was 7 x 3 mm. Elemental atomic percent compositions were determined from three survey spectra sweeps performed from 0 to 1100 eV. High

resolution (HR) analyses with a pass energy of 40 eV were performed with a take-off angle of 90°. HR scans (180 s sweeps) were performed at 526 to 536 eV for O 1s, 280 to 295 eV for C 1s, and 96 to 106 eV for Si 2p. Raw data was quantified and analyzed using XPS Peak Processing software.

C.7.5.2 Ellipsometry

The thickness of surface-grafted coatings on silicon wafers was measured *via* ellipsometry (Alpha-SE, J.A. Woollam) with an incident angle of 70° in the spectral range of 380–900 nm and in the high-precision mode (30 s data acquisition time). The average thickness of the oxide layer of an oxidized silicon wafer was determined at three regions of a wafer specimen (taken from a wafer designated for grafting with a particular composition) using a standard two-layer (silica–silicon) optical model included in the manufacturer's software. To measure the thickness of the grafted chains, the previously determined oxide layer thickness was utilized in a second optical model that included the third "Cauchy layer" (polymer–silica–silicon). The index of refraction (n) was set to 1.450 which is that of crystalline PEO.[47,53] The average thickness (h) of the grafted layers was based on four individual wafers, each measured at three different regions.

C.7.5.3 Water Contact Angle Analysis

Static contact angles (θ_{static}) of DI water droplets were measured at RT using a CAM-200 goniometer (KSV Instruments) equipped with an autodispenser, video camera, and drop-shape analysis software (Attension Theta). Following deposition, a 5 mL sessile drop of water was iteratively measured over a 2 min (surface-grafted wafers) and 3 min (silicone-based coatings) period. The reported qstatic values of the surface-grafted wafers were based on four individual wafers, each measured at three different areas (12 measurements total). The θ_{static} for the silicone-based coatings was an average of three measurements from different areas of the same film surface.

C.7.5.4 Protein Adsorption

Protein adsorption onto surface-grafted coatings was measured by QCM-D (Q-Sense E4). Silicon dioxide coated sensors (50 nm thickness; Q-Sense) were ultrasonically cleaned with acetone and DI water as described above for silicon wafers. Following exposure to oxygen plasma for 2 min (Harrick Plasma, PDC-001), the sensors were surface-grafted with the designated PEO–silane amphiphile, PEO-control or siloxane-control as described above for silicon wafers. Contact angle analysis was used to verify grafting. Grafted sensors were subjected to the following sequence: (1) 150 μL min^{-1} flow of PBS until the frequency and dissipation values remained constant for >5 min, (2) 150 μL min^{-1} flow of 100 μg mL^{-1} HF in PBS for 20 min and (3) 150 μL min^{-1}

flow of PBS for 5 min to remove loosely bound protein. The manufacturer's software was used to process the raw data and determine the mass of HF adsorbed to each sensor.

The adsorption of AF-546 HF onto silicone coatings was measured via fluorescence microscopy. A silicone isolator well (20 mm well diameter, 2 mm depth; McMaster-Carr) was pressed against silicone films thereby creating a seal which prevented leakage of solution from the well. Fibrinogen solution (100 μg mL^{-1} in PBS, 0.7 mL) was added to each well. (Note: per manufacturer specifications, the AF-546 was first dissolved in 0.1 M NaHCO3 to obtain a 1.5 μg mL^{-1}solution and was further diluted in PBS to obtain a final concentration of 0.1 mg mL^{-1}.) After 3 h at RT (protected from light), the solution was removed and 0.7 mL of fresh PBS was then added to each well and removed after 5 min. This process was repeated five times with fresh PBS and lastly one time with DI water. The samples were dried under a stream of air and protected from light until imaged. For each coating, an additional specimen was prepared and likewise rinsed with PBS and DI water, but without exposure to AF-546 (*i.e.* soaked 3 h in PBS) in order to correct for the background intensity.

A FV1000 (Olympus) laser scanning confocal microscope was used for quantification of protein adsorption onto all films. Imaging conditions, both in excitation and collection, were identical for all samples: objective (SPLSAPO 10x objective, NA 0.40), laser excitation type and intensity (HeNe 543 nm source), field of view and resolution (256 x 256 pixels, 317 x 317 micron field of view), depth (40 slices at 1 mm per slice), slice averaging, and collection (150 mm pinhole, 560 nm long-pass filter followed by a 560–660 nm band-pass filter, identical photomultiplier

voltages/sensitivities). Data analysis was performed on the FV10-ASW v3.1 software suite (Olympus). Each surface was imaged in three locations and aggregate intensities computed. These were compared to three images obtained from the analogous surface that had similar treatment without protein exposure. Changes in intensity from exposure to protein were then obtained and compared, with errors reported as the standard deviation of three measurements.

C.8 Conclusions

While the exceptional protein resistance of PEO (e.g. conventional PEO–silanes) is well described, these observations have largely been made when PEO is grafted to a physically stable substrate (e.g. silicon wafer). In this way, migration of the PEO to the surface–water interface (where protein and other biological adhesion occurs) is not required. However, when PEO is used to bulk-modify a silicone elastomer, rapid water-driven restructuring is essential in order to affect protein resistance. In this work, both surface-grafted silicon and bulk-modified silicones were prepared with PEO–silane amphiphiles comprised of a siloxane tether (m = 13) and a PEO segment of variable lengths (n = 3, 8, and 16) as well as the corresponding PEO controls (*i.e.* no siloxane tether). Surface-grafted PEO-controls, due to their greater hydrophilicity, demonstrated superior resistance to fibrinogen versus the PEO–silane amphiphiles. However, when used to bulk-modify a silicone, PEO-controls produced surfaces that remained hydrophobic after 3 min of exposure to water. As a result, these surfaces exhibited poor

resistance to protein adsorption. In contrast, PEO–silane amphiphiles (n = 8 and 16) demonstrated dramatic and rapid water-driven surface restructuring, becoming extremely hydrophilic after exposure to water for only 3 min. As a result, these surfaces displayed exceptionally high resistance to fibrinogen. While the PEO–silane amphiphile (n = 3) also exhibited water driven restructuring, the achieved hydrophilicity and resistance to protein was diminished by its low PEO content. The enhanced potential of PEO–silane amphiphiles to migrate to the surface–water interface and reduce protein adsorption may be attributed to the hydrophobic nature as well as flexibility of the siloxane tether which allows movement of the tether and attached PEO segment through the silicone network. Furthermore, these results point to the limitations of predicting PEO's protein resistance using model substrates.

C.9 Acknowledgements

The authors thank the Texas Engineering and Experiment Station (TEES) for financial support of this research. M. A. Rufin gratefully acknowledges support from the NIH (3R01DK95101-02S1). J. A. Gruetzner thanks the Texas A&M University Research Opportunities Experience Fellowship. J. E. Raymond acknowledges support from the Welch Foundation (#A-0001) and the Office of Naval Research (N00014-14-1-0082). We also thank Professor Karen L. Wooley (Texas A&M University, Department of Chemistry) and the Laboratory for Synthetic–Biologic Interactions for use of the QCM-D.

C.10 Notes and References

1. J. Curtis and A. Colas, in Biomaterials Science: An Introduction to Materials in Medicine, ed. B. D. Ratner, A. S. Hoffman, F. J. Schoen and J. E. Lemons, Academic Press, New York, 2nd edn, 2004, ch. 7.19, p. 697.
2. M. E. Van Dyke, S. J. Clarson and R. Arshady, in An Introduction to Polymeric Biomaterials, ed. R. Arshady, Citrus Books, London, 2003, p. 109.
3. H. S. El-Zaim and J. P. Heggers, in Polymeric Biomaterials, ed. S. Dumitriu, Marcel Dekker, New York, 2nd edn, 2001, ch. 3, p. 79.
4. M. Lejars, A. Margaillan and C. Bressy, Chem. Rev., 2012, 112, 4347.
5. J. L. Brash, Ann. N. Y. Acad. Sci., 1977, 283, 356.
6. S. Krishnan, C. J. Weinman and C. K. Ober, J. Mater. Chem., 2008, 18, 3405.
7. S. R. Hanson, in Biomaterials Science: An Introduction to Materials in Medicine, ed. B. D. Ratner, A. S. Hoffman, F. J. Schoen and J. E. Lemons, Academic Press, New York, 2nd edn, 2004, ch. 4.6, p. 332.
8. I. I. Raad, M. Luna, S.-A. M. Khalil, J. W. Costerton, C. Lam and G. P. Bodey, JAMA, J. Am. Med. Assoc., 1994, 271, 1014.
9. D. A. Lloyd, L. K. R. Shanbhogue, P. J. Doherty, D. Sunderland, C. A. Hart and D. F. Williams, J. Pediatr. Surg., 1993, 28, 345.
10. P. Hron, Polym. Int., 2003, 52, 1531.
11. F. Abbasi, H. Mirzadeh and A.-A. Katbab, Polym. Int., 2001, 50, 1279.
12. D. Bodas and C. Khan-Malek, Microelectron. Eng., 2006, 83, 1277.

13. K. Yao, X.-D. Huang, X.-J. Huang and Z.-K. Xu, J. Biomed. Mater. Res., Part A, 2006, 78, 684.

14. H. Zhang, G. M. Annich, J. Miskulin, K. Osterholzer, S. I. Merz, R. H. Bartlett and M. E. Meyerhoff, Biomaterials, 2002, 23, 1485.

15. M. Morra, E. Occhiello and F. Garbassi, Clin. Mater., 1993, 14, 255.

16. J. H. Lee, Y. M. Ju and D. M. Kim, Biomaterials, 2000, 21, 683.

17. J. G. Archambault and J. L. Brash, Colloids Surf., B, 2004, 39, 9.

18. B. Balakrishnan, D. S. Kumar, Y. Yoshida and A. Jayakrishnan, Biomaterials, 2005, 26, 3495.

19. I. Banerjee, R. C. Pangule and R. S. Kane, Adv. Mater., 2011, 23, 690.

20. J. H. Lee, H. B. Lee and J. D. Andrade, Prog. Polym. Sci., 1995, 20, 1043.

21. S. I. Jeon, J. H. Lee, J. D. Andrade and P. G. De Gennes, J. Colloid Interface Sci., 1991, 142, 149.

22. S. I. Jeon and J. D. Andrade, J. Colloid Interface Sci., 1991, 142, 159.

23. D. Knoll and J. Hermans, J. Biol. Chem., 1983, 258, 5710.

24. Poly(Ethylene Glycol) Chemistry: Biotechnical and Biomedical Applications, ed. J. M. Harris, Plenum Press, New York, 1992.

25. M. B. Browning, S. N. Cereceres, P. T. Luong and E. M. Cosgriff-Hernandez, J. Biomed. Mater. Res., Part A, 2014, 102, 4244.

26. K. L. Prime and G. M. Whitesides, J. Am. Chem. Soc., 1993, 115, 10714.

27. K. Feldman, G. H¨ahner, N. D. Spencer, P. Harder and M. Grunze, J. Am. Chem. Soc., 1999, 121, 10134.

28. C. Pale-Grosdemange, E. S. Simon, K. L. Prime and G. M. Whitesides, J. Am. Chem. Soc., 1991, 113, 12.

29. M. Zhang, T. Desai and M. Ferrari, Biomaterials, 1998, 19, 953.

30. M. Zhang and M. Ferrari, Biomed. Microdevices, 1998, 1, 81.

31. A. Papra, N. Gadegaard and N. B. Larsen, Langmuir, 2001, 17, 1457.

32. S.-W. Lee and P. E. Laibinis, Biomaterials, 1998, 19, 1669.

33. S. Jo and K. Park, Biomaterials, 2000, 21, 605.

34. H. Yasuda, A. K. Sharma and T. Yasuda, J. Polym. Sci., Polym. Phys. Ed., 1981, 19, 1285.

35. M. J. Owen and P. J. Smith, J. Adhes. Sci. Technol., 1994, 8, 1063.

36. M. J. Owen, in Silicon-based Polymer Science: A Comprehensive Resource, ed. J. M. Zeigler and F. W. G. Fearon, American Chemical Society, Washington, D.C., 1990, ch. 40, p. 705.

37. M. J. Owen, in Siloxane Polymers, ed. S. J. Clarson and J. A. Semlyen, Prentice Hall, Englewood Cliffs, 1993, ch. 7, p. 309.

38. J. E. Mark, in Silicon-Based Polymer Science: A Comprehensive Review, ed. J. M. Zeigler and F. W. G. Fearon, American Chemical Society, Washington, D.C., 1990, vol. 224, ch. 2, p. 47.

39. T. H. Lane and S. A. Burns, in Immunology of Silicones, ed. M. Potter and N. R. Rose, Springer, Berlin, 1996, p. 3.

40. H. Chen, M. A. Brook and H. Sheardown, Biomaterials, 2004, 25, 2273.

41. H. Chen, M. A. Brook, Y. Chen and H. Sheardown, J. Biomater. Sci., Polym. Ed., 2005, 16, 531.

42. D. B. Thompson, A. S. Fawcett and M. A. Brook, in Silicon Based Polymers, ed. F. Ganachaud, S. Boileau and B. Boury, Springer, 2008, ch. 3, p. 29, DOI: 10.1007/978-1-4020-8528-4_3.

43. H. Chen, Z. Zhang, Y. Chen, M. A. Brook and H. Sheardown, Biomaterials, 2005, 26, 2391.

44. R. Murthy, C. D. Cox, M. S. Hahn and M. A. Grunlan, Biomacromolecules, 2007, 8, 3244.

45. M. L. Hawkins, F. Fa¨y, K. R´ehel, I. Linossier and M. A. Grunlan, Biofouling, 2014, 30, 247.

46. M. L. Hawkins, M. A. Rufin, J. E. Raymond and M. A. Grunlan, J. Mater. Chem. B, 2014, 2, 5689.

47. R. Murthy, C. E. Shell and M. A. Grunlan, Biomaterials, 2009, 30, 2433.

48. R. Murthy, B. M. Bailey, C. Valentin-Rodriguez, A. Ivanisevic and M. A. Grunlan, J. Polym. Sci., Part A: Polym. Chem., 2010, 48, 4108.

49. M. L. Hawkins and M. A. Grunlan, J. Mater. Chem., 2012, 22, 19540.

50. O. Moreau, C. Portella, F. Massicot, J. M. Herry and A. M. Riquest, Surf. Coat. Technol., 2007, 201, 5994.

51. M. A. Cole, H. Thissen, D. Losie and N. H. Voelcker, Surf. Sci., 2007, 601, 1716.

52. S. J. Sofia, V. Premnath and E. W. Merrill, Macromolecules, 1998, 31, 5059.

53. L. D. Unsworth, Z. Tun, H. Sheardown and J. L. Brash, J. Colloid Interface Sci., 2005, 281, 112.

54. W. Feng, J. L. Brash and S. Zhu, Biomaterials, 2006, 27, 847.

55. S. Sharma, R. W. Johnson and T. A. Desai, Appl. Surf. Sci., 2003, 206, 218.

56. B. Zdyrko, V. Klep and I. Luzinov, Langmuir, 2003, 19, 10179.

57. P. Harder, M. Grunze, R. Dahint, G. M. Whitesides and P. E. Laibinis, J. Phys. Chem. B, 1998, 102, 426.

58. R. Soong and P. M. Macdonald, Biochim. Biophys. Acta, Biomembr., 2007, 1768, 1805.

59. C. Allen, N. Dos Santos, R. Gallagher, G. N. C. Chiu, Y. Shu, W. M. Li, S. A. Johnstone, A. S. Janoff, L. D. Mayer, M. S. Webb and M. B. Bally, Biosci. Rep., 2002, 22, 225.

60. M. Sangermano, R. Bongiovanni, G. Malucelli, A. Priola, A. Pollicino and A. Recca, J. Appl. Polym. Sci., 2003, 89, 1524.

61. W. G. Pitt, K. Park and S. L. Cooper, J. Colloid Interface Sci., 1986, 111, 343.

62. L. Tang and J. W. Eaton, J. Exp. Med., 1993, 178, 2147.

63. W.-B. Tsai, J. M. Grunkemeier and T. A. Horbett, J. Biomed. Mater. Res., 1999, 44, 130.

64. Y. Wu, F. I. Simonovsky, B. D. Ratner and T. A. Horbett, J. Biomed. Mater. Res., Part A, 2005, 74, 722.

65. W.-J. Hu, J. W. Eaton, T. P. Ugarova and L. Tang, Blood, 2001, 98, 1231.

66. Q. Wei, T. Becherer, S. Angioletti-Uberti, J. Dzubiella, C. Wischke, A. T. Neffe, A. Lendlein, M. Ballauff and R. Haag, Angew. Chem., Int. Ed., 2014, 53, 8004.

67. C. J. Nonckreman, S. Fleith, P. G. Rouxhet and C. C. Dupont-Gillain, Colloids Surf., B, 2010, 77, 139.

68. A. G. Hemmersam, M. Foss, J. Chevallier and F. Besenbacher, Colloids Surf., B, 2005, 43, 208.

69. K. Park, S. Shim Hong, K. Dewanjee Mrinal and L. Eigler Neal, J. Biomater. Sci., Polym. Ed., 2000, 11, 1121.

70. Y. Luan, D. Li, Y. Wang, X. Liu, J. L. Brash and H. Chen, Langmuir, 2014, 30, 1029.

71. M. Tanaka, T. Sawaguchi, Y. Sato, K. Yoshioka and O. Niwa, Tetrahedron Lett., 2009, 50, 4092.

72. M. S. Lord, M. H. Stenzel, A. Simmons and B. K. Milthorpe, Biomaterials, 2006, 27, 1341.

73. M. Tanaka, A. Mochizuki, T. Motomura, K. Shimura, M. Onishi and Y. Okahata, Colloids Surf., A, 2001, 193, 145.

74. M. A. Cooper and V. T. Singleton, J. Mol. Recognit., 2007, 20, 154.

75. D. R. Lu and K. Park, J. Colloid Interface Sci., 1991, 144, 271.

76. S. J. Geelhood, T. A. Horbett, W. K. Ward, M. D. Wood and M. J. Quinn, J. Biomed. Mater. Res., Part B, 2007, 81, 251.

77. R. Hooper, L. J. Lyons, M. K. Mapes, D. Schumacher, D. A. Moline and R. West, Macromolecules, 2001, 34, 931.

78. Y. Chang, Y. C. Kwon, S. C. Lee and C. Kim, Macromolecules, 2000, 33, 4496.

C.11 Supplementary Material

		θ_{static} @ 15 sec	θ_{static} @ 2 min
Siloxane-control		91.6 ± 3.7	89.7 ± 4.6
n = 3	Control	59.0 ± 2.3	56.5 ± 1.7
	Amphiphile	95.2 ± 0.7	93.7 ± 0.7
n = 8	Control	44.3 ± 1.1	42.3 ± 1.2
	Amphiphile	89.7 ± 2.1	87.9 ± 2.2
n = 16	Control	39.8 ± 2.9	37.1 ± 3.0
	Amphiphile	79.5 ± 7.5	76.8 ± 8.4

Table C9. Static water contact angles (°) measured on surface-grafted silicon wafers. Each value reported is the average and standard deviation of measurements performed in triplicate on four identically prepared samples (12 measurements total)

	Unmodified silicone	Siloxane-control	n = 3		n = 8		n = 16	
			Control	Amphiphile	Control	Amphiphile	Control	Amphiphile
Initial	114.8±1.1	115.9 ± 0.6	111.6±1.6	117.1±0.7	112.6 ± 0.4	117.2±0.6	115.3±1.0	115.2±3.3
15 sec	114.6±1.1	111.6 ± 0.2	108.0±1.2	94.9±0.8	104.9 ± 0.6	63.6±0.4	114.4±0.8	110.0±1.1
30 sec	114.4±1.1	109.3 ± 0.3	104.3±1.0	90.9±0.6	102.6 ± 0.7	46.9±0.6	111.3±1.1	104.2±0.4
1 min	114.2±1.0	107.2 ± 0.3	101.8±1.0	88.3±0.4	100.7 ± 0.9	38.5±0.7	107.4±0.7	90.7±1.4
2 min	113.2±1.2	105.0 ± 0.2	99.3±0.9	85.9±0.3	99.1 ± 1.1	32.0±0.5	105.2±0.6	66.4±0.9
3 min	111.1±1.7	103.5 ± 0.3	97.7±0.9	84.3±0.4	97.8 ± 1.3	29.0±0.5	103.6±0.5	56.6±0.8

Table C10. Static water contact angles (°) measured on bulk-modified silicone films. Each value reported is the average and standard deviation of three water droplets measured on the same film

		Absolute	Normalized
Unmodified		2280.56 ± 41.03	100.00 ± 1.80
Siloxane-control		2162.79 ± 28.75	94.84 ± 1.26
n = 3	Control	2314.98 ± 41.91	101.51 ± 1.84
	Amphiphile	3013.66 ± 30.90	132.15 ± 1.36
n = 8	Control	3303.40 ± 146.60	144.85 ± 6.43
	Amphiphile	1.98 ± 1.18	0.09 ± 0.05
n = 16	Control	1438.91 ± 976.56	63.09 ± 42.82
	Amphiphile	4.21 ± 1.27	0.18 ± 0.06

Table C11. Fluorescence intensity measured on bulk-modified silicone films before (absolute) and after normalizing all values to the signal measured on unmodified silicone